AD-A132 843 THE RESPONSE OF A LAMINAR BOUNDARY LAYER TO SOUND AND WALL VIBRATION(U) MASSACHUSETTS INST OF TECH CAMBRIDGE ACOUSTICS AND VIBRATION L.. C J GEDNEY MAY 83 1/2

UNCLASSIFIED A/V-83560-3 N00014-76-C-0396 F/G 20/4 NL

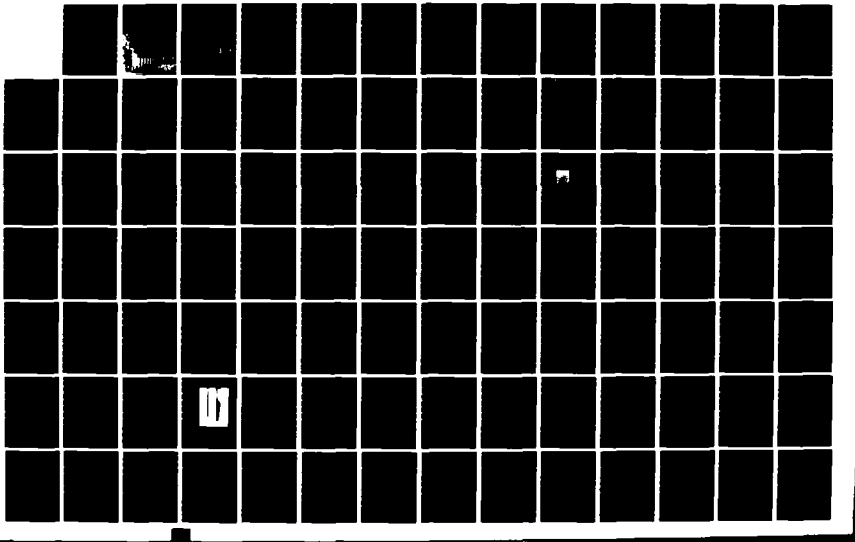

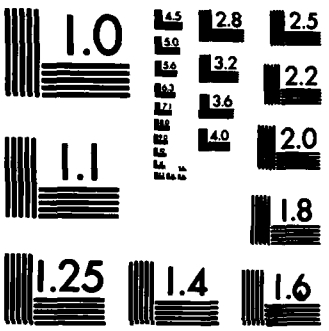

THE RESPONSE OF A LAMINAR BOUNDARY LAYER TO SOUND AND WALL VIBRATION

by

CHARLES J. GEDNEY

Report No. 83560-3
May 1983

This research was carried out under the
Mechanics Division of the Office of Naval Research
under Contract N00014-76-C-0396

Acoustics and Vibration Laboratory
Massachusetts Institute of Technology
Cambridge, Massachusetts 02139

Massachusetts Institute of Technology
Cambridge, Massachusetts 02139

Unclassified

SECURITY CLASSIFICATION OF THIS PAGE (When Data Entered)

REPORT DOCUMENTATION PAGE		READ INSTRUCTIONS BEFORE COMPLETING FORM
1. REPORT NUMBER 83560-3	2. GOVT ACCESSION NO. AD-A132843	3. RECIPIENT'S CATALOG NUMBER
4. TITLE (and Subtitle) The Response of a Laminar Boundary Layer to Sound and Wall Vibration		5. TYPE OF REPORT & PERIOD COVERED 6. PERFORMING ORG. REPORT NUMBER
7. AUTHOR(s) Charles J. Gedney		8. CONTRACT OR GRANT NUMBER(s) N00014-76-C-0396
9. PERFORMING ORGANIZATION NAME AND ADDRESS Massachusetts Institute of Technology Cambridge, Massachusetts 02139		10. PROGRAM ELEMENT, PROJECT, TASK AREA & WORK UNIT NUMBERS
11. CONTROLLING OFFICE NAME AND ADDRESS Mechanics Division, Office of Naval Research 800 N. Quincy Street Arlington, VA 22217		12. REPORT DATE May 1983 13. NUMBER OF PAGES 172
14. MONITORING AGENCY NAME & ADDRESS(if different from Controlling Office) Mechanics Division, Office of Naval Research 800 N. Quincy Street Arlington, VA 22217		15. SECURITY CLASS. (of this report) Unclassified 15a. DECLASSIFICATION/DOWNGRADING SCHEDULE

16. DISTRIBUTION STATEMENT (of this Report)

Approved for public release; distribution unlimited

17. DISTRIBUTION STATEMENT (of the abstract entered in Block 20, if different from Report)

18. SUPPLEMENTARY NOTES

19. KEY WORDS (Continue on reverse side if necessary and identify by block number)

20. ABSTRACT (Continue on reverse side if necessary and identify by block number)

An experimental analysis of the interaction of sound and plate vibration with a laminar boundary layer is presented. The two excitations generate disturbances at the leading edge of the plate which develop into Tollmien-Schlichting (TS) waves in the quasi-parallel region of the boundary layer. It is demonstrated that the TS wave and the sound wave coexist independently in this region, as predicted by the linear theory. A TS wave generated by a vibrating ribbon is shown to superimpose linearly

DD FORM 1 JAN 73 1473 EDITION OF 1 NOV 65 IS OBSOLETE
S/N 0102-014-6601

SECURITY CLASSIFICATION OF THIS PAGE (When Data Entered)

with the sound-generated TS wave. Plate vibration is used to successfully cancel a sound-excited TS wave. With sound excitation, transition occurs at a streamwise Reynolds number (R_x) of 1.2×10^6. The addition of plate vibration delays transition to $R_x = 1.8 \times 10^6$. In the laminar region of the boundary layer (at $R_x = 0.97 \times 10^6$) the plate vibration reduces the level of streamwise velocity fluctuations from more than one hundred to only two times the particle velocity of the sound excitation.

THE RESPONSE OF A LAMINAR BOUNDARY LAYER TO SOUND AND WALL VIBRATION

by

CHARLES J. GEDNEY

May 1983

This research was carried out under the
Mechanics Division of the Office of Naval Research
under Contract N00014-76-C-0396

Approved for public release; distribution unlimited

Department of Mechanical Engineering
Massachusetts Institute of Technology
Cambridge, Massachusetts 02139

ABSTRACT

An experimental analysis of the interaction of sound and plate vibration with a laminar boundary layer is presented. The two excitations generate disturbances at the leading edge of the plate which develop into Tollmien-Schlichting (TS) waves in the quasi-parallel region of the boundary layer. It is demonstrated that the TS wave and the sound wave coexist independently in this region, as predicted by the linear theory. A TS wave generated by a vibrating ribbon is shown to superimpose linearly with the sound-generated TS wave. Plate vibration is used to successfully cancel a sound-exicted TS wave. With sound excitation, transition occurs at a streamwise Reynolds number (R_x) of 1.2×10^6. The addition of plate vibration delays transition to $R_x = 1.8 \times 10^6$. In the laminar region of the boundary layer (at $R_x = 0.97 \times 10^6$) the plate vibration reduces the level of streamwise velocity fluctuations from more than one hundred to only two times the particle velocity of the sound excitation.

ACKNOWLEDGEMENTS

The author would like to thank Professor Patrick Leehey for his help and guidance during the course of this research. The assistance and advice of Professors Erik L. Mollo-Christensen and C. Forbes Dewey is greatfully acknowledged. Discussions with Dr. Dietrich Bechert proved to be very helpful and are also appreciated.

Fellow students of the Acoustics and Vibration Laboratory also provided invaluable assistance and many enlightening discussions during the completion of this work. In particular, Shawn Burke, Charles Thompson, George Pariseanu and Mark Moeller extended their expert help. The work of Seung-Hee Lee, who supervised all of the numerical calculations which appear in this report, is also appreciated.

Special thanks go to my parents, Rex and Fraynie Gedney, for their support and to Patricia LeBlanc for her help and friendship. Finally, the companionship of Jedediah von Izenberg is greatly appreciated.

This research was supported by the Fluid Dynamics Program of the Office of Naval Research under contract number N00014-76-C-0396.

TABLE OF CONTENTS

Page

Abstract..... 2

Acknowledgements..... 3

List of Figures..... 5

Nomenclature..... 11

Chapter I. INTRODUCTION..... 15

Chapter II. BACKGROUND..... 20

Chapter III. THEORETICAL CONSIDERATIONS..... 32

Chapter IV. EXPERIMENTAL APPARATUS..... 53
- 4.1 Wind Tunnel..... 53
- 4.2 Test Section..... 59
- 4.3 Test Plate..... 65
- 4.4 Hot Wire Probe..... 67
- 4.5 Instrumentation..... 74
- 4.6 Experimental Conditions..... 88

Chapter V. EXPERIMENTAL RESULTS..... 99
- 5.1 Comparisons at $\beta=112\times10^{-6}$..... 99
- 5.2 Natural Excitation of the Boundary Layer..... 101
- 5.3 Sound Excitation of the Boundary Layer..... 106
- 5.4 Excitation of the Boundary Layer by Plate Vibration..... 118
- 5.5 Excitation of the Boundary Layer with a Vibrating Ribbon..... 125
- 5.6 Disturbance Growth Comparison..... 135
- 5.7 Cancellation of a Sound-Excited TS Wave with Plate Vibration..... 139
- 5.8 Characteristics of the Boundary Layer Excitations..... 145

Chapter VI. CONCLUSIONS..... 151

References..... 156

Appendix..... 166

LIST OF FIGURES

Figure	Title	Page
1.1	Transition Reynolds number (R_{xtr}) as a function of u'/U_∞ for several investigators (from Leehey [3])	17
3.1	Transition to turbulence on a flat plate (from White [51])	33
3.2	Sketch of the x, y, z coordinate system inside the wind tunnel test section	36
3.3	Disturbance stability (α_i/R) for the spatial, flat plate Orr-Sommerfeld problem as a function of Reynolds number and frequency (from Obremski et. al. [59])	44
3.4	Magnitude and phase of the eigenfunction $\bar{\varphi}(y)$ for the spatial, flat plate Orr-Sommerfeld problem	45
4.1	Wind tunnel facility	54
4.2	Spectral densities of the velocity fluctuations (u') in the free stream for three mean velocities at x = 0 and y = 3.0 cm (d = 1.1 mm, the mesh length of the turbulence reduction screens)	56
4.3	Free stream turbulence level. Measured at test section duct centerline	58
4.4	Background sound pressure spectral densities for three mean velocities, measured just outside of the open jet (d = 38 cm, the test section width)	60
4.5	Test section fairing	62
4.6	Sound particle velocity in the free stream at the excitation frequency (200 Hz) as a function of x. (Measured during the sound excitation tests. The phase is with respect to the speaker excitation signal)	63
4.7	Test plate cross section	66

Figure	Title	Page
4.8	Traverse with hot wire probe installed (from Shapiro [7])	69
4.9	Spectrum of the hot wire signal in the boundary layer at x = 21 cm, y = 0.4 mm, and U_∞ = 41 m/s (from Shapiro [7])	70
4.10	Set-up for hot wire vibration sensitivity test	71
4.11	Hot wire probe vibration transfer function without damping treatment. (Velocity at the sensor divided by the velocity at the probe base as a function of frequency.)	72
4.12	Phase of the hot wire probe vibration transfer function shown in Figure 4.11 (undamped)	73
4.13	Hot wire probe vibration transfer function with damping treatment. (Velocity at the sensor divided by the velocity at the probe base as a function of frequency.)	75
4.14	Phase of the hot wire probe vibration transfer function shown in Figure 4.13 (damped)	76
4.15	Schematic of the instrumentation used in the sound excitation tests	77
4.16	Linearizer output voltage as a function of the mean velocity at the hot wire	79
4.17	Mean velocity profile of the boundary layer at x = 15.2 cm, U_∞ = 18.5 m/s	80
4.18	Schematic of the instrumentation used in the plate vibration tests	83
4.19	Static pressure variations along the test plate at three free stream velocities	90
4.20	Top view of test plate showing side wall contamination and location of the vibrating ribbon	91

Figure	Title	Page
4.21	Sound pressure spectrum level during the sound excitation tests at x = 0 and y = 3.7 cm with U_∞ = 0	93
4.22	Plate acceleration spectrum level at x = 5.1 cm with U_∞ = 18.5 m/s during the plate vibration tests	94
4.23	Plate vibration level at the excitation frequency (200 Hz) as a function of x during the plate vibration tests	95
4.24	Plate vibration level at the excitation frequency (200 Hz) as a function of x during the sound excitation tests	96
4.25	Free stream velocity fluctuations at the excitation frequency (200 Hz) as a function of x during the plate vibration tests (y = 1.27 cm, U_∞ = 18.5 m/s)	98
5.1	Boundary layer disturbance amplitudes (at $\beta = 112\times10^{-6}$) as functions of the Reynolds number (U_∞ = 29.0 m/s and f = 1000 Hz)	100
5.2	Velocity signal at x = 66.5 cm, y = 0.5 mm and U_∞ = 18.5 m/s	103
5.3	Boundary layer disturbance amplitudes (at $\beta = 56\times10^{-6}$) as functions of the Reynolds number with natural excitation	105
5.4	Velocity fluctuations (at 200 Hz) as functions of y for sound excitation (x = 16.0 cm, U_∞ = 18.5 m/s)	107
5.5	Velocity fluctuations (at 200 Hz) as functions of y for sound excitation (x = 20.3 cm, U_∞ = 18.5 m/s)	108
5.6	Velocity fluctuations (at 200 Hz) as functions of y for sound excitation (x = 27.9 cm, U_∞ = 18.5 m/s)	109
5.7	Velocity fluctuations (at 200 Hz) as functions of y for sound excitation (x = 39.4 cm, U_∞ = 18.5 m/s)	110

Figure	Title	Page
5.8	Velocity fluctuations (at 200 Hz) as functions of y for sound excitation (x = 63.5 cm, U_∞ = 18.5 m/s).....	111
5.9	Velocity fluctuations (at 200 Hz) as functions of y for sound excitation. The sound excited results do not include the Stokes shear-wave (x = 16.0 cm, U_∞ = 18.5 m/s).....	113
5.10	Velocity fluctuations (at 200 Hz) as functions of y for sound excitation. The sound excited results do not include the Stokes shear-wave (x = 20.3 cm, U_∞ = 18.5 m/s).....	114
5.11	Velocity fluctuations (at 200 Hz) as functions of y for sound excitation. The sound excited results do not include the Stokes shear-wave (x = 27.9 cm, U_∞ = 18.5 m/s).....	115
5.12	Velocity fluctuations (at 200 Hz) as functions of y for sound excitation. The sound excited results do not include the Stokes shear-wave (x = 39.4 cm, U_∞ = 18.5 m/s).....	116
5.13	Velocity fluctuations (at 200 Hz) as functions of y for sound excitation. The sound excited results do not include the Stokes shear-wave (x = 63.5 cm, U_∞ = 18.5 m/s).....	117
5.14	Velocity fluctuations (at 200 Hz) as functions of y for plate vibration (x = 20.3 cm, U_∞ = 18.5 m/s).....	119
5.15	Velocity fluctuations (at 200 Hz) as functions of y for plate vibration (x = 27.9 cm, U_∞ = 18.5 m/s).....	120
5.16	Velocity fluctuations (at 200 Hz) as functions of y for plate vibration (x = 39.4 cm, U_∞ = 18.5 m/s).....	121

Figure	Title	Page
5.17	Velocity fluctuations (at 200 Hz) as functions of y for plate vibration (x = 63.5 cm, U_∞ = 18.5 m/s).....	122
5.18	Fluctuating velocity in the boundary layer (at 200 Hz) as a function of the excitation phase difference (phase of speaker minus phase of ribbon drive).....	126
5.19	Velocity fluctuations (at 200 Hz) as functions of y for ribbon excitation (x = 21.8 cm, U_∞ = 18.5 m/s).....	128
5.20	Velocity fluctuations (at 200 Hz) as functions of y for ribbon excitation (x = 27.9 cm, U_∞ = 18.5 m/s).....	129
5.21	Velocity fluctuations (at 200 Hz) as functions of y for ribbon excitation (x = 39.4 cm, U_∞ = 18.5 m/s).....	130
5.22	Boundary layer disturbance amplitudes (at $\beta = 56\times10^{-6}$) as functions of R (U_∞ = 18.5 m/s, f = 200 Hz).....	133
5.23	Boundary layer disturbance amplitudes (at $\beta = 56\times10^{-6}$) as functions of the Reynolds number (U_∞ = 18.5 m/s, f = 200 Hz).....	136
5.24	Sound excited boundary layer disturbance amplitudes (at $\beta = 56\times10^{-6}$) as functions of the Reynolds number (from Shapiro [7]).....	138
5.25	Intermittency as a function of streamwise Reynolds number (R_x).....	141
5.26	Velocity fluctuations (at 500 Hz) as functions of y, U_∞ = 29.0 m/s. (+ and ◈ are 10 times their actual magnitudes.).....	143
5.27	Sound pressure level (at 200 Hz) as a function of x under the test plate during the sound excitation tests (U_∞ = 18.5 m/s).....	147

Figure	Title	Page
5.28	Symmetric component of the fluctuating velocity (at 200 Hz) as a function of the distance from the plate's center during the sound excitation tests (U_∞ = 18.5 m/s).....	149
5.29	Antisymmetric component of the fluctuating velocity (at 200 Hz) as a function of the distance from the plate's center during the sound excitation tests (U_∞ = 18.5 m/s).....	150

NOMENCLATURE

a	parameter of the Joukouski mapping function
$A(x)$	boundary layer disturbance amplitude at x
A_0	boundary layer disturbance amplitude at x_0
c	sound speed
d	length scale for nondimensionalization of spectral densities
f	excitation frequency
f_0	first natural frequency of vibrating ribbon
$f(\bar{z})$	complex velocity potential in $\bar{z}$ plane ($f(\bar{z}) = \phi(\bar{z}) + i\psi(\bar{z})$)
$f(\bar{\zeta})$	complex velocity potential in $\bar{\zeta}$ plane ($f(\bar{\zeta}) = \phi(\bar{\zeta}) + i\psi(\bar{\zeta})$)
i	$\sqrt{-1}$
I	turbulent intermittency
k_x	wavenumber in x direction
k_z	wavenumber in z direction
L	typical dimension of the plate's leading edge
ℓ	typical dimension of cylinder in Lighthill's [42] analysis
p,P,p'	total, mean part and fluctuating part of the pressure, respectively
r_0	radius of circular cylinder in the complex $\bar{z}$ plane
R	boundary layer Reynolds number ($R = U_\infty \delta^*/\nu$)
R_x	streamwise Reynolds number ($R_x = U_\infty x/\nu$)
R_{xtr}	R_x at transition point ($I = 0.5$)
$R_{x,crit}$	R_x at critical point

t	time
u,v,w	x, y and z components of velocity, respectively
U,V,W	x, y and z components of mean velocity, respectively
u',v',w'	x, y and z components of fluctuating velocity, respectively
U_∞	free stream velocity
u_0,U_0,u_0'	total, mean part and fluctuating part of velocity outside the boundary layer, respectively
$\bar{u}$	amplitude of $\hat{u}'$ in the sound excited Orr-Sommerfeld problem
u'_f	excitation frequency component of u'
$\underline{V}$	vector velocity
$w(\bar{z})$	complex velocity in $\bar{z}$ plane ($w(\bar{z}) = u(\bar{z}) - iv(\bar{z})$)
$w(\bar{\zeta})$	complex velocity in $\bar{\zeta}$ plane ($w(\bar{\zeta}) = u(\bar{\zeta}) - iv(\bar{\zeta})$)
x,y,z	Cartesian coordinate system for the flat plate boundary layer
x_0	reference value of x
$\bar{z}$	complex plane for flow about a circular cylinder
α	nondimensional wavenumber in x direction ($\alpha = k_x\delta^*$)
α_r	real part of α
α_i	imaginary part of α
β	nondimensional frequency ($\beta = \omega\nu/U_\infty^2$)
β_r	real part of β
β_i	imaginary part of β
β_{FS}	Falkner-Skan parameter

γ	nondimensional wavenumber in z direction ($\gamma = k_z \delta^*$)
δ	boundary layer thickness
δ^*	boundary layer displacement thickness
∇	gradient operator
∇^2	Laplacian operator
∇^4	biharmonic operator
ε	sound wave amplitude in the sound excited Orr-Sommerfeld problem
ε_v	vertical velocity amplitude of circular cylinder in $\bar{z}$ plane
$\bar{\zeta}$	complex plane for flow about an elliptic cylinder
η	vertical coordinate in ζ plane
η_{max}	vertical amplitude of stagnation point motion for vibrating elliptic cylinder in cross flow
θ	argument of complex variable $\bar{z}$
κ	radius of curvature of the plate's leading edge
ν	fluid kinematic viscosity
ξ	horizontal coordinate in $\bar{\zeta}$ plane
ρ	fluid density
ϕ	velocity potential
$\phi_p(f)$	experimental sound pressure spectral density
$\phi_u(f)$	experimental velocity spectral density (x component)
$\bar{\phi}(\hat{y})$	amplitude function for v' in Orr-Sommerfeld equation
ψ	stream function
ψ'	perturbation stream function
ω	circular frequency

ω_0 intermediate value of frequency in Lighthill's [42] analysis

$\hat{}$ denotes dimensionless variable

I. INTRODUCTION

One of the most active areas of research in the field of fluid mechanics is the study of subsonic, laminar boundary layer transition. In many cases this research is directly applicable to a number of engineering design problems. There is considerable interest in developing techniques to delay the transition to turbulence in boundary layers. Even a modest delay of transition can represent a considerable decrease in drag and, therefore, a savings in propulsion costs. Delaying turbulence can also significantly decrease the vibratory excitation of sensitive structures such as sonar devices. A complete understanding of the events that lead to transition would be invaluable in the design of systems involving fluid flow at large Reynolds numbers. However, more research is necessary to adequately describe the transition process.

The transition to turbulence within a boundary layer is a very complex process and, owing to the large amount of research that has been completed, is reasonably well understood. However, some aspects of transition are still unclear. It is well known that there are four types of environmental perturbations that can have dramatic effects upon boundary layer transition, viz: 1) surface roughness,

2) free stream turbulence, 3) free stream sound, and 4) plate vibration. As an example, on a smooth flat plate with zero mean pressure gradient, the streamwise Reynolds number at which the boundary layer becomes turbulent (R_{xtr}) is normally about $2x10^6$. In contrast, if the perturbations are very carefully controlled, transition Reynolds numbers of up to $2.8x10^6$ (Schubauer and Skramstad [1]) and even as high as $5.2x10^6$ (Spangler and Wells [2]) have been reported. This notable variation in the transition Reynolds number indicates that boundary layer transition is very sensitive to changes in the environment.

Figure 1.1 shows the variation in transition Reynolds number with the fluctuating component of the streamwise velocity of the incoming flow u' for several experiments. (This figure was taken from Leehey [3].) All of these experiments were conducted on smooth surfaces in flows of nearly zero pressure gradient. One notes that there is a substantial variation in the reported data. The variation occurs because this interpretation tends to oversimplify the transition process. The value of u' in the free stream is often reported as the level of free stream turbulence, but it includes acoustic noise as well. The boundary layer reacts quite differently to acoustic excitation than it does to free stream turbulence. The frequency content of u', which is also important, is not included in the figure. The

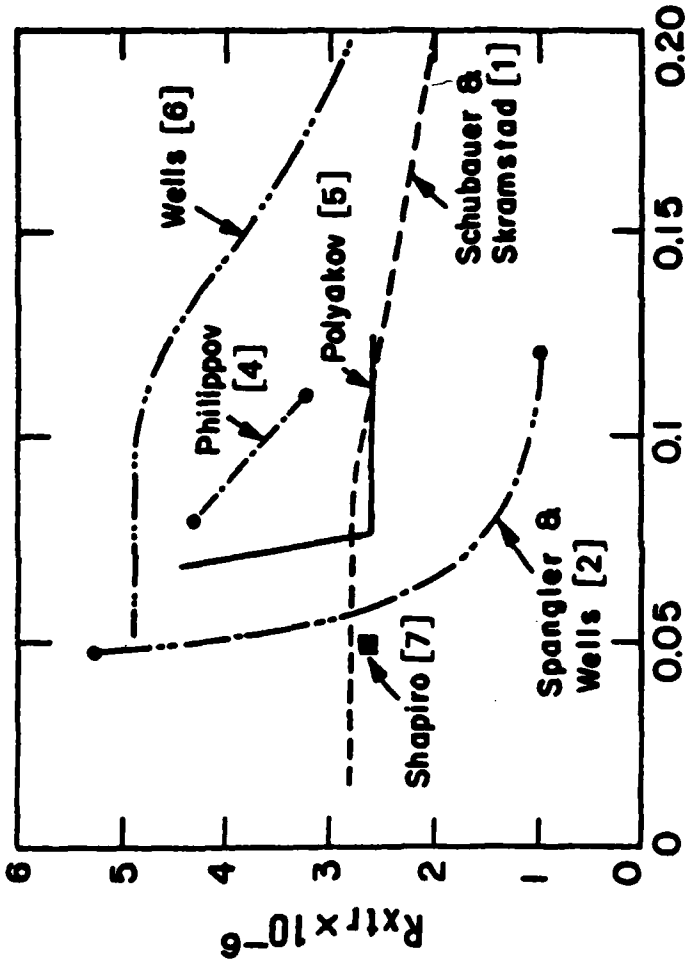

FIGURE 1.1 Transition Reynolds number (R_{xtr}) as a function of u'/U_∞ for several investigators (from Lechey [3]).

shapes and possible vibration of the bodies on which the data were taken is also missing in Figure 1.1. The influence of each of these factors on transition is very important and should be more closely examined before a proper interpretation of these results can be made.

The objective of the present research is to examine the effects of sound and wall vibration on the early stages of boundary layer transition. This will provide further insight into how these two excitations interact with a laminar boundary layer and how this interaction may eventually lead to the transition to turbulence.

This report is divided into six chapters. Chapter II presents a brief overview of the research in this field to date. Chapter III contains a review of the theoretical considerations that describe the early stages of transition and how sound and wall vibration influence this part of the transition process. Chapter IV describes the experimental instrumentation that was used and the experimental conditions under which the research was conducted. Chapter V contains the experimental results, including: 1) the natural excitation of the laminar boundary layer; 2) the response of the laminar boundary layer to sound, wall vibration, and a vibrating ribbon; 3) the cancellation of a sound-excited Tollmien-Schlichting wave with plate

vibration; and 4) a comparison of the growth of laminar boundary layer disturbances for the various excitation cases. Finally, Chapter VI contains an interpretation of the results and recommendations for further work.

II BACKGROUND

Boundary layer theory began with the clever observation of Prandtl [8] that, when the streamwise Reynolds number, R_x, is large, the Navier-Stokes equations may be approximated by the more simplified boundary layer equations. These equations were solved for a flat plate in the well known work of Blasius [9].

The stability of shear flows was first treated by Rayleigh [10], and the viscous laminar stability equation for parallel flow (commonly known as the Orr-Sommerfeld equation) was derived independently by Orr [11] and Sommerfeld [12]. Stability theory was greatly improved by Tollmien [13,14] and Schlichting [15-18], but it was not until the classic experiments of Schubauer and Skramstad [1] that the laminar boundary layer oscillations predicted by the stability theory were first observed. These oscillations are known as Tollmien-Schlichting waves (hereafter called "TS waves"). The properties of these waves were found to match the linear theory very well. More recently, calculations of the properties of TS waves were compared to experimental measurements in the works of Jordinson [19], Barry and Ross [20], and Ross et al [21] with excellent success.

The Orr-Sommerfeld equation together with its boundary conditions represents an eigenvalue problem and the TS wave is the only eigenfunction solution that is known to be unstable. Recent work [22-25] has shown that the eigenvalue problem for a boundary layer possesses a finite number of discrete eigenvalues along with a continuous spectrum. The effects of three-dimensionality and nonlinearity on boundary layer oscillations and transition have been studied [26-30], and found to be very important.

The influence of free stream perturbations (both sound and turbulence) and wall vibrations on boundary layer transition has received a considerable amount of attention in boundary layer research. Many investigators have studied this problem experimentally, with some surprising results. The effects of both free stream turbulence and sound were examined in the original experiments of Schubauer and Skramstad. They found that the transition Reynolds number increased with decreasing levels of free stream turbulence until R_{xtr} was 2.8×10^6 (see Figure 1.1). As the level of free stream turbulence was reduced further (below $u'/U_\infty = 0.1\%$), R_{xtr} remained constant. This peculiar behavior was attributed to acoustic noise in their tunnel, but the mechanism by which the sound interacted with the boundary layer was unknown. Schubauer and Skramstad went on to find that the point on their flat plate at which the boundary

layer became turbulent could be moved one to two feet upstream by the introduction of sound at the proper magnitude and frequency. The sound field they used was directed across the free stream, normal to the leading edge of their test plate. They also reported that, at a given Reynolds number, the sound frequency which caused the greatest amplification of fluctuations within the boundary layer matched the predicted frequency of the most amplified TS wave. Wells [6] and Spangler and Wells [2] have also investigated the effects of sound and free stream turbulence on boundary layer transition. The sound waves in their tests propagated in the streamwise direction. They found that the spectral content as well as the intensity of the acoustic perturbations had important effects on the transition Reynolds number. Spangler and Wells also found that traveling sound waves had a strong influence on transition, while standing sound waves did not.

A series of experimental investigations into the effects of wall motion and sound excitation on a laminar boundary layer were conducted by Schilz [31,32] and Mechel and Schilz [33]. In one set of tests, sound waves were beamed across the free stream normal to the leading edge of their flat plate. They reported that if the sound frequency was within the unstable TS wave frequency range, boundary layer distortions were excited, while suppression of the

distortions was observed for sound frequencies above this range. This suppression led to a significant reduction in the turbulent bursting at a point in the transition region of the boundary layer. Similar observations were reported in another set of tests, where a piston transducer was used to excite the boundary layer. This piston was flush-mounted into a section of the test plate near its leading edge. Schilz attributed this effect on the boundary layer to the sound emitted by the piston reflecting back onto the leading edge of the plate. Attributing the suppression to the influence of sound alone may not have been correct because no other experiments are known to support this conclusion. Schilz also conducted experiments in which transverse motions of the wall were used to excite the boundary layer. These wall motions were generated on a special "flexural wave" transducer that was flush-mounted into a section of the test plate. This transducer had a flexible surface which was forced to move in a transverse wave-like manner with a variety of frequencies and phase speeds. The phase speeds of this transducer were much slower than the speed of sound, so very little sound was generated. Schilz found that the excitation of the boundary layer became most effective when the frequency and phase speed of the wall motion coincided with those of an unstable TS wave.

Shapiro [7] measured the stability of laminar boundary

layer oscillations under sound excitation and compared the results to measurements taken without excitation (where, presumably, free stream turbulence was the only excitation). The sound excitation was a pure tone, plane wave propagating in the streamwise direction. He found that the growth of these oscillations was significantly higher with sound excitation than without it. This was attributed to the assumed form of the excited oscillation. The oscillation was thought to be a two-dimensional TS wave, propagating in the stream direction. It may be inferred from Squire's transformation [34] that a wave of this form is more highly amplified than one possessing lateral components, provided the maximum growth rate for the frequency in question has not yet been reached. Lin [35] gives a more complete transformation (which is valid anywhere in the parallel flow, and not just at the critical Reynolds number) from which the same conclusion may be reached. Without excitation, Shapiro assumed that the boundary layer oscillations were made up of many TS waves with random propagation directions, having slower growth rates. Shapiro also found that the amplitude of the boundary layer disturbance was linearly dependent on the sound excitation amplitude. In the region of the boundary layer upstream of the growth of disturbances, Shapiro discovered a standing spatial wave with a wavelength equal to that of the TS wave. Such standing waves had been discovered earlier by Kachanov

et al [36] who correctly interpreted them as resulting from the linear superposition of a sound wave and a TS wave of nearly equal amplitude, see also Thomas and Lekoudis [37]. However, for such a standing wave to occur, the phase of the TS wave at any point must be constant in time with respect to the phase of the sound wave. This means that the origin of the TS wave must be a fixed point in the boundary layer, which is most likely the leading edge of the plate.

The influence of sound on boundary layer oscillations was also studied experimentally by Kachanov et al [36]. Their tests were conducted in a manner that was similar to the work of Shapiro. They found that their sound field excited plate vibrations that were considered to be the major source of boundary layer excitation. Thus, these results are not directly comparable to Shapiro's because of the differences in the levels of plate vibration. Shapiro used a highly damped plate with a rms vibration level approximately 40 times smaller than the thin undamped plate used by Kachanov. Polyakov [5] also experimentally studied the excitation of boundary layer oscillations by streamwise propagating sound and by plate vibration. He found that these perturbations had a strong influence on the oscillations, particularly in the frequency range of unstable TS waves. He also found that the oscillations could be generated at harmonics and subharmonics of the

excitation frequency, presumeably due to a non-linear interaction.

Some experimental investigations have shown that artificially-excited boundary layer oscillations can be suppressed or cancelled with a secondary excitation. Schilz [32] excited a "boundary layer wave" with a vibrating ribbon and later forced his flexural wave transducer to move at the frequency and phase speed of the boundary layer wave, but in opposite phase. He found that this resulted in a significant amount of cancellation. Milling [38] was able to nearly cancel the "Tollmien-Schlichting type disturbances" that were generated in his water tunnel in a similar manner. In this experiment, vibrating wires were used to generate and later cancel the disturbances. Liepmann et al [39] used flush-mounted heating strips to both generate, and later cancel, a "laminar-instability wave," in water. Liepmann also reported that "extremely two-dimensional, naturally occurring TS waves" appeared in their water tunnel. These waves were nearly pure tone. Liepmann and Nosenchuck [40] used a single heating strip, activated by a hot film sensor, to suppress these naturally occurring TS waves. The hot film signal was processed and used to excite the heating strip through a feedback loop. The terms "boundary layer wave," "Tollmien-Schlichting type disturbance," and "laminar-instability wave" have all been

used to describe the disturbances in these cancellation experiments. Undoubtedly these disturbances are all TS waves, since all other eigenmodes are heavily damped.

Theoretical studies of the excitation of laminar flow by free stream perturbations (including sound) and plate vibration have provided many important insights into the physical phenomena that lead to turbulence. The stability of plane Poiseuille flow, subjected to a time periodic pressure gradient (the incompressible limit of a sound wave) was studied by Grosh and Salwen [41]. They found that small oscillations in the pressure gradient tended to stabilize the flow, while for larger amplitudes the oscillations destabilized the flow. This finding seems to contradict most boundary layer studies.

Lighthill [42] analyzed the incompressible flow in the laminar boundary layers of cylinders in which the incoming velocity contained a small oscillation in magnitude. He pointed out that this approximates the case when the fluid contains a small amplitude sound wave propagating in the stream direction, if the wavelength is large compared to any dimension of the cylinder. He also stated that this analysis applies to fluctuations in the flow arising from oscillations of the body parallel to a steady, incompressible stream. Lighthill obtained two approximate

solutions to the flow field for high and low values of the Strouhal number, $\hat{\omega}$ ($\hat{\omega}=\omega\ell/U_\infty$, where: ω is the circular frequency, ℓ is a characteristic body dimension, and U_∞ is the mean value of the incoming velocity.) In the high Strouhal number limit, the approximate solution is that of a Stokes shear-wave, unaffected by the mean flow. The low Strouhal number approximation was obtained using the Kármán-Pohlhausen method to solve the governing equations. These approximations were calculated for a Blasius boundary layer and for a stagnation point flow (also know as a Hiemenz layer), at an intermediate value of the frequency ω_0 (corresponding to an intermediate value of the Strouhal number). ω_0 was found to be dependent upon U_∞, ℓ, and the cylinder geometry. $\omega_0=0.6U_\infty/x$ for a Blasius layer and $\omega_0=5.6U_0(x)/x$ for a Hiemenz layer, where $U_0(x)$ is the mean value of the velocity along the wall outside the boundary layer. Lighthill showed that the high and low Strouhal number approximations are in reasonably good agreement for these two cases at $\omega=\omega_0$. Lin [43] independently carried out an analysis that was similar to that of Lighthill, with the exception that finite amplitude oscillations in the free stream velocity were considered.

Lighthill's theory has been improved greatly by many theoretical investigators (most notably, in References 44 through 47). These improvements have usually involved

better approximations to the oscillatory flow in a flat plate boundary layer when the Strouhal number is in the intermediate range. The existence of a "double boundary layer" [45] (in the linear approximation) has been discovered in the downstream portion of the flow. In this double layer the shear waves (or Stokes shear-waves) and the Blasius flow, with its TS wave oscillation, were found to coexist independently. Patel [46] expanded the theory to allow for disturbances in the free stream propagating at a finite phase velocity. Goldstein [47] analyzed the oscillatory flows in the boundary layer of an infinitely thin flat plate. He demonstrated that asymptotic solutions of the unsteady boundary layer equation match onto solutions of the Orr-Sommerfeld equation. (The unsteady boundary layer equation is valid near the leading edge, while the Orr-Sommerfeld equation applies in a region further downstream.) He goes on to show that small streamwise oscillations in the mean flow generate disturbances near the leading edge of the plate, in the unsteady boudary layer region, which in turn couple into a TS wave in the Orr-Sommerfeld region. The leading edge of the test plate is, therefore, of prime importance in the generation of TS waves by free stream disturbances. The magnitude of the TS wave predicted by this theory is, however, considerably smaller than the level measured by Shapiro.

Numerical investigations into the generation of TS waves by streamwise propagating sound waves on flat plates, and parabolic cylinders have been conducted by Murdock [48,49]. These investigations also demonstrate the importance of the leading edge of the plate in determining the eventual TS wave magnitude. Again, the TS wave amplitude predicted for a flat plate was much less than the measurements of Shapiro. The effect of a finite leading edge radius, as demonstrated by the parabolic cylinders, tended to decrease the amplitude of the TS wave. It should be noted that for a parabolic cylinder there is no region of adverse pressure gradient as there was in Shapiro's tests.

The effect of surface motion on the boundary layer was analyzed by Aizin and Volodin [50]. They studied the stability of two-dimensional, temporally growing disturbances in the incompressible flow over a flat surface, where the surface was perturbed by a small sinusoidal wave, traveling in the flow direction. The wavenumber and phase speed of the surface wave did not correspond to any of the eigenvalues of the stability problem. The position of the neutral stability curve, as a function of the Reynolds number and the wavenumber of the flow disturbance, was computed for several combinations of wavenumber, phase velocity, and amplitude of the surface wave. The influence of the surface wave on the neutral stability curve was found

to be negligible, except in a small region near the point where the frequency and wavenumber of the flow disturbance were approximately equal to the frequency and wavenumber of the surface wave. Typical bending wavelengths in metal plates are much larger than the TS wavelengths and, therefore, it is unlikely that this type of near coincidence would be observed (except in special cases such as with the flexural wave transducer of Schilz). Also, the applicability of this analysis to a physical boundary layer is questionable, since the solution is written in a coordinate system moving with respect to the plate. In the moving coordinates the parallel flow assumption is more likely to be invalid, and the proper velocity profile would change with time.

Only a portion of the large amount of the research conducted in this field has been presented here. However, even in the research that was discussed, many phenomena still remain unclear. The present research will attempt to clarify some of these questions.

III. THEORETICAL CONSIDERATIONS

The process of transition to turbulence within a boundary layer is depicted in Figure 3.1, which was adapted from White [51]. This sketch is for transition at subsonic speeds on a smooth, stationary flat plate in a low-turbulence, constant-temperature fluid with low acoustic levels and no pressure gradient over the plate. The boundary layer is stable and laminar over the initial portion of the plate and is described very well by the Blasius solution (except at the leading edge of the plate, which is a singular point in the theory). Downstream of the critical point, certain types of boundary layer oscillations are unstable. (These oscillations are TS waves and they are described in detail below.) In some cases, the initial boundary layer disturbances may be large enough (from sound or plate vibration, say) that the TS waves quickly become non-linear and the flow very rapidly becomes turbulent [52], or the flow may immediately become turbulent with no evidence of TS waves at all. However, if the initial disturbances are small, some TS waves will grow and decay, while others will eventually grow large enough for the boundary layer to develop spanwise vorticity and then three-dimensional vortex breakdown. Small spots of turbulence then begin appearing in the boundary layer.

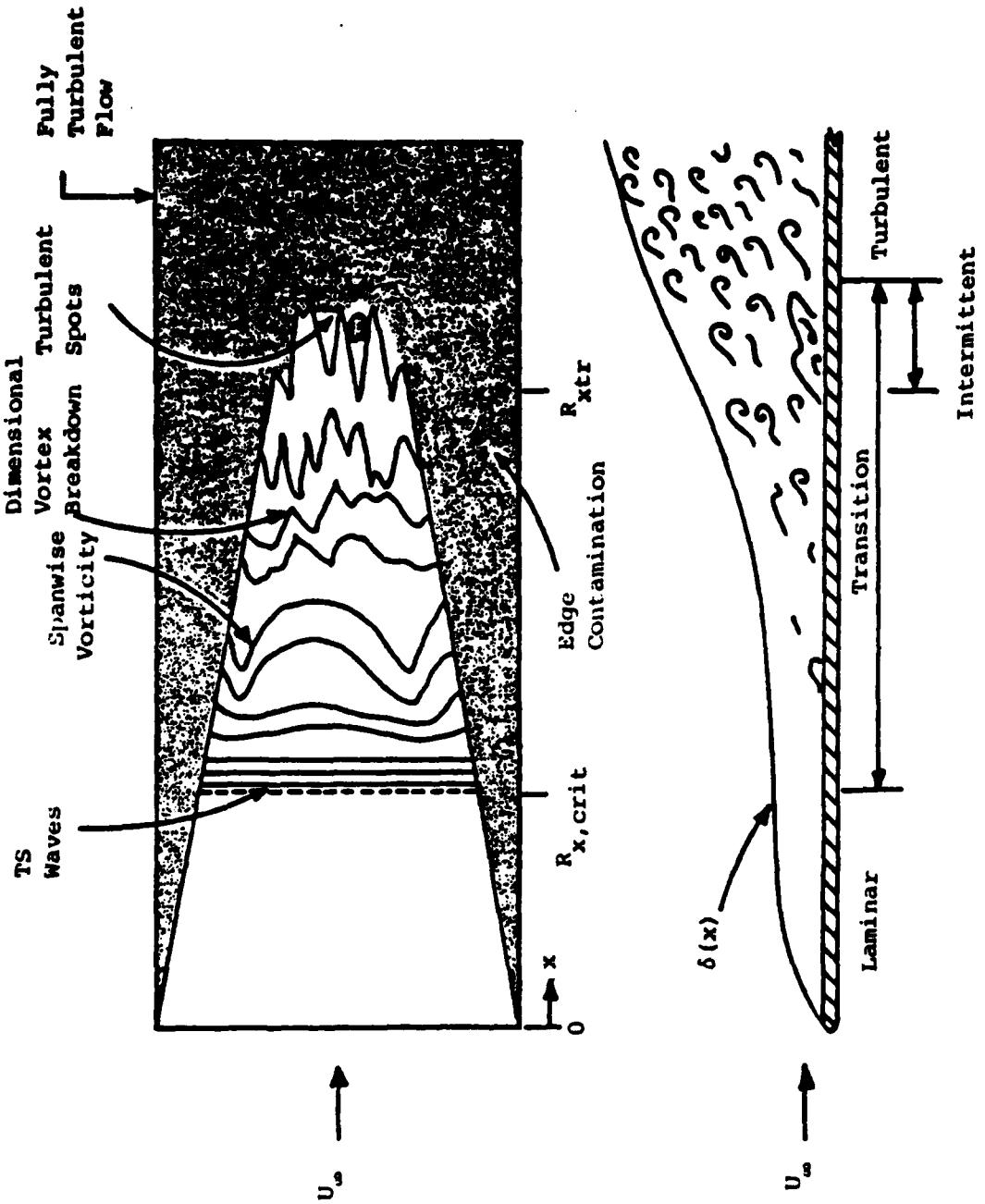

FIGURE 3.1 Transition to turbulence on a flat plate (from White [51]).

These spots grow as they convect downstream and soon the boundary layer becomes fully turbulent.

The focus of the present research is on how the perturbations (free stream sound and plate vibration) interact with a laminar boundary layer and how this interaction influences the initial stages of the transition process. There are two separate ways in which the perturbations may interact with a boundary layer. A disturbance may be generated in the laminar flow by the perturbation and then feed the instabilities that lead to transition (as in Goldstein's theory, for example). The perturbation may also influence the actual stability of the flow (even though the linear theory predicts that a Stokes shear-wave and a TS wave are completely decoupled in the double layer).

The linear stability analysis of a laminar boundary layer is a well known problem in fluid mechanics. A complete discription of this analysis is given in Schlichting [53], but a brief outline will be given here. The non-dimensional continuity and momentum (or Navier-Stokes) equations for subsonic motion of an incompressible, Newtonian, constant viscosity fluid with negligible thermal, buoyancy, and gravitational effects can be written as follows:

$$\nabla \cdot \hat{\underline{V}} = 0 \tag{3.1}$$

$$\frac{\partial \hat{\underline{V}}}{\partial \hat{t}} + \hat{\underline{V}} \cdot \nabla \hat{\underline{V}} = - \nabla \hat{p} + \frac{1}{R} \nabla^2 \hat{\underline{V}} \tag{3.2}$$

In the boundary layer problem, the non-dimensionalization is done with the displacement thickness (δ^*) and the free stream velocity (U_∞). The hats ($\hat{}$'s) signify dimensionless variables. The $\hat{x},\hat{y},\hat{z}$ coordinate system is defined in Figure 3.2, and $\hat{t}$ is time. $\hat{\underline{V}}$ is the vector velocity of the fluid and $\hat{p}$ is the pressure, and, in general, both of these variables are functions of $\hat{x},\hat{y},\hat{z}$ and $\hat{t}$. R is the boundary layer Reynolds number, defined as $R=U_\infty \delta^*/\nu$, where ν is the kinematic viscosity of the fluid. $\hat{u}$, $\hat{v}$, and $\hat{w}$ will be used to represent the $\hat{x}$, $\hat{y}$, and $\hat{z}$ components of $\hat{\underline{V}}$, respectively. The stability analysis of the flow begins by expressing the three velocity components and the pressure in terms of their mean and fluctuating parts:

$$\hat{u} = \hat{U} + \hat{u}'$$

$$\hat{v} = \hat{V} + \hat{v}'$$

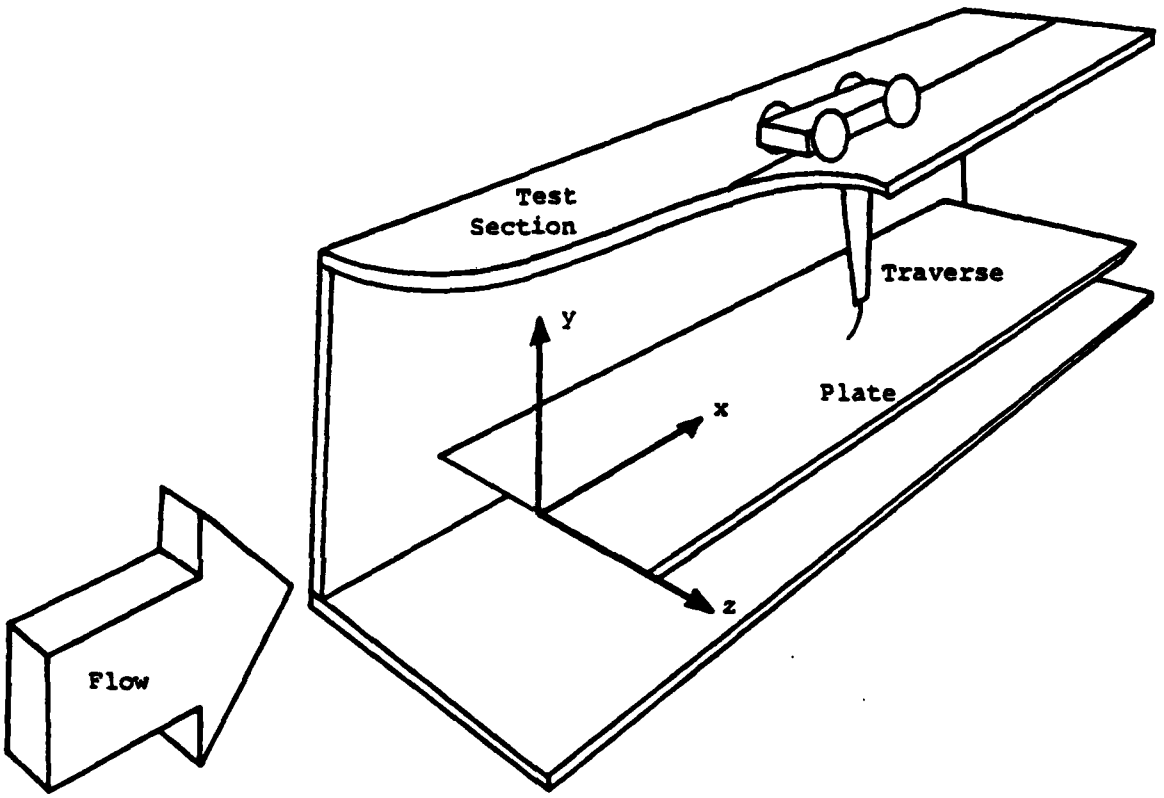

FIGURE 3.2 Sketch of the x,y,z coordinate system inside the wind tunnel test section.

$$\hat{w} = \hat{W} + \hat{w}' \qquad (3.3)$$

$$\hat{p} = \hat{P} + \hat{p}'$$

Where the primes denote fluctuating parts and the capitals denote the mean, or time-averaged parts. These expressions are inserted into equations (3.1) and (3.2). The resulting equations are then time averaged to obtain a new set of equations. This new set of equations is subtracted from the first set, yielding equations for the fluctuating quantities. In the stability analysis the disturbance is assumed to be infinitesimally small, hence the resulting equations are linearized with respect to the fluctuating quantities. In the boundary layer problem $\hat{V}$ and $\hat{W}$ are zero and $\hat{U}$ is assumed to be a function of $\hat{y}$ only. This approximation is good only if $\hat{U}$ is a slowly varying function of $\hat{x}$, which, for a flat plate boundary layer, is not true near the leading edge of the plate. In the downstream portion of the plate this approximation is appropriate [20]. With these approximations, the equations become

$$\frac{\partial \hat{u}'}{\partial \hat{x}} + \frac{\partial \hat{v}'}{\partial \hat{y}} + \frac{\partial \hat{w}'}{\partial \hat{z}} = 0, \tag{3.4a}$$

$$\frac{\partial \hat{u}'}{\partial \hat{t}} + \hat{U}\frac{\partial \hat{u}'}{\partial \hat{x}} + \hat{v}\frac{d\hat{U}}{d\hat{y}} = -\frac{\partial \hat{p}'}{\partial \hat{x}} + \frac{1}{R}\nabla^2\hat{u}' \tag{3.4b}$$

$$\frac{\partial \hat{v}'}{\partial \hat{t}} + \hat{U}\frac{\partial \hat{v}'}{\partial \hat{x}} = -\frac{\partial \hat{p}'}{\partial \hat{y}} + \frac{1}{R}\nabla^2\hat{v}' \tag{3.4c}$$

$$\frac{\partial \hat{w}'}{\partial \hat{t}} + \hat{U}\frac{\partial \hat{w}'}{\partial \hat{x}} = -\frac{\partial \hat{p}'}{\partial \hat{z}} + \frac{1}{R}\nabla^2\hat{w}' \tag{3.4d}$$

Equations (3.4) are then combined to obtain a single expression for $\hat{v}'$, viz:

$$\left(\frac{\partial}{\partial \hat{t}} + \hat{U}\frac{\partial}{\partial \hat{x}}\right)\nabla^2\hat{v}' - \frac{d^2\hat{U}}{d\hat{y}^2}\frac{\partial \hat{v}'}{\partial \hat{x}} = \frac{1}{R}\nabla^4\hat{v}' \tag{3.5}$$

Equation (3.5) is a fourth order, linear, partial differential equation for $\hat{v}'$ in terms of $\hat{x}, \hat{y}, \hat{z}$ and $\hat{t}$ ($\hat{U}$ is a known function of $\hat{y}$, from the Blasius solution). The boundary conditions for $\hat{v}'$ are

$$\hat{v}' = \frac{\partial \hat{v}'}{\partial \hat{y}} = 0 \text{ at } \hat{y} = 0 \tag{3.6}$$

and $\hat{v}', \frac{\partial \hat{v}'}{\partial \hat{y}}$ are bounded as $\hat{y} \to \infty$ (3.7)

The Orr-Sommerfeld equation may now be obtained by assuming a wave-like behavior of the perturbation $\hat{v}'$. That is, assume $\hat{v}'$ is represented by the real part of the function

$$\hat{v}' = \bar{\phi}(\hat{y}) \exp\{i(\alpha\hat{x} + \gamma\hat{z} - \beta\hat{t})\} \tag{3.8}$$

where α and γ are the complex, dimensionless wavenumbers in the $\hat{x}$ and $\hat{z}$ directions; β is the complex, dimensionless frequency; and $\bar{\phi}$ is an unknown function of $\hat{y}$. The complex, dimensionless parameters (α, γ, β) can be written in terms of their dimensional counterparts (k_x, k_z, ω) as follows:

$$\alpha = k_x \delta^*$$

$$\gamma = k_z \delta^* \tag{3.9}$$

and $\beta = \omega \nu / U_\infty^2$

From Squire [34] and Lin [35] we find that the most unstable disturbance (prior to the maximum growth rate) for a two-dimensional, parallel flow is a two-dimensional disturbance propagating in the flow direction. The spanwise variation, γ, will therefore be neglected. Equation (3.8) represents a small disturbance that is to be introduced into a steady laminar boundary layer. This form of disturbance is specialized, but since the problem is linear, Fourier superposition can be used to represent distubances of any form in the $\hat{x}$, $\hat{z}$, and $\hat{t}$ dimensions, as in Gaster [54]. The form of the solution for $\bar{\phi}(\hat{y})$ is needed in order to determine whether an arbitrary upstream boundary condition may be represented by superposition in the $\hat{y}$ direction. Neglecting γ, equation (3.8) may be inserted into equation (3.5) to yield the Orr-Sommerfeld equation:

$$(\alpha \hat{U}(\hat{y}) - \beta)\left(\frac{d^2}{d\hat{y}^2} - \alpha^2\right)\bar{\phi} - \alpha \frac{d^2\hat{U}}{d\hat{y}^2}\bar{\phi} = \frac{-i}{R}\left(\frac{d^2}{d\hat{y}^2} - \alpha^2\right)^2 \bar{\phi} \tag{3.10}$$

with boundary conditions for $\bar{\phi}$:

$$\bar{\phi} = \frac{d\bar{\phi}}{d\hat{y}} = 0 \quad \text{at } \hat{y} = 0, \tag{3.11}$$

and $\bar{\phi}$, $\frac{d\bar{\phi}}{d\hat{y}}$ are bounded as $y \to \infty$. (3.12)

Equation (3.10) is a fourth order, ordinary differential equation for $\bar{\phi}(\hat{y})$, with parameters $\hat{U}(\hat{y})$, R, α and β. Equations (3.10) through (3.12) represent an eigenvalue problem. For the boundary layer, $\hat{U}(\hat{y})$ and R are determined by the mean flow, and either α or β may be chosen arbitrarily. If α is selected to be real (temporal problem), β is a complex eigenvalue and the growth or decay of $\hat{v}'$ is temporal. Conversely, if β is selected to be real (spatial problem), α is a complex eigenvalue and the growth or decay of $\hat{v}'$ is spatial (with $\hat{x}$). The temporal problem is often done in theoretical calculations because it is easier to solve. However, in experimental investigations disturbances are introduced into the flow at a particular, real frequency and the spatial problem is applicable. Today, the solution of equation (3.10) is done numerically and many sophisticated schemes have been devised

[19,20,22-25,55,59] to obtain solutions. The numerical code developed by Orszag [55] was kindly given to us and the numerical results in Chapter V were computed using this code.

As was noted in Chapter II, this eigenvalue problem, when applied to the Blasius boundary layer, possesses a finite set of discrete eigenvalues and a continuous eigenvalue spectrum. Salwen and Grosch [25] have shown that the discrete and continuous eigenfunctions for the temporal problem form a complete, orthogonal set, so that any arbitrary disturbance can be represented by a superposition of expressions in the form of equation (3.8). The initial value problem of equation (3.10) (in the temporal sense) is then completely tractable. The spatial problem was also treated by Salwen and Grosch. In this case, the discrete and continuous eigenfunctions are orthogonal and complete, with the requirement that the disturbance (represented by equation (3.8)) be orthogonal to non-physical eigenfunctions (those which propagate upstream from $\hat{x}=-\infty$ or whose amplitude increase as $\hat{x}$ increases). With these restrictions, the boundary value problem of equation (3.10) (in the spatial sense) is also tractable. More research into the physical implications of these restrictions is clearly needed. Wasow [56-58] also treated the completeness of the eigenfunctions for the spatial problem in "the full complex neighborhood"

of a complex solution point (at the critical layer).

The most studied and the only unstable eigenfunction for this problem is the (discrete) TS wave. Spatial solutions for the TS wave have been presented in many ways [19,59]. Figure 3.3 is a plot of the imaginary part of the TS wave eigenvalue divided by R, α_i/R, as a function of R and β (recall β is real in the spatial problem) for the Blasius boundary layer. Figure 3.3 was taken from Obremski et al [59]. The points at which α_i is zero are called the neutral stability curve and at these conditions the disturbance neither grows or decays. Figure 3.3 shows this curve along with the regions where the disturbance is stable and unstable. Figure 3.4 shows the TS wave eigenfunction $(\bar{\phi}(\hat{y}))$ for R=1400 and $\beta=56\times10^{-6}$.

Thus far, only a Blasius boundary layer flow has been considered. Experimentally, the zero pressure gradient condition is impossible to maintain over the entire length of a test plate. Non-zero pressure gradients may substantially distort the boundary layer profile $\hat{U}(\hat{y})$ and the Orr-Sommerfeld problem will change. Obremski has computed solutions to several non-zero pressure gradient flows (Falkner-Skan flows). To make accurate comparisons between experiments and theoretical calculations, the pressure gradient must be considered.

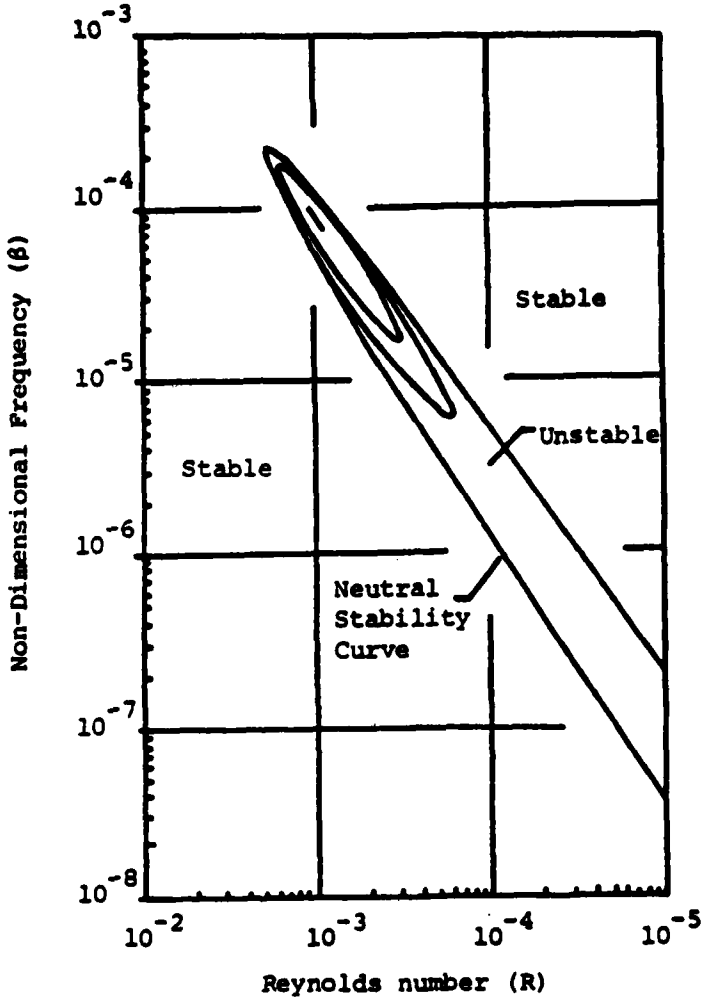

FIGURE 3.3 Disturbance stability $(\frac{\alpha_i}{R})$ for the spatial, flat plate Orr-Sommerfeld problem as a function of Reynolds number and frequency (from Obremski et. al. [59]).

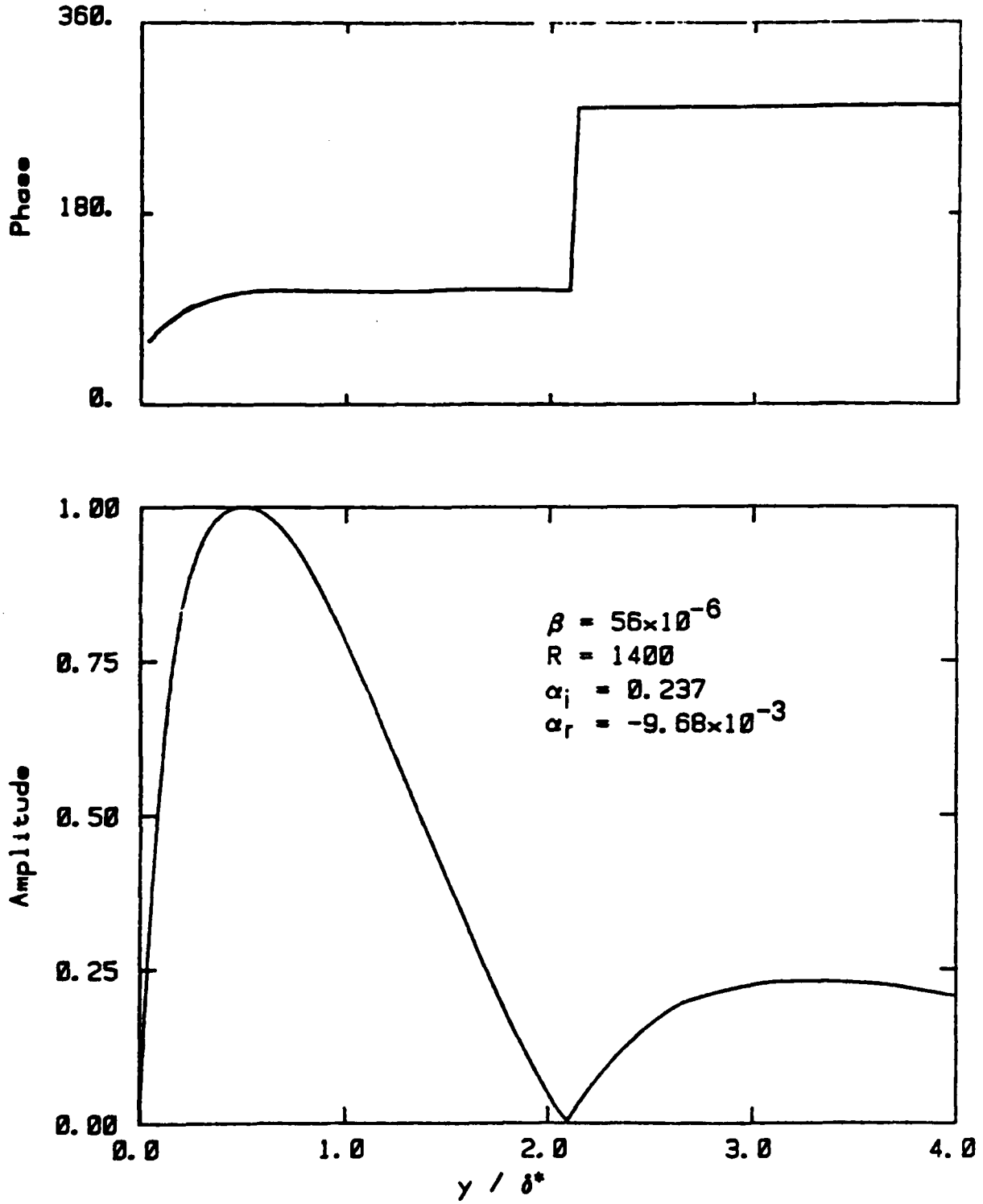

FIGURE 3.4 Magnitude and phase of the eigenfunction, $\bar{\phi}(\hat{y})$, for the spatial, flat plate Orr-Sommerfeld problem.

One final property of the Orr-Sommerfeld problem will now be considered. Suppose the disturbance in the boundary layer flow is a sound wave propagating in the $\hat{x}$ direction. In the incompressible (low frequency) limit its wavenumber vanishes. Since the mean flow and the disturbance are now two-dimensional, equations (3.4a,b,c) become

$$\frac{\partial \hat{u}'}{\partial \hat{x}} + \frac{\partial \hat{v}'}{\partial \hat{y}} = 0, \tag{3.13a}$$

$$\frac{\partial \hat{u}'}{\partial \hat{t}} + \hat{U}\frac{\partial \hat{u}'}{\partial \hat{x}} + \hat{v}'\frac{d\hat{U}}{d\hat{y}} = -\frac{\partial \hat{p}'}{\partial \hat{x}} + \frac{1}{R}\nabla^2\hat{u}', \tag{3.13b}$$

$$\frac{\partial \hat{v}'}{\partial \hat{t}} + \hat{U}\frac{\partial \hat{v}'}{\partial \hat{x}} = -\frac{\partial \hat{p}'}{\partial \hat{y}} + \frac{1}{R}\nabla^2\hat{v}'. \tag{3.13c}$$

Defining a perturbation stream function, ψ', by

$$\hat{u}' = \frac{\partial \psi'}{\partial \hat{y}}, \tag{3.14a}$$

and $$\hat{v}' = -\frac{\partial \psi'}{\partial \hat{x}}, \tag{3.14b}$$

automatically solves equation (3.13a). Inserting ψ' into (3.13b) and (3.13c) and eliminating $\hat{p}'$ yields

$$\left(\frac{\partial}{\partial \hat{t}} + \hat{U}\frac{\partial}{\partial \hat{x}}\right)\nabla^2\psi' - \frac{d^2\hat{U}}{d\hat{y}^2}\frac{\partial\psi'}{\partial\hat{x}} = \frac{1}{R}\nabla^4\psi' \qquad (3.15)$$

If a wave-like expression for ψ' is inserted into equation (3.15), the Orr-Sommerfeld equation is again obtained:

$$(\alpha\hat{U}(\hat{y}) - \beta)\left(\frac{d^2}{d\hat{y}^2} - \alpha^2\right)\bar{\phi} - \alpha\frac{d^2\hat{U}}{d\hat{y}^2}\bar{\phi} \qquad (3.10)$$

$$= \frac{-i}{R}\left(\frac{d^2}{d\hat{y}^2} - \alpha^2\right)^2\bar{\phi},$$

where now, (3.16)

$$\psi' = \bar{\phi}(\hat{y})\exp\{i(\alpha\hat{x} - \beta\hat{t})\}.$$

For the sound wave disturbance, $\alpha=0$ and equation (3.10) becomes

$$\frac{d^4\bar{\phi}}{d\hat{y}^4} + i\beta R\frac{d^2\bar{\phi}}{d\hat{y}^2} = 0, \qquad (3.17)$$

and β is real for the sound wave. Further,

$$\hat{v}' = -\frac{\partial \psi'}{\partial \hat{x}} = 0 \tag{3.18a}$$

$$\text{and} \quad \hat{u}' = \frac{\partial \psi'}{\partial \hat{y}} = \frac{d\bar{\phi}}{d\hat{y}} \exp(-i\beta\hat{t}), \tag{3.18b}$$

so that equation (3.17) may be rewritten as

$$\frac{d^3\bar{u}}{d\hat{y}^3} + i\beta R \frac{d\bar{u}}{d\hat{y}} = 0 \tag{3.19}$$

$$\text{where} \quad \hat{u}' = \bar{u}(\hat{y}) \exp(-i\beta\hat{t}), \tag{3.20}$$

with boundary conditions

$$\bar{u} = 0 \text{ at } \hat{y} = 0, \tag{3.21a}$$

$$\left.\begin{aligned} \bar{u} &\to \epsilon \\ \frac{d\bar{u}}{d\hat{y}} &\to 0 \end{aligned}\right\} \text{ as } y \to \infty. \tag{3.21b}$$

(ϵ is the sound wave amplitude.)

The solution of equation (3.19), subject to the boundary conditions (3.21), is precisely the Stokes shear-wave obtained in the high Strouhal number approximation of Lighthill [42]. This solution satisfies the Orr-Sommerfeld equation for $\alpha=0$ and any real frequency β. Therefore, it is not surprising that the Stokes shear-wave and the TS wave are completely decoupled in the double layer region for the linear approximation.

Solutions to the Orr-Sommerfeld equation only apply to parallel flow, and are appropriate only in the downstream portion of the flat plate boundary layer. Near the leading edge of the plate the unsteady boundary layer equations must be used. This was done in the low frequency approximation of Lighthill [42], and in the asymptotic analysis of Goldstein [47]. The boundary layer approximation (in two dimensions) to equations (3.1) and (3.2) is as follows:

$$\frac{\partial \hat{u}}{\partial \hat{x}} + \frac{\partial \hat{v}}{\partial \hat{y}} = 0, \tag{3.22a}$$

$$\frac{\partial \hat{u}}{\partial \hat{t}} + \hat{u}\frac{\partial \hat{u}}{\partial \hat{x}} + \hat{v}\frac{\partial \hat{u}}{\partial \hat{y}} = \frac{\partial \hat{u}_0}{\partial \hat{t}} + \hat{u}_0\frac{\partial \hat{u}_0}{\partial \hat{x}} + \frac{1}{R}\frac{\partial^2 \hat{u}}{\partial \hat{y}^2}, \tag{3.22b}$$

where $\hat{u}(\hat{x},\hat{t})$ is the velocity just outside the boundary layer. These expressions apply to a curved plate if $\hat{x}$ and $\hat{y}$ are curvilinear coordinates with $\hat{y}$ normal to the plate, and if the radius of curvature is much larger than the boundary layer thickness. $\hat{u}$, $\hat{v}$ and $\hat{u}_0$ may be expressed as the sum of mean and fluctuating components and equations (3.22) may then be expressed in terms of the fluctuating quantities (in linearized form, as in equations (3.4)) as follows:

$$\frac{\partial \hat{u}'}{\partial \hat{x}} + \frac{\partial \hat{v}'}{\partial \hat{y}} = 0 \tag{3.23a}$$

and
$$\frac{\partial \hat{u}'}{\partial \hat{t}} + \hat{U}\frac{\partial \hat{u}'}{\partial \hat{x}} + \hat{u}'\frac{\partial \hat{U}}{\partial \hat{x}} + \hat{v}'\frac{\partial \hat{U}}{\partial \hat{y}} \tag{3.23b}$$
$$= \frac{\partial \hat{u}'_0}{\partial \hat{t}} + \hat{U}_0\frac{\partial \hat{u}'_0}{\partial \hat{x}} + \hat{u}'_0\frac{\partial \hat{U}_0}{\partial \hat{x}} + \frac{1}{R}\frac{\partial^2 \hat{u}'}{\partial \hat{y}^2}$$

where $u_0 = U_0 + u'_0$.

Goldstein demonstrated that asymptotic solutions to these equations can be matched onto solutions of the Orr-Sommerfeld equation. He also demonstrated that a streamwise disturbance in the free stream couples onto the asymptotic solutions of (3.23) one of which then leads to a TS wave. The amplitude of the predicted TS wave is significantly less than the measurements of Shapiro. There

are two reasons for this discrepancy. First, the theory of Goldstein is for an infinitely thin flate plate, and should be modified to include the leading edge curvature and pressure gradients that were present in Shapiro's test. Finally, the acoustic behavior of Shapiro's test section caused the sound perturbations in the flow above and below the leading edge of the plate to have different phases (see Section 5.8) This means that the disturbance at the leading edge of Shapiro's test plate consisted of two parts: a symmetric disturbance (as in Goldstein's theory), and an antisymmetric disturbance where the symmetry is with respect to the plane at the center of the plate's thickness. The effects of these two disturbances may be superimposed since, as Goldstein and Shapiro have found, the TS wave excitation is linear in the case of small disturbances. It should also be noted that transverse oscillations of the plate's leading edge will produce an antisymmetric disturbance. An analysis into the effects of the antisymmetric disturbance is needed.

An estimate of the influence of antisymmetric disturbances may be obtained by considering the potential flow near the extreme leading edge of the test plate. The antisymmetric disturbances will cause the stagnation point to move and the magnitude of this motion will indicate the relative effect that the excitation has on the boundary layer. The Appendix contains approximate potential flow

calculations for the plate vibration case. The antisymmetric disturbance due to the acoustic excitation is examined in Section 5.8.

IV. EXPERIMENTAL APPARATUS

4.1 Wind Tunnel

The experimental measurements of Chapter V were undertaken in the wind tunnel facility of the M.I.T. Acoustics and Vibration Laboratory. This facility is a low-noise, low-turbulence, open circuit wind tunnel with a flow speed range of 10 to 50 m/s and a free stream turbulence level of approximately 0.05%. Figure 4.1 is an elevation view of the wind tunnel. The intake section of the tunnel consists of a honeycomb flow straightener, followed by seven 16x18 mesh and two 24 mesh screens for turbulence reduction. The screens are followed by a contraction section with a 20:1 area ratio, which leads to a 38 cm square test section duct that is 183 cm long. The test section is completely enclosed in an airtight blockhouse whose walls, ceiling, and floor are acoustically treated. The flow exits the blockhouse via a muffler-diffuser and is drawn by a centrifugal blower powered by a 14.9 kilowatt DC motor. The flow speed is controlled by varying the speed of the motor.

The original design and construction of this wind tunnel is discussed in Hanson [60]. After the work of Hanson, Shapiro [7] modified the wind tunnel to allow

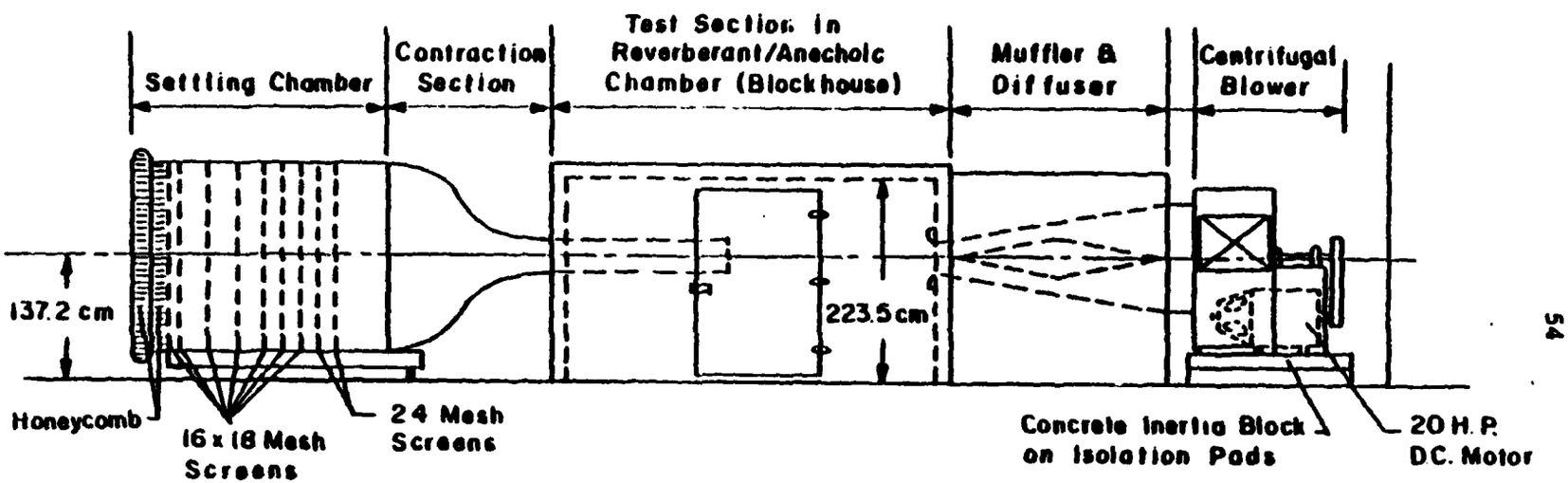

General Specifications:
Contraction Ratio: 20:1
Test Section: 38cm x 38cm, shown in open duct configuration

FIGURE 4.1

WIND TUNNEL FACILITY — ROOM 5-024
ACOUSTICS & VIBRATIONS LABORATORY
MASSACHUSETTS INSTITUTE OF TECHNOLOGY

studies of transition phenomena. Shapiro added a substantial treatment of noise and vibration abatement materials to the tunnel, and extended the settling chamber. Though Hanson and Shapiro give detailed descriptions of the wind tunnel, some of the important characteristics will be reviewed here.

The spectral densities of the u' component of the free stream velocity in the wind tunnel at three test speeds are shown in Figure 4.2. At 29 and 41 m/s there are no peaks in the spectra above 3 Hz. At 18.5 m/s, the u' spectrum has peaks at 1150 Hz and 1420 Hz, which will be explained below. The 3 Hz peaks in each of the spectra were caused by a Helmholtz resonance in the tunnel circuit. During the experiments, the test section exited into the blockhouse (this is called an "open-jet" configuration). The u' oscillation associated with this resonance is, therefore, acoustic and should not be treated as free stream turbulence. The tests were conducted at $\beta=56\times10^{-6}$ (that is, at 200 Hz and 18.5 m/s, at 500 Hz and 29.0 m/s, and by Shapiro at 1000 Hz and 41.0 m/s). The peaks in the spectra are not in the frequency range of unstable TS waves for a flat plate boundary layer (approximately 29 Hz to 790 Hz at 18.5 m/s and up to 3900 Hz at 41 m/s, for R<3000, see Figure 3.3), and were not considered to be detrimental to the experiments. Spangler and Wells [2] noted a similar low

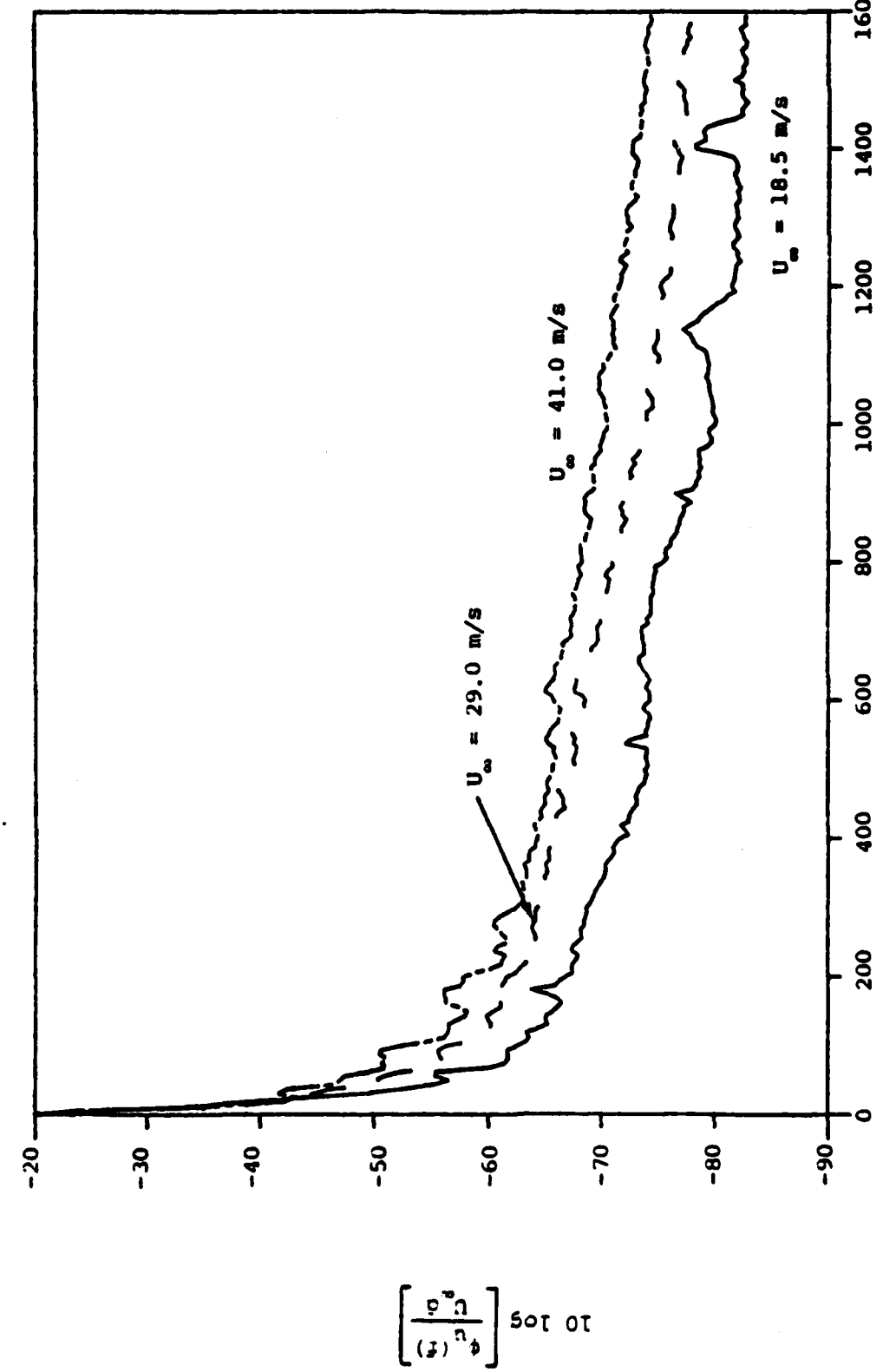

FIGURE 4.2 Spectral densities of the velocity fluctuations (u') in the free stream for three mean velocities at x = 0 and y = 3.0 cm (d = 1.1 mm, the mesh length of the turbulence reduction screens).

frequency resonance in their tunnel and found that lowering the resonance level by 10 dB had no effect on the transition Reynolds number. The measured level of u'/U_∞ depended strongly on the low frequency cutoff of the instrumentation. At 41 m/s, with a low frequency cutoff of 10 Hz, u'/U_∞ was 0.04%. With a 4 Hz cutoff, u'/U_∞ was 0.07% and with a 1 Hz cutoff, u'/U_∞ was 0.16%. The variation in u'/U_∞ with free stream velocity is shown in Figure 4.3. An 8 Hz cutoff frequency was used to obtain the data in Figure 4.3.

The acoustic treatment has been effective in reducing the unwanted acoustic disturbances in the free stream. As was stated above, the experiments were conducted with the wind tunnel in an open-jet configuration. This allowed the noise that was generated in the flow to propagate into the blockhouse and be absorbed by the acoustic treatment. The blockhouse treatment was designed by Moeller [61], who found it to be almost completely absorptive in the 200 to 2000 Hz frequency range. A lead/plastic sheet (51x102 cm) was suspended in one corner of the blockhouse to reduce the possibility of exciting a low frequency acoustic mode of the blockhouse itself. The muffler-diffuser was designed to reduce the fan noise (particularly the blade frequency component) that may propagate upstream into the test section. The effectiveness of the muffler-diffuser in reducing this noise is good (see Hanson for a complete

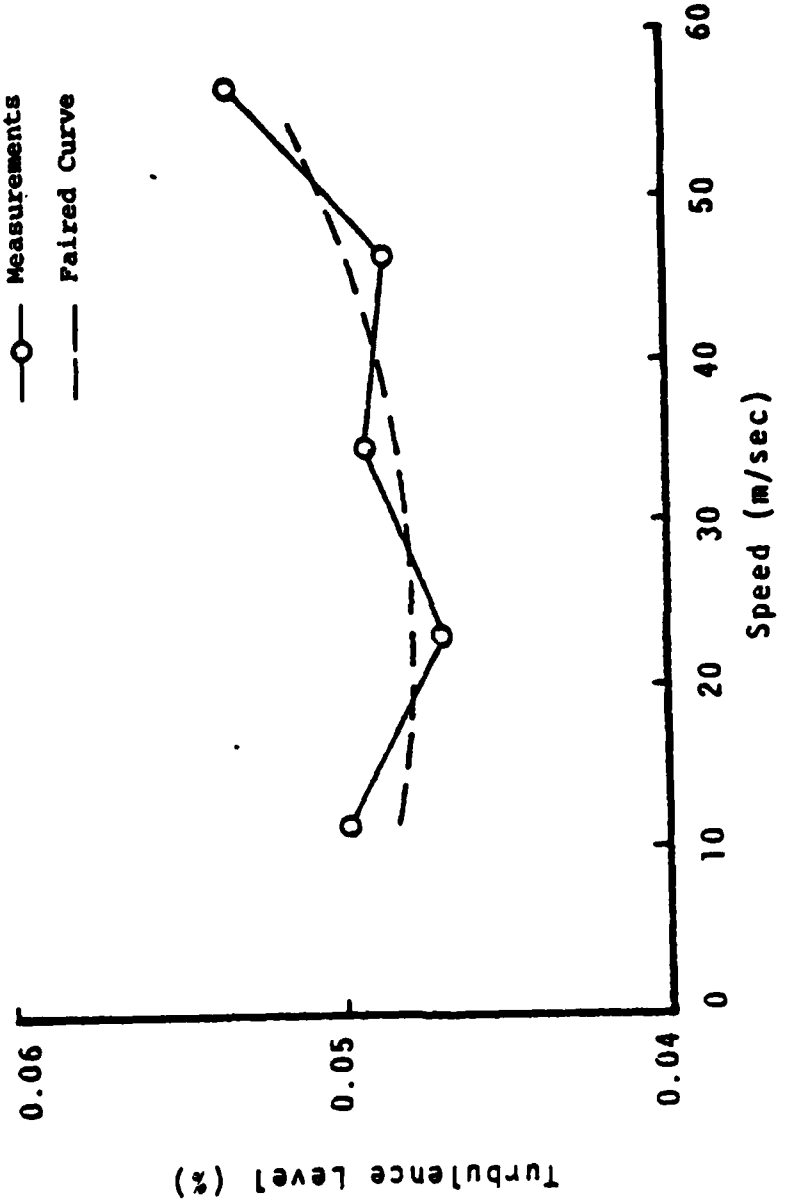

FIGURE 4.3 Free Stream Turbulence Level. Measured at Test Section Duct Centerline.

description). The possibility of noise from other sources entering the test section was reduced by the following: 1) the fan and its motor were mounted on a concrete inertia block to reduce the excitation of structural vibrations, 2) the fan housing was treated with vibration damping material and it was internally lined with acoustic foam, and 3) acoustic absorptive material was mounted on the laboratory walls in front of the tunnel intake and behind the fan.

The spectral densities of the background acoustic disturbances at the three test speeds are shown in Figure 4.4. These spectra were measured with a condenser microphone inside the blockhouse, just outside of the open-jet. One notes no peaks in the spectra above the 3 Hz Helmholtz resonance, except for a peak at 1480 Hz in the 18.5 m/s case, which will be described below. These acoustic background spectra have no peaks in the unstable TS wave range for a flat plate (as in the u' spectra of Figure 4.2) and also were not considered to have a significant influence on boundary layer transition inside the test section.

4.2 Test Section

The test section ducting was constructed to reduce the acoustic noise level in the flow. The test section walls

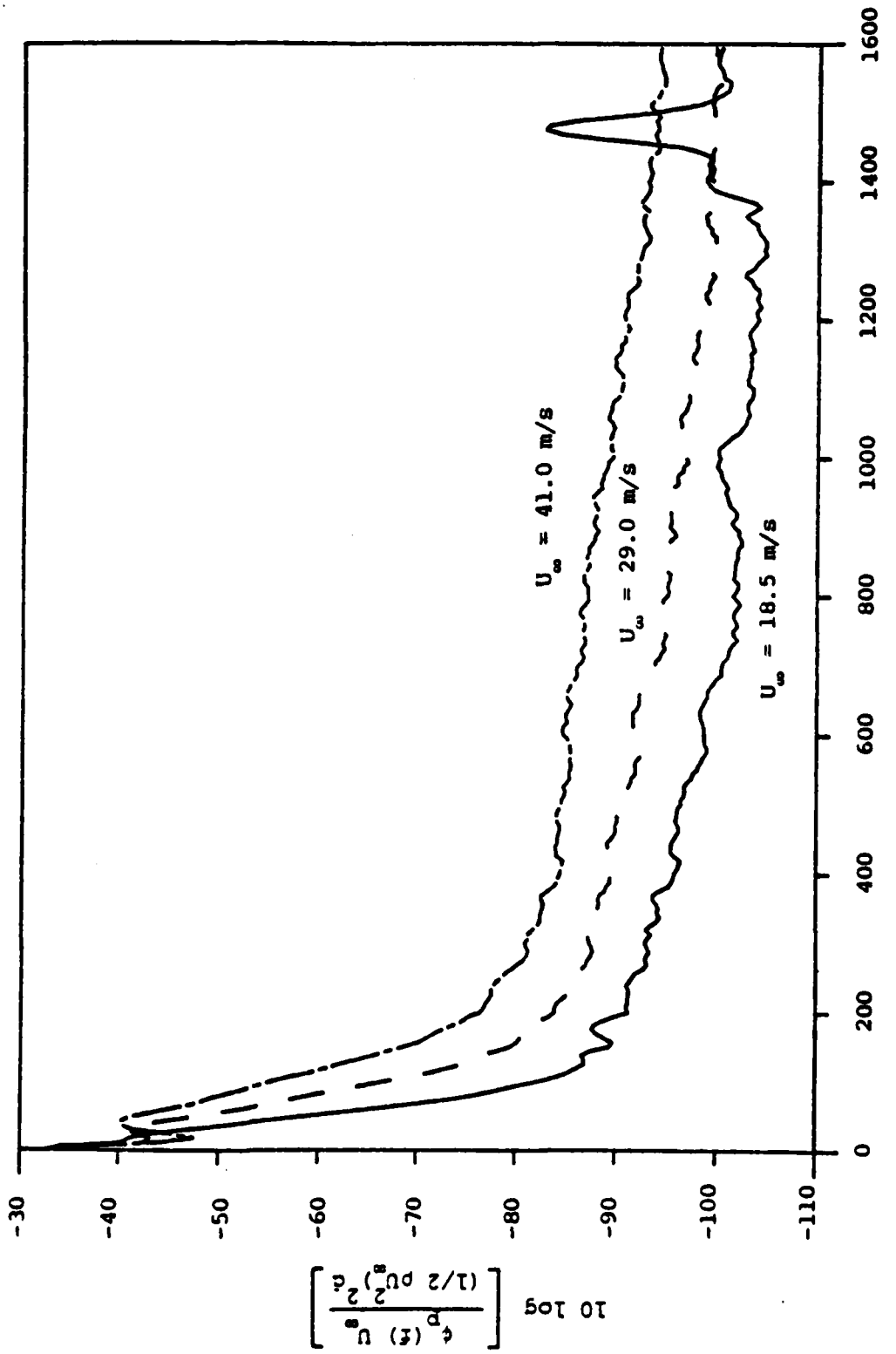

FIGURE 4.4 Background sound pressure spectral densities for three mean velocities, measured just outside of the open jet (d = 38 cm, the test section width).

were lined with 1.9 cm thick acoustic absorption material. The surface of this material was smooth, so that the flow was not disturbed. The material's absorption coefficient was small enough to allow the sound excitation wave (for the boundary layer excitation) to travel the length of the test section without a significant loss in amplitude. This absorption material also reduced the level of acoustic noise inside the test section, and the level of the acoustic cross modes in the duct that were excited by the sound wave. In the open-jet configuration the sound excitation was reflected at the open end of the test section duct, resulting in standing waves inside the duct. To reduce the amplitude of the reflected wave a fairing was built and attached to the open end of the test section. The fairing was constructed of wedge shaped panels, which were attached to the sides and the top of the test section. With the fairing attached, the test section did not terminate abruptly. Instead, it ended with a gradual effective area change (similar to an acoustic horn). Such an area change decreases the magnitude of the reflected wave. The fairing is sketched in Figure 4.5, and the standing wave pattern at 200 Hz, with U_∞=18.5 m/s, is shown in Figure 4.6. (The sound wave amplitude at a point 8.7 cm above the leading edge of the plate was 90 dB re 20μPa for the data of Figure 4.6.)

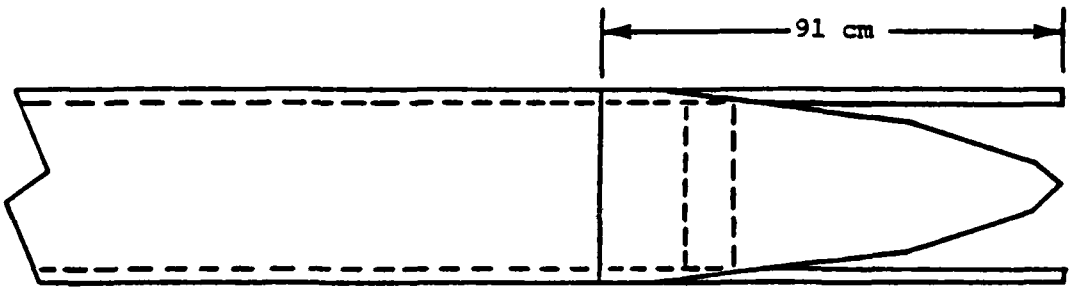

Top View

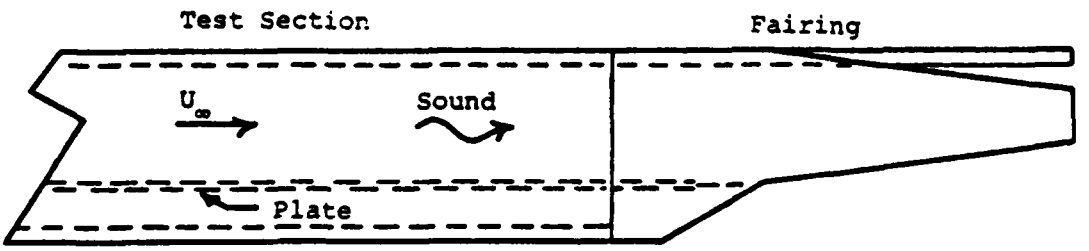

Side View

FIGURE 4.5 Test Section Fairing

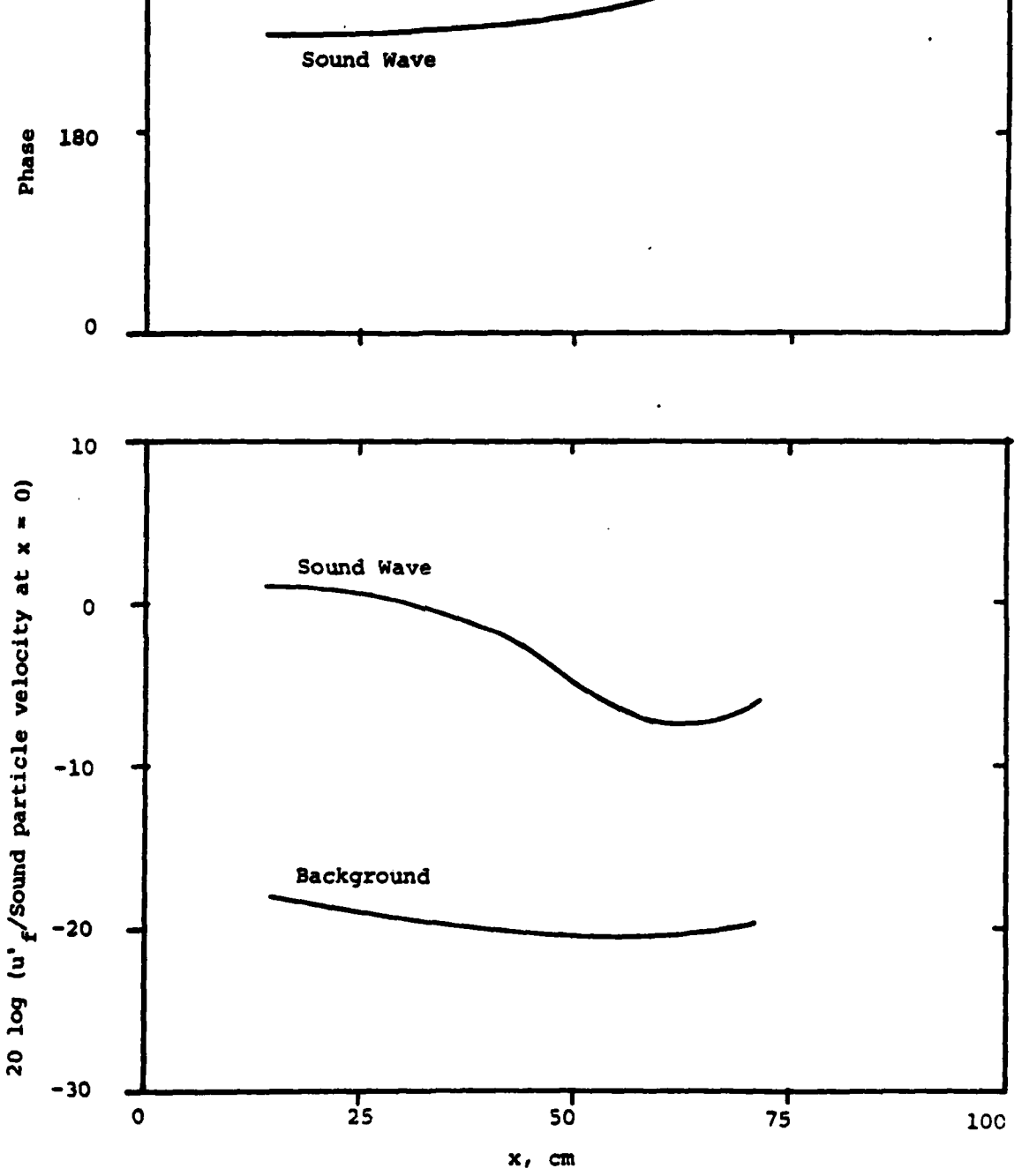

FIGURE 4.6 Sound particle velocity in the free stream at the excitation frequency (200 Hz) as a function of x. (Measured during the sound excitation tests. The phase is with respect to the speaker excitation signal.)

The inner sidewalls of the test section were flexible, and could be moved to adjust the cross sectional area of the duct at any point along its length. These walls were adjusted to minimize the static pressure gradient along the length of the test plate. Section 4.6 contains a description of the actual static pressure variations.

A remotely positioned traverse mechanism was mounted atop the test section. A remote controller was used because access to the blockhouse was difficult during the experimental work. The traverse mechanism had a symmetric airfoil that penetrated the top wall of the test section and carried a hot wire probe at its tip. The airfoil was tapered from a thickness of 4.7 mm at the root to 4.0 mm at the tip. At a flow speed of 18.5 m/s, vorticies were shed from different sections of the airfoil. The peaks in the 18.5 m/s spectra of Figures 4.2 and 4.4 are due to this shedding. The hot wire probe could be positioned in the x-y plane at z=0 (the center of the duct, see Figure 3.2). The resolution of the traverse mechanism was 0.025 mm in the y direction and 2.5 mm in the x direction. For the absolute calibration of the probe position the traverse was moved to its stops, where the distance between the probe and the plate was measured optically. The accuracy of this measurement was equal to the resolution of the traverse. A static pressure tube could be mounted into the traverse to

measure the static pressure variation over the length of the plate.

4.3 Test Plate

The velocity measurements that are presented in Chapter V were taken above the surface of a flat plate mounted horizontally in the test section. This plate was also used by Shapiro [7]. The plate spanned the entire 38 cm of the test section duct, and was 1.3 cm thick and 170 cm long. Figure 4.7 shows a cross-sectional view of the plate. The plate was rigidly fastened to the test section along its side edges and was 12.7 cm above the lower wall of the test section. During the plate vibration tests, the front 25 cm of the plate was disconnected from the sidewalls and was free to vibrate in the transverse direction. The plate was mounted below the centerline of the duct to avoid the secondary flow regions of higher free stream turbulence that appear in the flow (see Shapiro for a detailed descrption of these regions).

The leading edge of the plate was formed in a 6:1 semi-ellipse, both for its ease of machining and to prevent a severe pressure gradient which may have disturbed the normal development of the boundary layer. A thin formica splitter plate was installed into the trailing edge of the

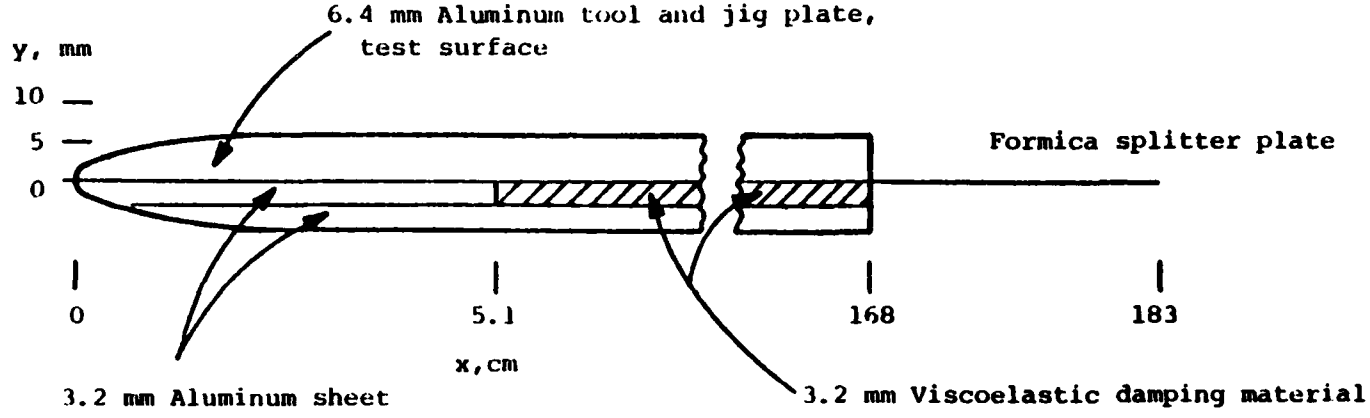

FIGURE 4.7 Test plate cross section.

plate, protruding 10.2 cm aft. This splitter separated the vortices that shed off the upper and lower surfaces, and thus prevented the excitation of plate vibration by coherent vortex shedding.

Unwanted vibration in the plate was kept to a minimum by constructing the plate as a sandwich of vibration damping material surrounded by aluminum. The upper section of the plate was a 6.4 mm thick aluminum tool and jig plate. The center section was a 3.2 mm thick sheet of damping material (E-A-R C-1002, from E-A-R Corp., Westwood, MA), followed by a 3.2 mm thick aluminum sheet. The sheets were bonded together with a high peel strength polyurethane adhesive. The forward 5.1 cm of the damping material was replaced by aluminum to simplify the machining of the leading edge. Shapiro's computations show that the overall damping of the plate ranged from 11% of critical damping at 2000 Hz and 25 C to 40% of critical at 500 Hz and 20 C. The actual vibration levels of the plate during the experiments are given in Section 4.6 below. The upper surface of the plate was polished to an rms surface roughness of 0.3 μm. This was somewhat smoother than the 0.6 μm rms plate used by Schubauer and Skramstad [1].

4.4 Hot Wire Probe

The velocity measurements were made with a miniature, u-component, boundary layer-type hot wire probe. (Thermo-Systems, Inc. model 1261-T1.5). This probe had a 4 μm diameter tungsten filament sensor that was 1.3 mm long. The probe is shown mounted in the traverse in Figure 4.8.

One of the problems of using this type of velocity sensor for oscillatory measurements was that the needles supporting the sensor were free to vibrate. At times, fluctuations within the boundary layer excited vibrations of the needles, which led to a serious degradation of the velocity signal as is shown in Figure 4.9. This figure is a spectrum of the hot wire signal measured at a point within the boundary layer. The spectrum shows a peak at the 3 Hz Helmholtz resonance along with a sharp peak at 700 Hz (A) and a broad peak at 1500 Hz (B). The peak at A is due to a mechanical resonance of the probe needles and the peak at B is due to boundary layer oscillations. The mechanical resonances of the probe were investigated by affixing the probe to a small shaker and placing the shaker in the flow with its axis in line with the streamwise direction, as shown in Figure 4.10. An accelerometer was attached to the shaker and the ratio of the hot wire signal to the velocity at the accelerometer (the probe base) is plotted versus frequency in Figure 4.11 (the phase between these signals is plotted in Figure 4.12). These figures show strong

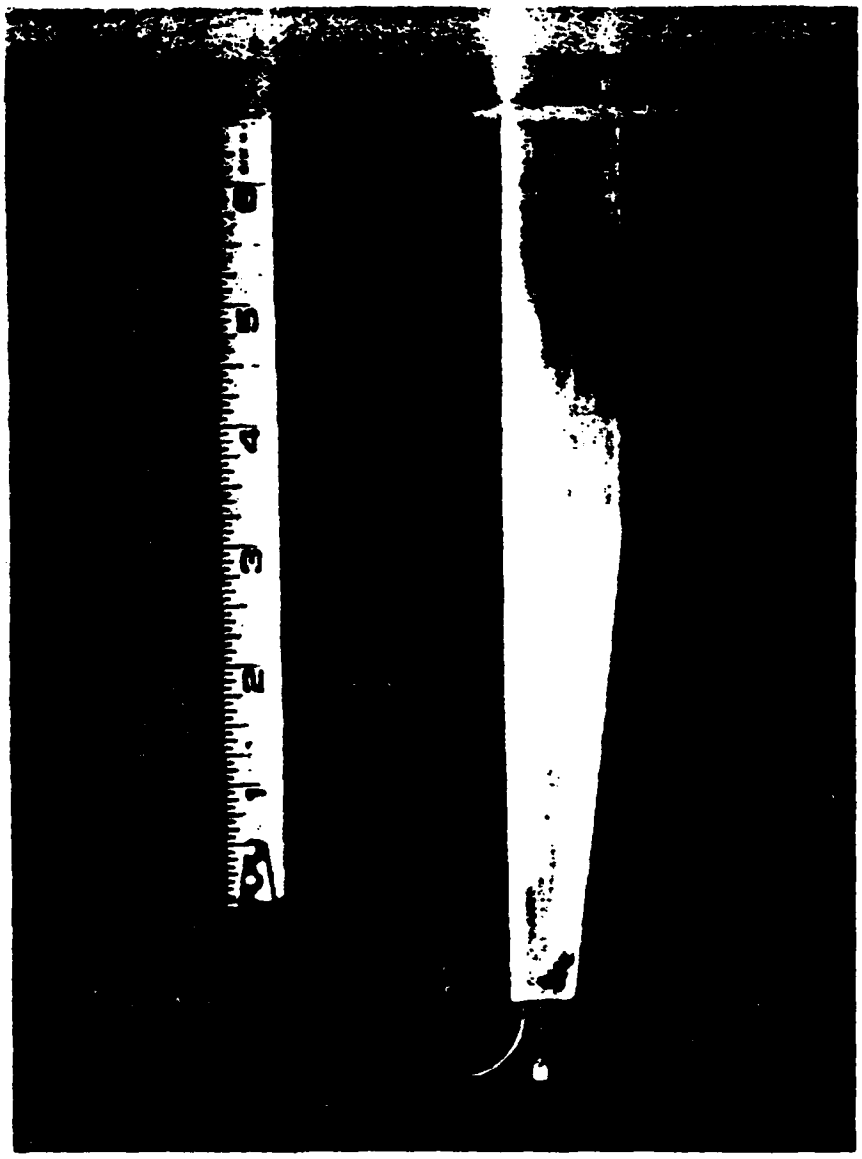

FIGURE 4.8 Traverse with hot wire probe installed (from Shapiro [7]).

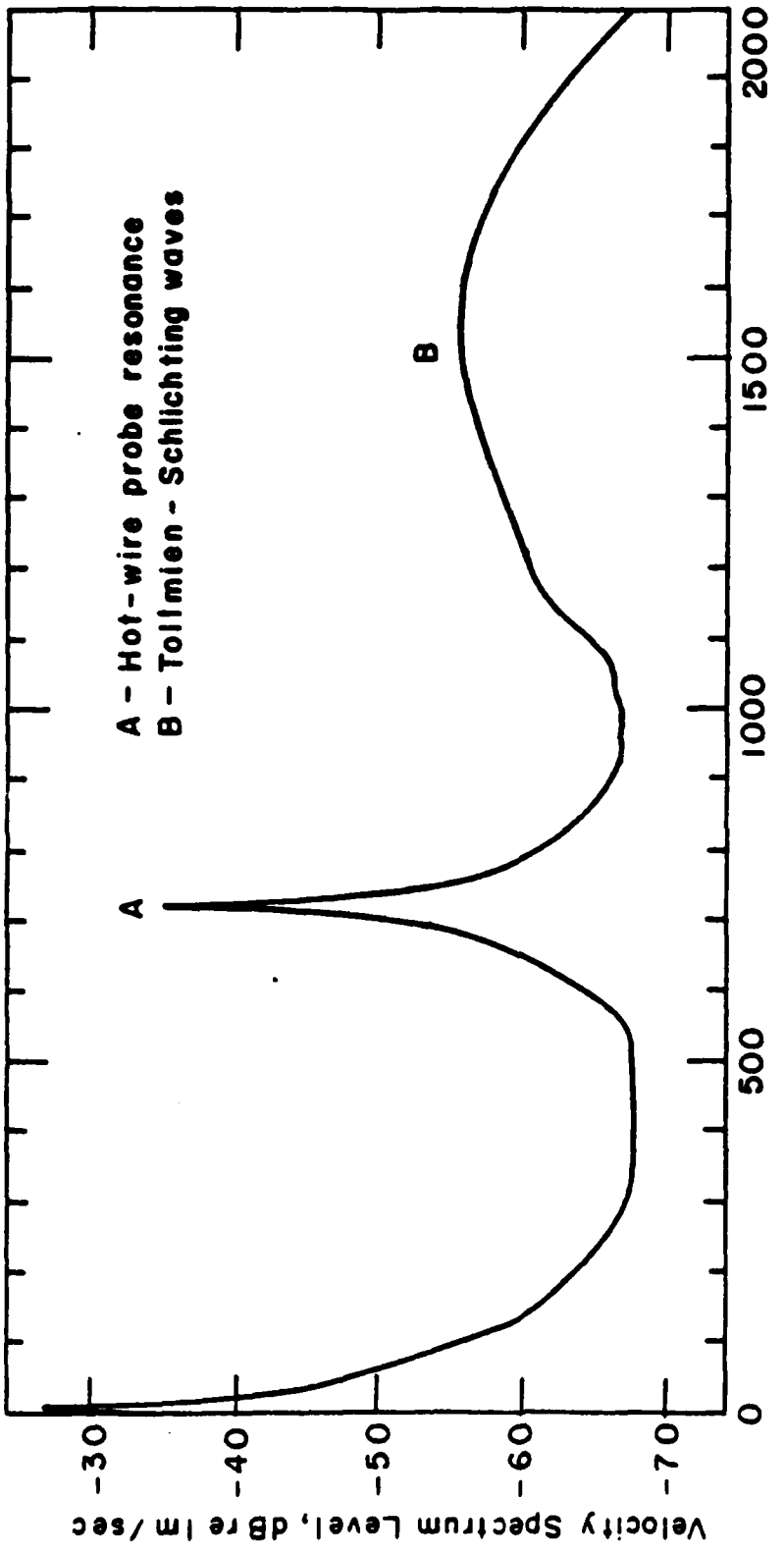

FIGURE 4.9 Spectrum of the hot wire signal in the boundary layer at x = 21 cm, y = 0.4 mm, and U_∞ = 41 m/s (from Shapiro [7]).

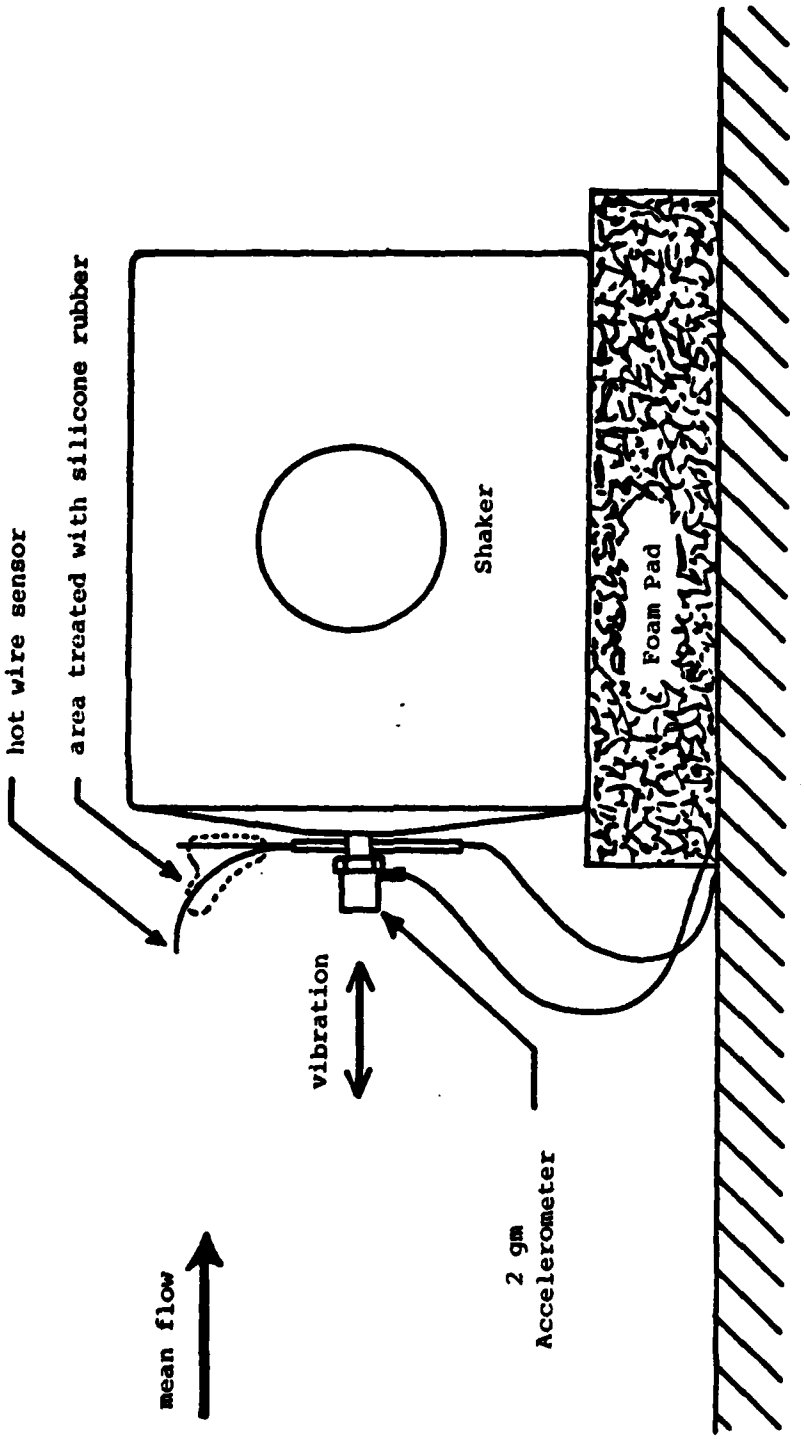

FIGURE 4.10 Set-up for hot wire vibration sensitivity test.

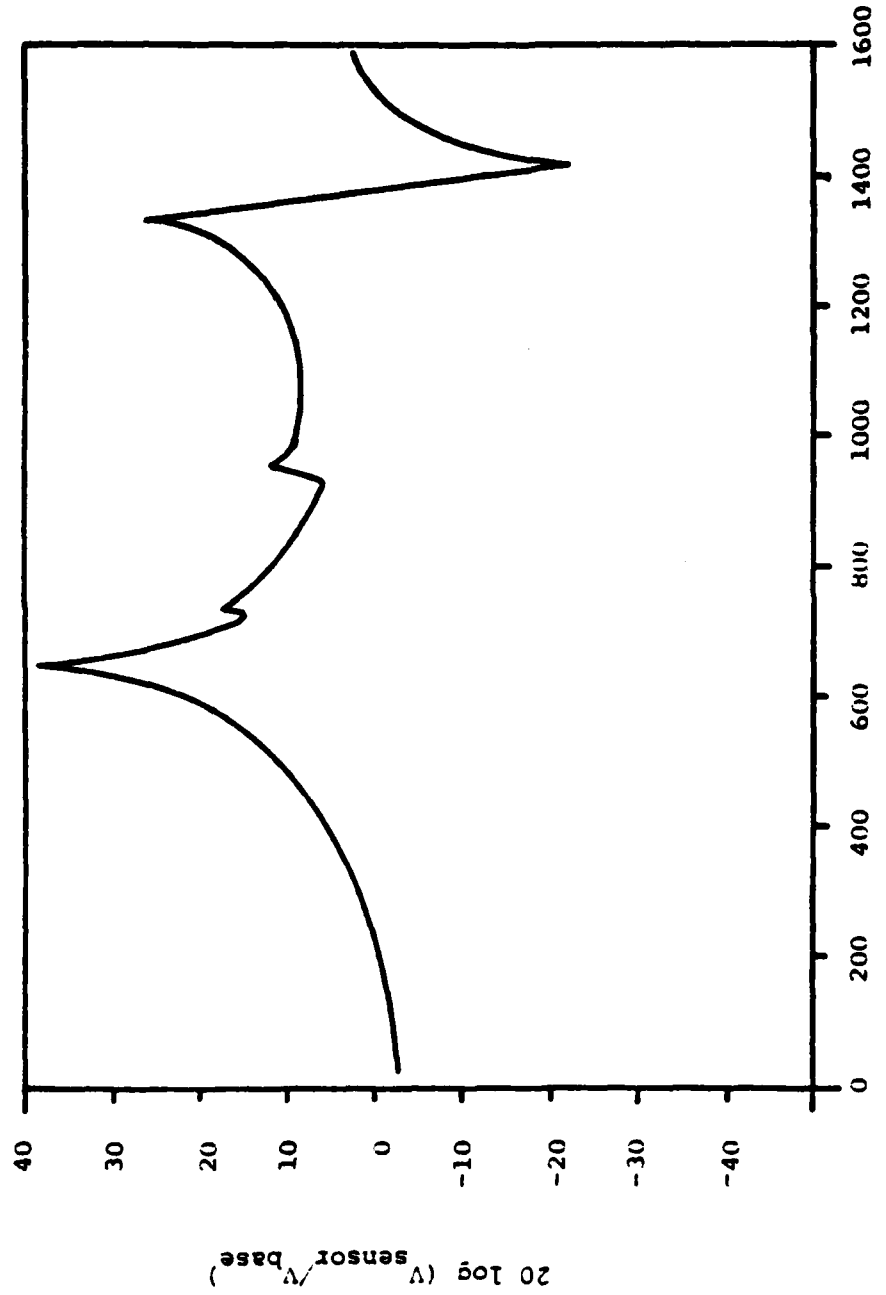

FIGURE 4.11 Hot wire probe vibration transfer function without damping treatment. (Velocity at the sensor divided by the velocity at the probe base as a function of frequency.)

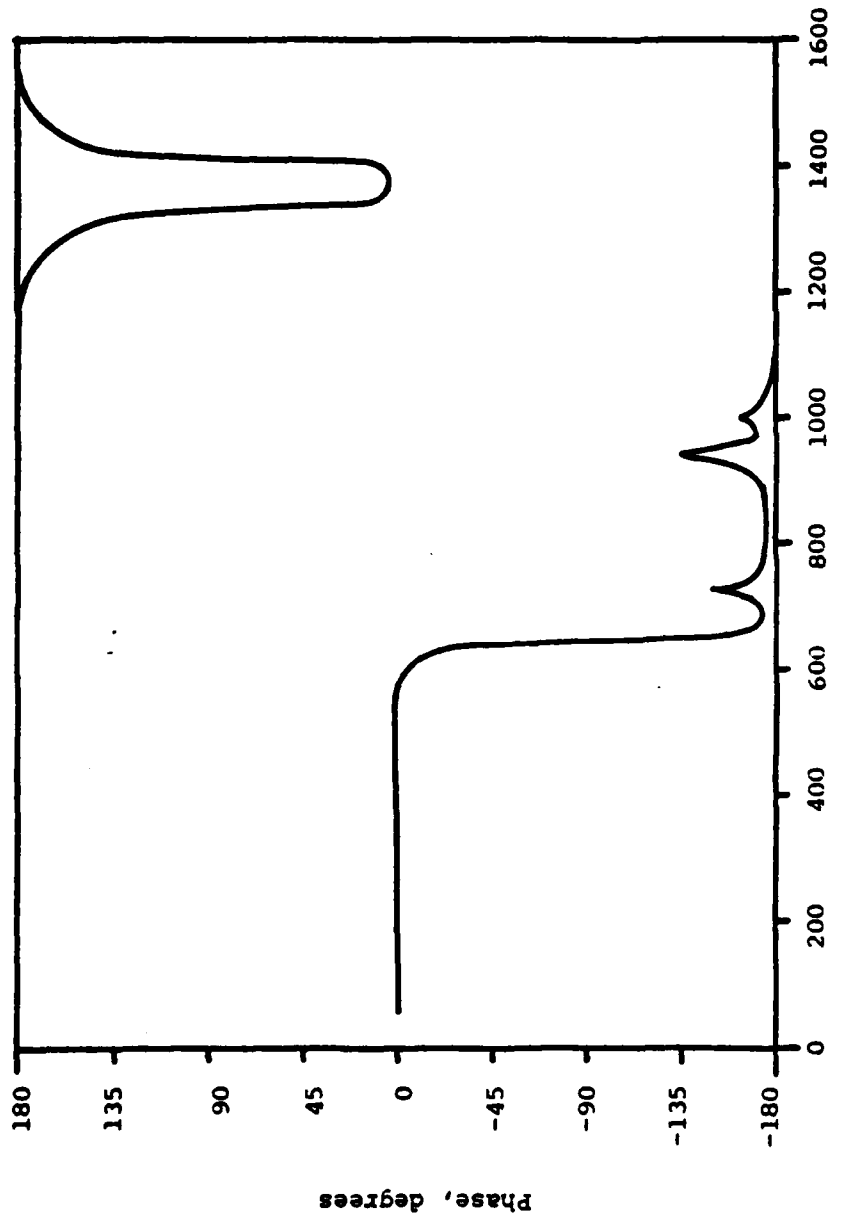

FIGURE 4.12 Phase of the hot wire probe vibration transfer function shown in Figure 4.11 (undamped).

resonances at approximately 650 and 1300 Hz. Even though most of the measurements were made at 200 Hz, the appearance of a strong oscillation at one of these resonances could seriously degrade the signal to noise ratio of the measurement. To avoid this problem, a patch of lightweight silicone rubber was added near the probe tip, as shown in Figure 4.10. The data of Figures 4.11 and 4.12 were retaken after the silicone was added and are plotted in Figures 4.13 and 4.14. Figures 4.13 and 4.14 show that a considerable amplitude reduction in the resonant peaks has occurred through the addition of the silicone rubber. The level of resonant mechanical peaks in the hot wire signal (such as peak A in Figure 4.9) were therefore significantly reduced, and the signal to noise ratio of the measurements was improved.

4.5 Instrumentation

A schematic of the instrumentation that was used during the sound excitation tests is shown in Figure 4.15. A DISA model 55D05 constant temperature anemometer was used to control the hot wire probe. This anemometer was powered by a DISA model 52A40 power supply. The anemometer output was linearized by a home built circuit. This circuit contained an adjustable exponentiating circuit with controls for gain and zero suppression. The frequency response of the

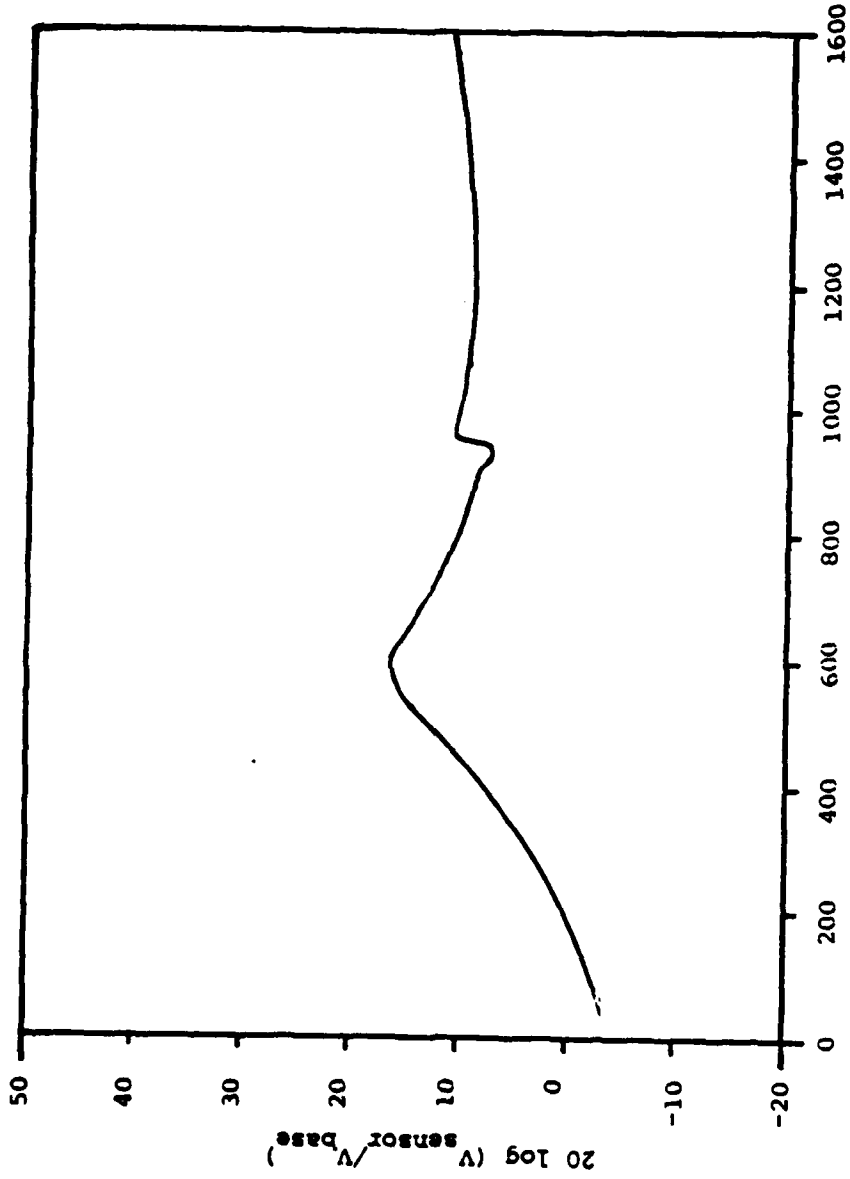

FIGURE 4.13 Hot wire probe vibration transfer function with damping treatment. (Velocity at the sensor divided by the velocity at the probe base as a function of frequency.)

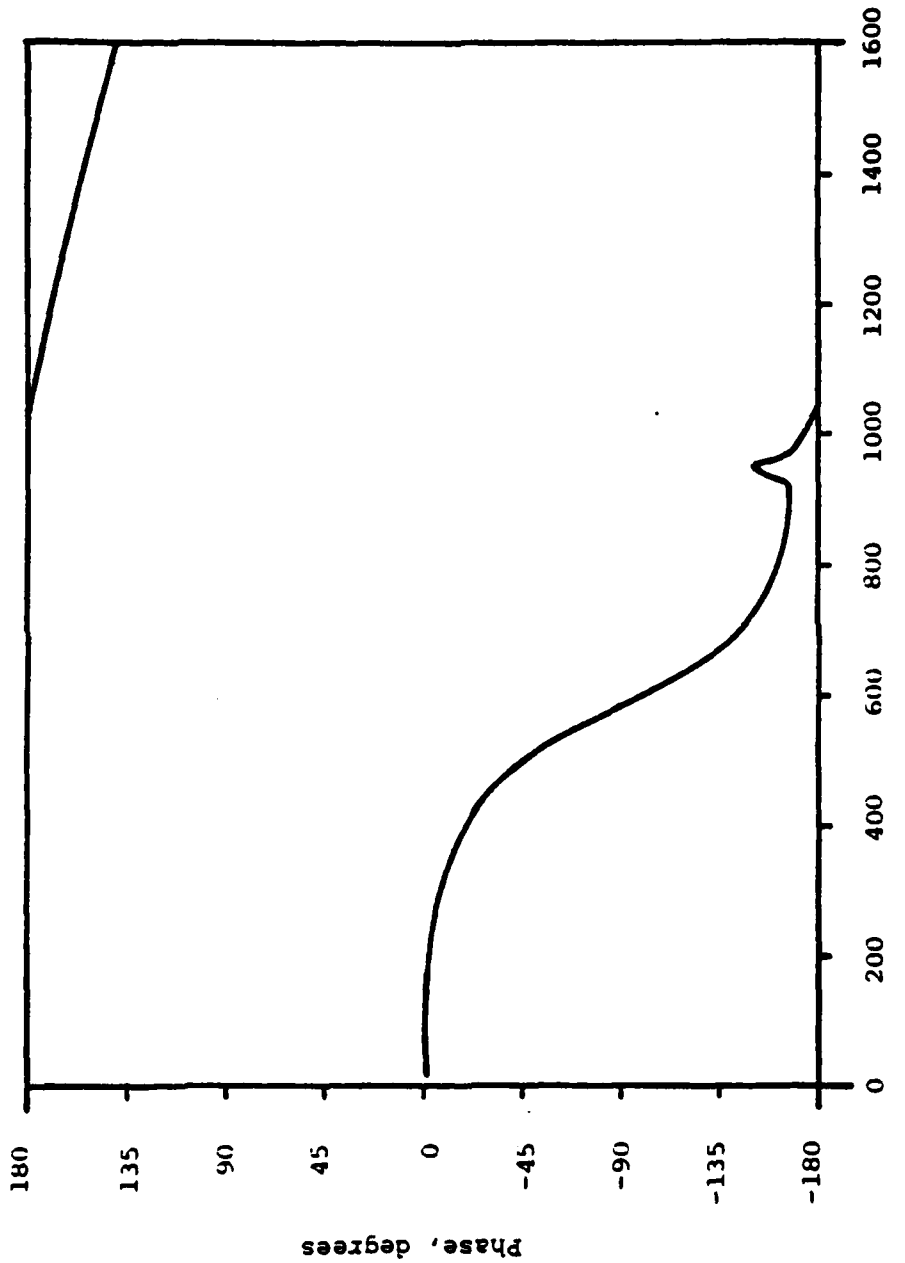

FIGURE 4.14 Phase of the hot wire probe vibration transfer function shown in Figure 4.13 (damped).

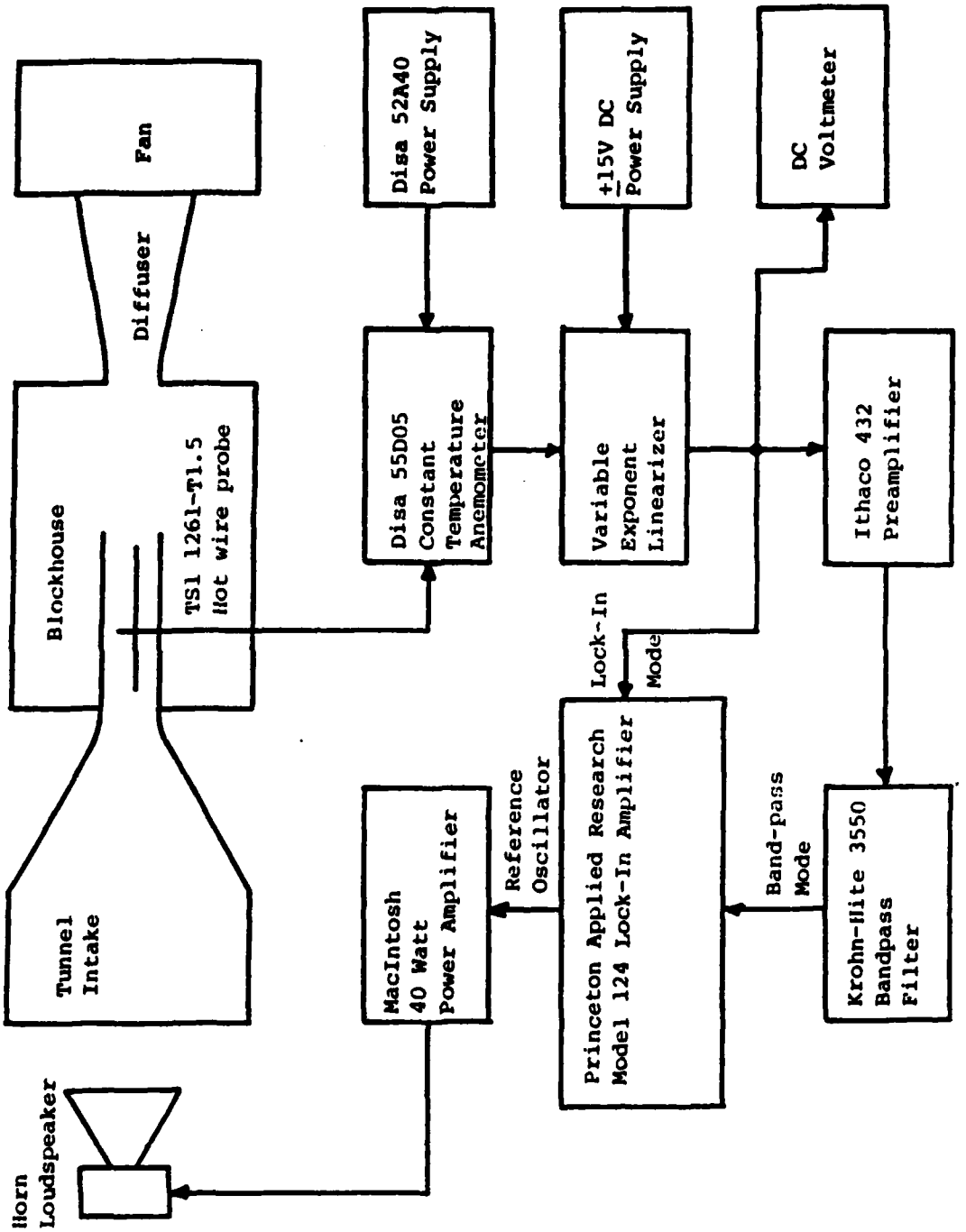

FIGURE 4.15 Schematic of the instrumentation used in the sound excitation tests.

anemometer-linearizer system was flat from 0 to 10 kHz. Figure 4.16 is a plot of the linearizer calibration, and Figure 4.17 is a plot of the mean boundary layer profile, measured at x=15.2 cm. Figure 4.16 shows that the maximum error in the linearization was approximately 5%. Figure 4.17 shows that the entire velocity measurement system was working well, since the measurements agree with the Blasius theory. The output of the linearizer was then approximately the instantaneous value of u (the x component of the velocity) near the hot wire sensor (assuming all fluctuations in u occured at frequencies less than 10 kHz). The spatial resolution of the hot wire was approximately 1.3 mm laterally (the length of the sensor). The longitudinal resolution of the wire is a complex function of the heat transfer characteristics of the wire and the air surrounding it. The longitudinal resolution of the wire is roughly the same order of magnitude as the wire diameter (4 μm). In fluid flow experiments, the lateral resolution and frequency response of the hot wire anemometer system usually become important long before the longitudinal resolution is a problem. Figure 4.17 also shows that, very near the plate (i.e. y<0.10 mm) the hot wire signal was influenced by the heat transfer to the plate, so that the data taken in this region were not accurate.

The central instrument in the equipment chain was a

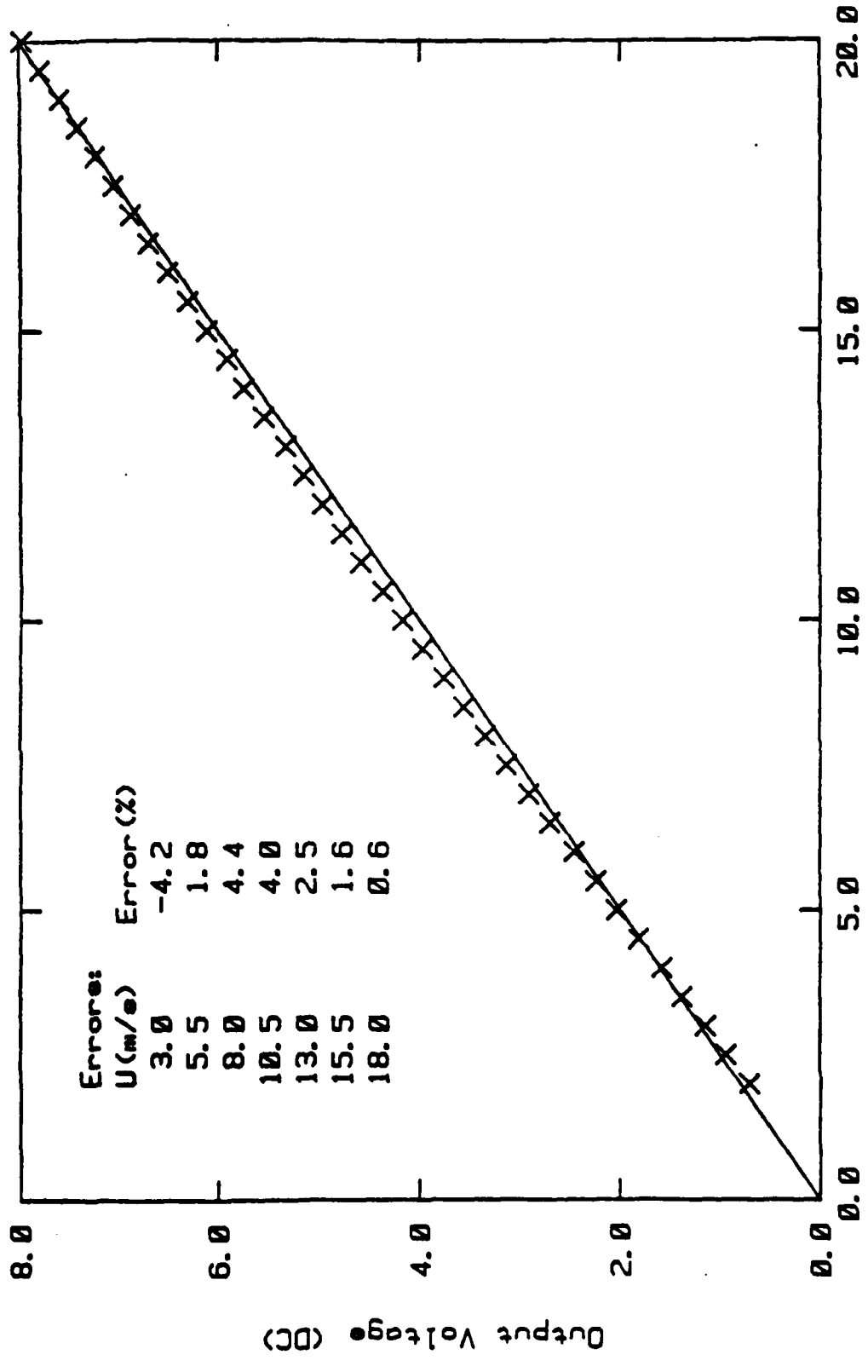

FIGURE 4.16 Linearizer output voltage as a function of the mean velocity at the hot wire.

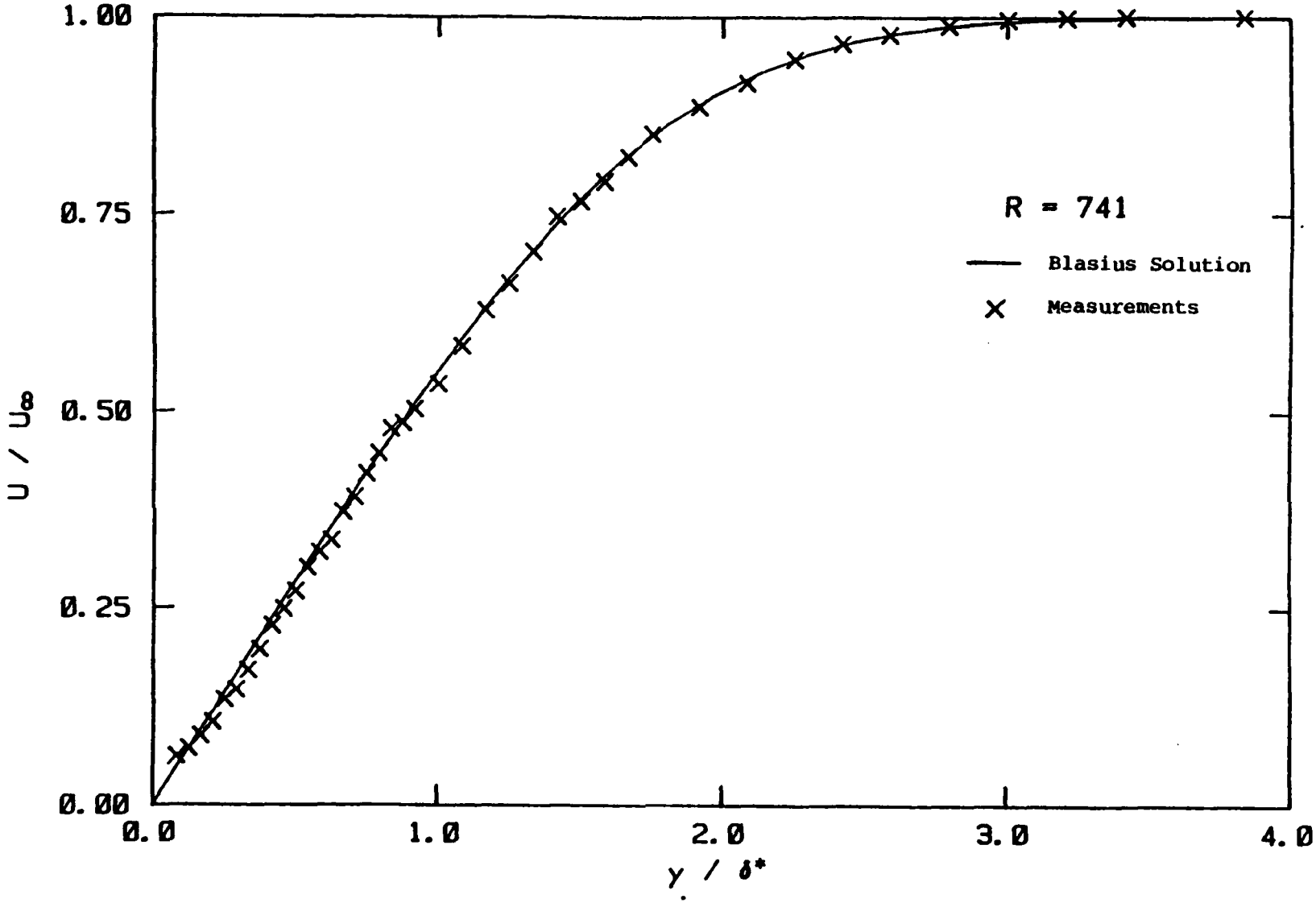

FIGURE 4.17 Mean velocity profile of the boundary layer at x = 15.2 cm, U_∞ = 18.5 m/s.

Princeton Applied Research model 124 lock-in amplifier. This amplifier was used to measure the behavior of the velocity fluctuations within the boundary layer. When an excitation was applied, the amplifier measured the magnitude and relative phase of that portion of the velocity signal which had a constant phase relation to the excitation signal (this will be called the lock-in mode). The lock-in amplifier also had a 4 Hz bandwidth filter and the level of the velocity signal inside this band was also measured. During these measurements, the velocity signal was preconditioned with an Ithaco model 432 preamplifier and a Krohn-Hite model 3550 bandpass filter and then fed into the 4 Hz filter. The center frequency of the 4 Hz filter was set at the excitation frequency, and the signal level inside this band was measured with the lock-in amplifier (this will be called the band-pass mode). When the excitation was applied, the velocity amplitude measured in the lock-in mode was compared to the level measured in the band-pass mode. In nearly all the measurements these two levels were equal, indicating that the locked-in signal dominated the 4 Hz bandwidth. In rare cases, the locked-in signal was very small and the band-pass measurement was larger than the locked-in measurement, due to other signals inside the passband. In other cases, the locked-in signal was larger than the band-passed signal, indicating that the lock-in amplifier was responding to the harmonics of the excitation

frequency. This was remedied by adding the 4 Hz filter to the lock-in mode circuit. During the unexcited tests only the band-pass mode was used, since no reference signal was present.

The sound excitation field was generated by a horn loudspeaker placed upstream of the tunnel intake. The pure tone signal from the reference oscillator of the lock-in amplifier was fed through a 40 watt McIntosh model MC40 audio power amplifier and used to drive the loudspeaker.

A schematic of the instrumentation used during the plate vibration tests is shown in Figure 4.18. This instrumentation is the same as that which was used in the sound excitation tests, except that the sound generation equipment was replaced by an electromechanical shaker and its power amplifier to generate the plate vibrations. The shaker was a 445N Bruel and Kjaer model 4801 with a model 4812 exciter head. The power amplifier was a Bruel and Kjaer model 2707. The shaker was connected to a 6.4 mm diameter drive rod which penetrated the bottom wall of the test section and was attached to the lower surface of the plate, 7.6 cm downstream of the leading edge. The influence of the drive rod on the pressure gradient above the plate was negligible. The shaker was also driven by the reference oscillator of the lock-in amplifier.

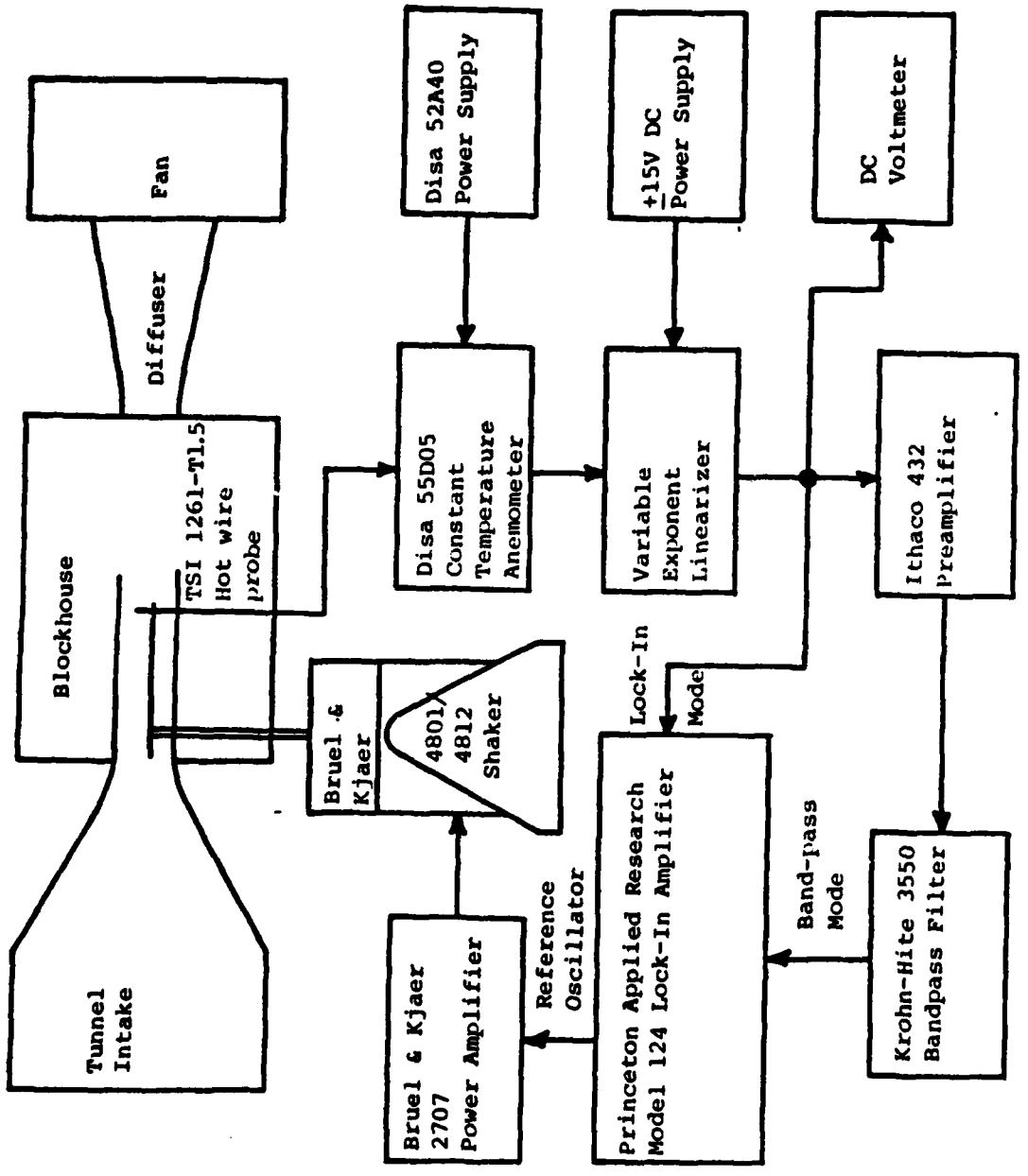

FIGURE 4.18 Schematic of the instrumentation used in the plate vibration tests.

The final type of excitation was provided by a vibrating ribbon, similar to the one used by Ross et al [21]. The ribbon was a 2.5 mm wide, 0.051 mm thick brass strip that was 30 5 cm long. This strip was heavy enough to prevent fluttering, yet thin enough that it did not disturb the flow so as to cause immediate transition The strip was stretched over the plate at x=20.4 cm. Two 0.38 mm diameter glass rods were placed under the strip at points where z=+/-10.2 cm, to hold the ribbon above the plate. This allowed the central 20.4 cm of the ribbon to vibrate freely in the vertical direction. The strip was held in contact to the plate, just outboard of the rods, with cellophane tape. The glue on the tape was not allowed to contact the ribbon so that constant tension in the ribbon could be maintained. The tension was applied with weights that were attached to each end of the ribbon and hung over pulleys. The pulleys were located outside of the test section. The tension was applied equally to both edges of the ribbon to prevent fluttering. The tension was adjusted until the first resonant frequency of the ribbon, f_0, fell in the range $3/2f<f_0<3f$, where f is the driving frequency. This relation was suggested by Ross. A drive rod protruded through one side of the test section and was attached to one end of the ribbon. The rod was driven with a 222N Ling model V50Mk1 electromechanical shaker which was suspended horizontally inside the blockhouse. The McIntosh power

amplifier was used to drive the shaker.

Some of the experimental tests involved studying the response of two simultaneously applied excitations. In these tests, there was a need for the independent control of both the amplitude and the phase of each excitation. This was accomplished in the following manner. The primary excitation was driven with the reference oscillator of the lock-in amplifier. The reference oscillator signal was also fed into an Ithaco model 432 preamplifier and then into a Krohn-Hite model 3550 bandpass filter. The output was then fed into the secondary excitation equipment. The bandpass filter shifted the phase of the oscillator signal and the preamp was used to correct for the filter's insertion loss. The phase shift was set by adjusting the low-pass and high-pass frequency controls on the filter. The amplitude of each excitation could be set independently by the power amplifiers.

Throughout the entire course of the experimental work several precautions were taken to ensure that the data were as accurate as possible. Each time a new sensor was soldered onto the hot wire probe the linearizer was adjusted and a new calibration (as shown in Figures 4.16 and 4.17) was done. The mean velocity level was measured with a 6.35 mm diameter pitot-static tube and a Betz micromanometer.

Before any testing was started the lock-in amplifier was fully calibrated.

At the start of each day of testing the excitation level was set, and the calibration of each instrument was checked. The levels for each excitation case were set in the following manner. During the sound excitation tests, a Bruel and Kjaer model 4133 1.27 cm condenser microphone, together with a model 2615 microphone preamplifier and a model 2607 measuring amplifier were used to measure the sound level in the test section. The three Bruel and Kjaer units were first calibrated with a model 4220 pistonphone. Then the microphone was placed into the test section (without flow) at a position 8.7 cm directly above the center of the plate's leading edge. The sound level was increased until it reached 90 dB re 20 μPa. The sound field could then be switched on and off as necessary. In the plate vibration test, a Bruel and Kjaer model 4332 30 gm accelerometer and a model 2628 charge amplifier were used to measure the acceleration of the shaker's table. The level of acceleration at the table was set to a predetermined level, corresponding to the required vibration level of the plate. The shaker could also be switched on and off as needed. The 30 gm accelerometer was calibrated with a General Radio model 1557-A vibration calibrator. During the ribbon excitation tests, a Bruel and Kjaer model 4344 2 gm

accelerometer and the charge amplifier were used to set the vibrartion level of the ribbon excitation shaker to a predetermined level. The ribbon excitation was left on continuously during each test period.

The calibration of the instrument chain was checked each day in the following manner. A voltage of known magnitude and phase was inserted into the lock-in amplifier to check its calibration in both the lock-in and band-pass modes. After adjusting the anemometer and linearizer, the linearity of the mean velocity signal was checked at five points within the velocity range to be used in that day's testing. If a day of testing lasted more than four hours, the anemometer and linearizer were readjusted and the linearity of the velocity signal was rechecked.

As was noted above, the measurments in the excited cases were made in both the lock-in and band-pass modes. An immediate comparison was made between these measurements to ensure that the lock-in amplifier was functioning correctly, and that the velocity signal was not contaminated with noise. At each point in the boundary layer, measurements for the excited and unexcited cases were done in rapid succession so that the error due to any slow change in the hot wire sensitivity was kept to a minimum. During each measurement, the averaging time of the lock-in amplifier was

adjusted (in the 10 to 100 sec range) until a steady reading was obtained

4.6 Experimental Conditions

The free stream turbulence and the acoustic noise levels in the flow field were discussed in Section 4.1, but the other conditions under which the experiments were conducted will be given here. Most of the experimental results of Chapter V were taken at an excitation frequency of 200 Hz and a free stream velocity of 18.5 m/s ($\beta=56\times10^{-6}$). Direct comparisons with the data of Shapiro at 1.0 kHz and 29.0 m/s ($\beta=112\times10^{-6}$) will also be made in Chapter V. Another experiment is discussed in which plate vibration was used to cancel a sound-excited TS wave. This experiment was conducted at an excitation frequency of 500 Hz and a free stream velocity of 29.0 m/s ($\beta=56\times10^{-6}$). The results measured at 200 Hz and 18.5 m/s will be compared to numerical calculations of the TS wave solution and to Shapiro's measurements at 500 Hz and 29.0 m/s and at 1.0 kHz and 41.0 m/s. All of the sound excitation results were measured with the sound pressure level at the leading edge of the plate equal to 90 dB re 20 μPa. The plate vibration tests were conducted with the transverse velocity of the leading edge approximately equal to the sound particle velocity near the leading edge in the sound excitation

tests.

The variations in static pressure over the length of the plate for the three test speeds are plotted in Figure 4.19. These variations show significant adverse gradients near the start of the unstable TS wave range for the 29.0 m/s and the 41.0 m/s flow speed cases. The unstable TS wave range that is indicated in Figure 4.19 was obtained from the numerical calculations of the spatial stability problem for a zero pressure gradient flow. The approximate Falkner-Skan parameter (β_{FS}) corresponding to the maximum pressure gradient is -0.03 for U_∞=29.0 m/s and -0.07 for U_∞=41.0 m/s. The position of the start of the unstable TS wave range for a Falkner-Skan flow with β_{FS}=-0.05 is also shown in Figure 4.19. The adverse presure gradient regions for U_∞=29.0 m/s and 41.0 m/s are very close to the start of this range of unstable TS waves. However, in the U_∞=18.5 m/s case, the pressure gradient is nearly zero at this point, and slightly favorable further downstream. U_∞=18.5 m/s was chosen for the present experiments because of these reasons. It should be noted that the values of the boundary layer Reynolds number, R, (recall $R=U_\infty \delta^*/\nu$) in this figure were computed assuming the flow was a Blasius boundary layer.

Figure 4.20 is a top view of the test plate showing the regions of the boundary layer that were contaminated by

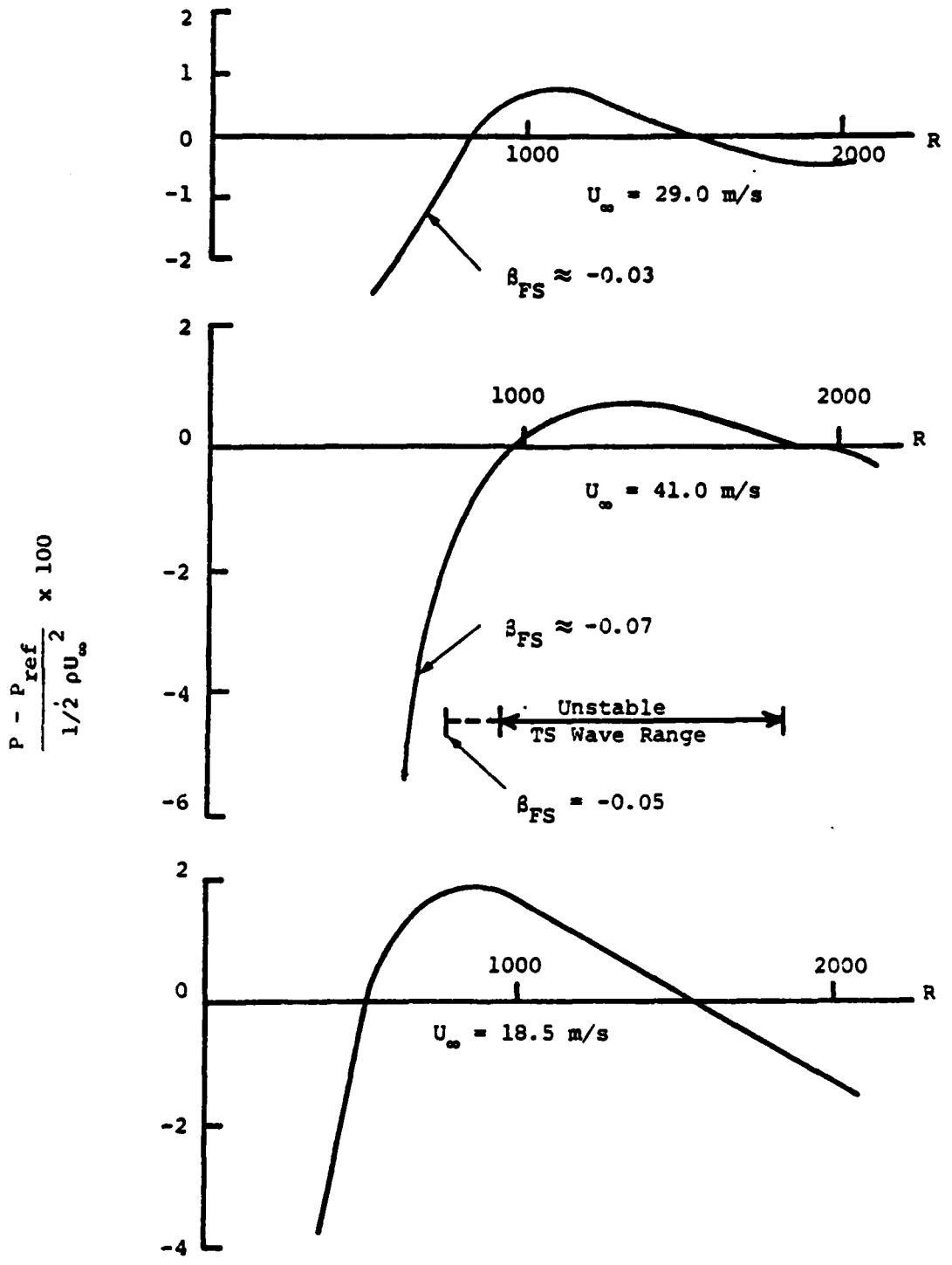

FIGURE 4.19 Static pressure variations along the test plate at three free stream velocities.

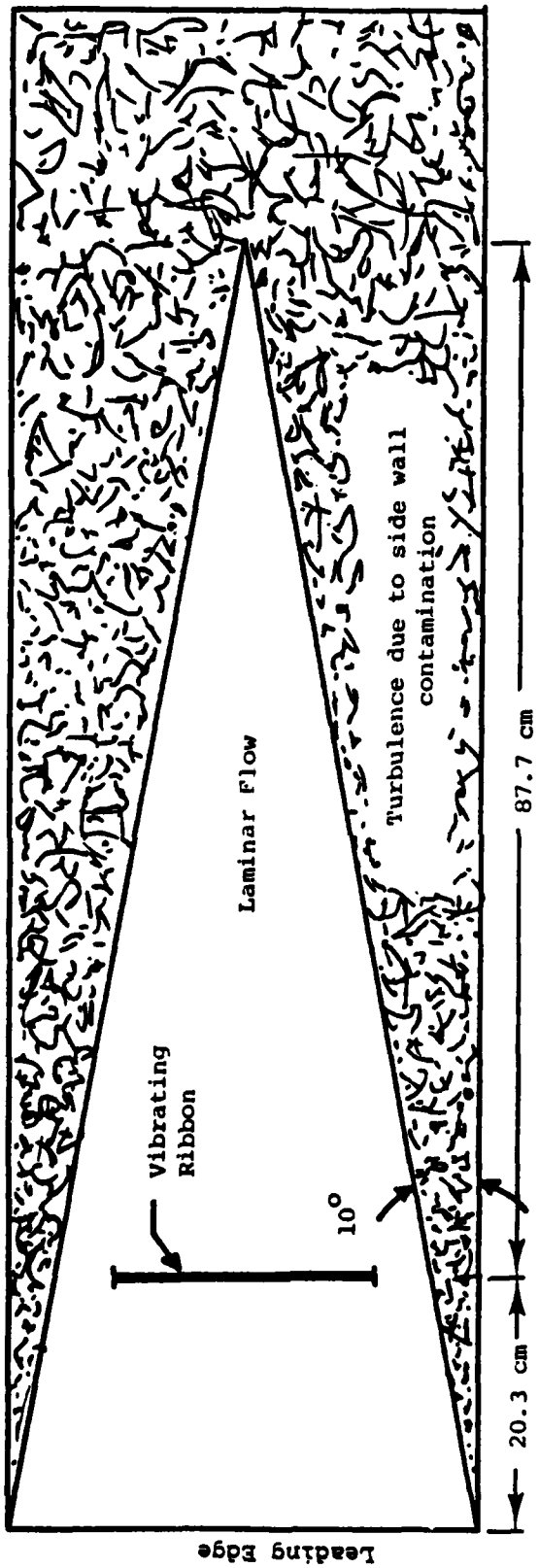

FIGURE 4.20 Top view of test plate showing side wall contamination and location of the vibrating ribbon.

turbulence from the sidewalls. This figure was obtained by coating the plate with a flow visualization film. To avoid the contaminated region, measurements were not made downstream of x=66.6 cm.

Figure 4.21 is a spectrum of the sound pressure level during sound excitation, measured at a position 8.7 cm above the leading edge of the plate. The flow velocity was zero during this measurement. This figure shows that the second harmonic is 40 dB below the signal at the excitation frequency. The spatial variations in the sound excitation level were discussed in Section 4.2, and are plotted in Figure 4.6.

Figure 4.22 shows a frequency spectrum of the transverse acceleration of the leading edge of the plate during the plate vibration test. The driving frequency is seen to be approximately 30 dB above its second harmonic. Peaks are also present in this figure at harmonics of 60 Hz. This is due to motion of the shaker table at harmonics of the line frequency. The rms plate vibration level as a function of x is shown in Figure 4.23 for the plate vibration tests, and in Figure 4.24 for the sound excitation tests. The data for these figures were taken at the center of the plate using the lock-in amplifier. Figure 4.24 shows that the plate vibration level was 40 dB below the sound

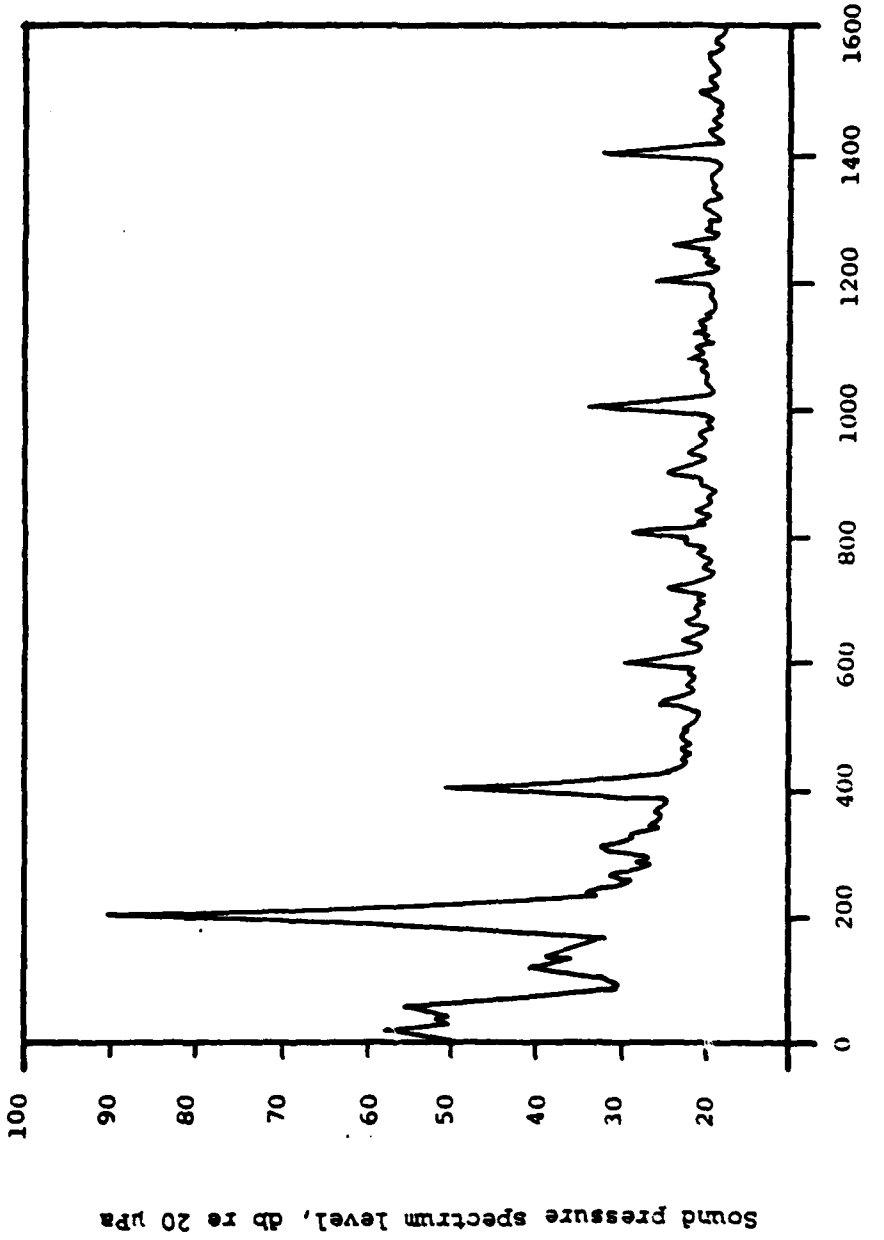

FIGURE 4.21 Sound pressure spectrum level during the sound excitation tests at x = 0 and y = 3.7 cm with U_∞ = 0.

AD-A132 843 THE RESPONSE OF A LAMINAR BOUNDARY LAYER TO SOUND AND WALL VIBRATION(U) MASSACHUSETTS INST OF TECH CAMBRIDGE ACOUSTICS AND VIBRATION L... C J GEDNEY MAY 83 2/2

UNCLASSIFIED A/V-83560-3 N00014-76-C-0396 F/G 20/4 NL

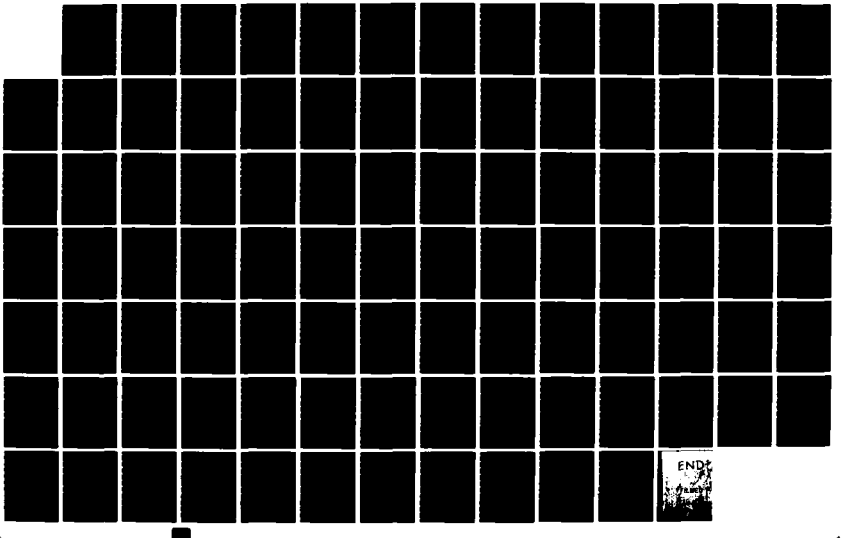

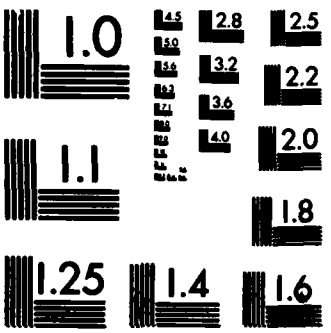

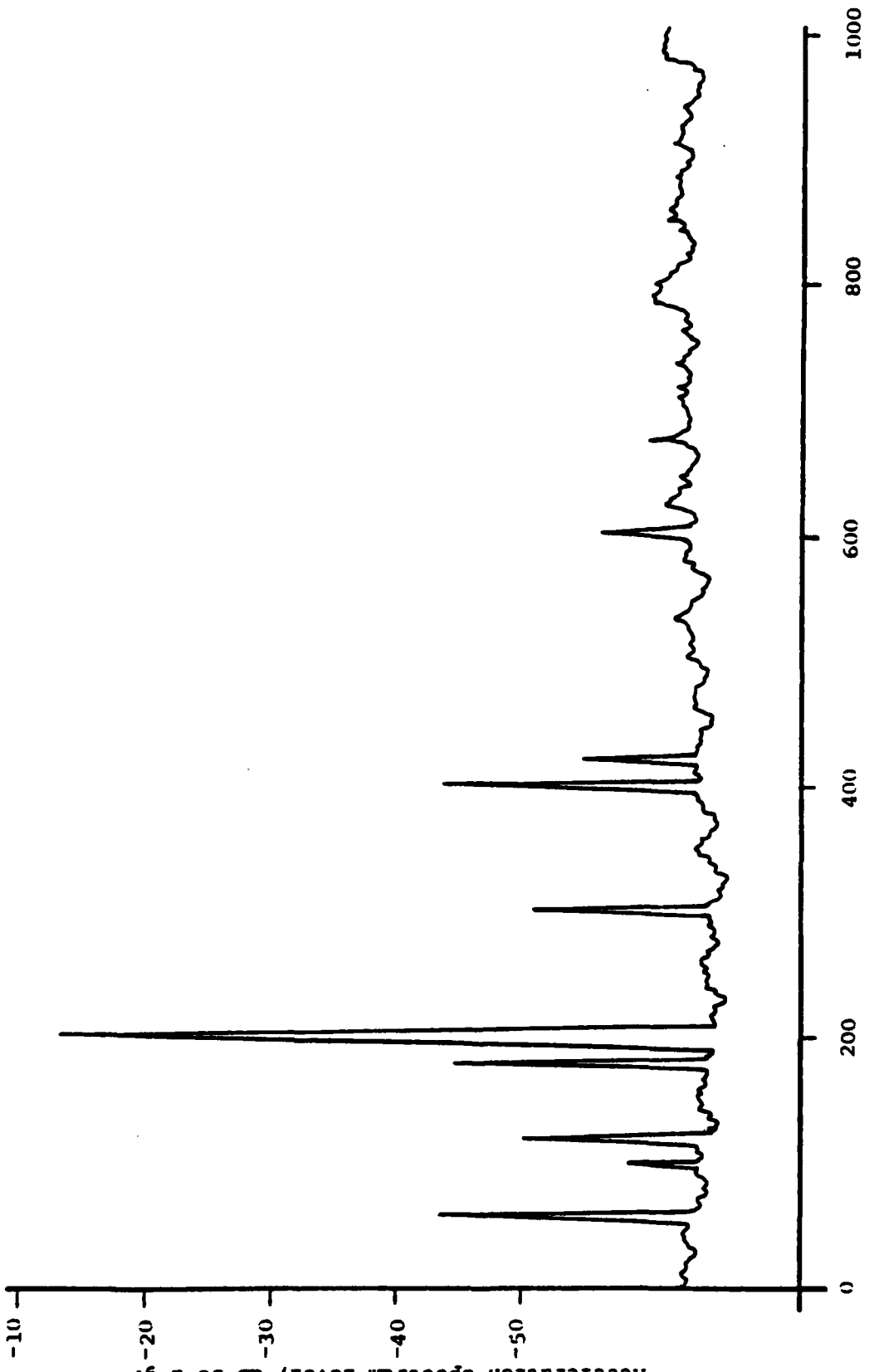

FIGURE 4.22 Plate acceleration spectrum level at x = 5.1 cm with U_∞ = 18.5 m/s during the plate vibration tests.

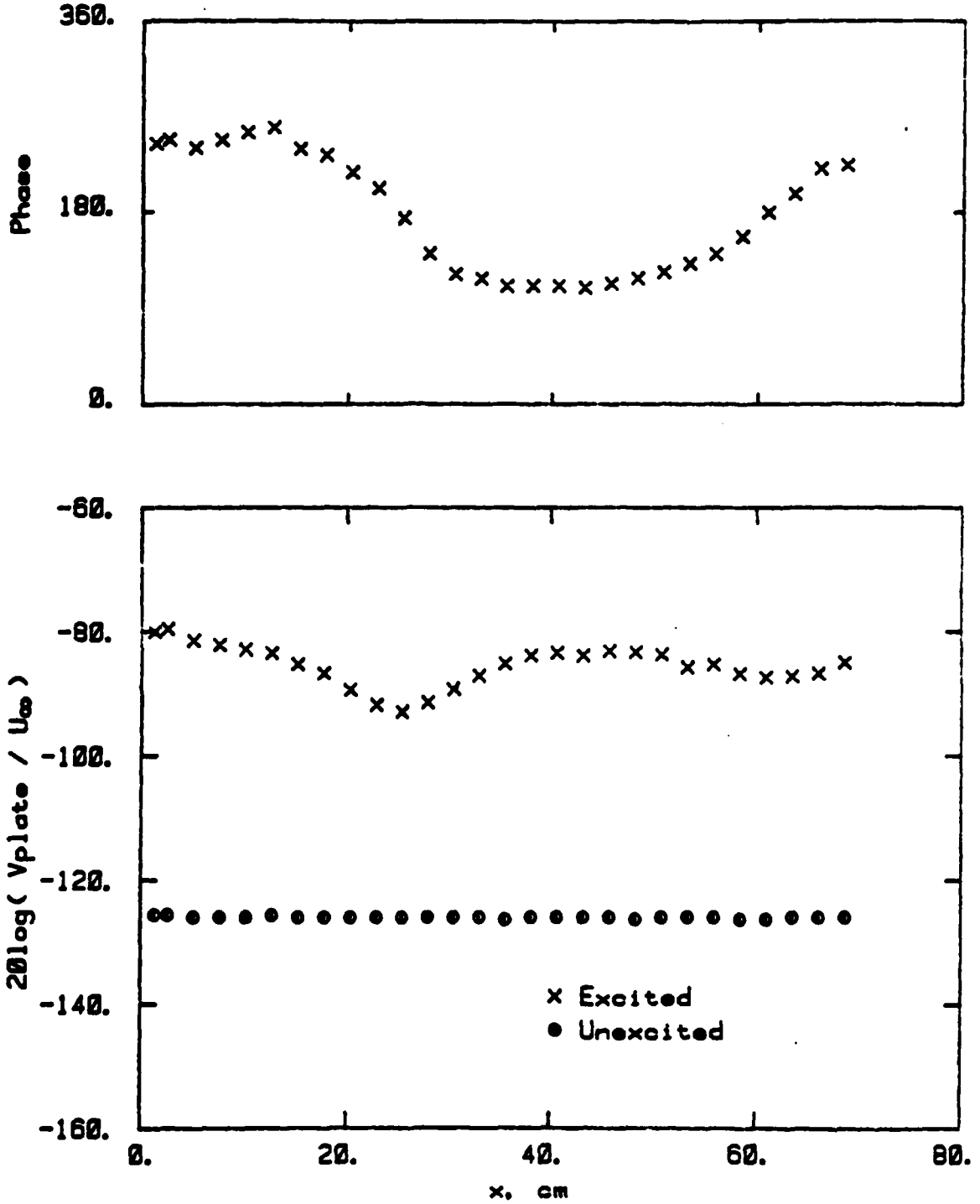

FIGURE 4.23 Plate vibration level at the excitation frequency (200 Hz) as a function of x, during the plate vibration tests.

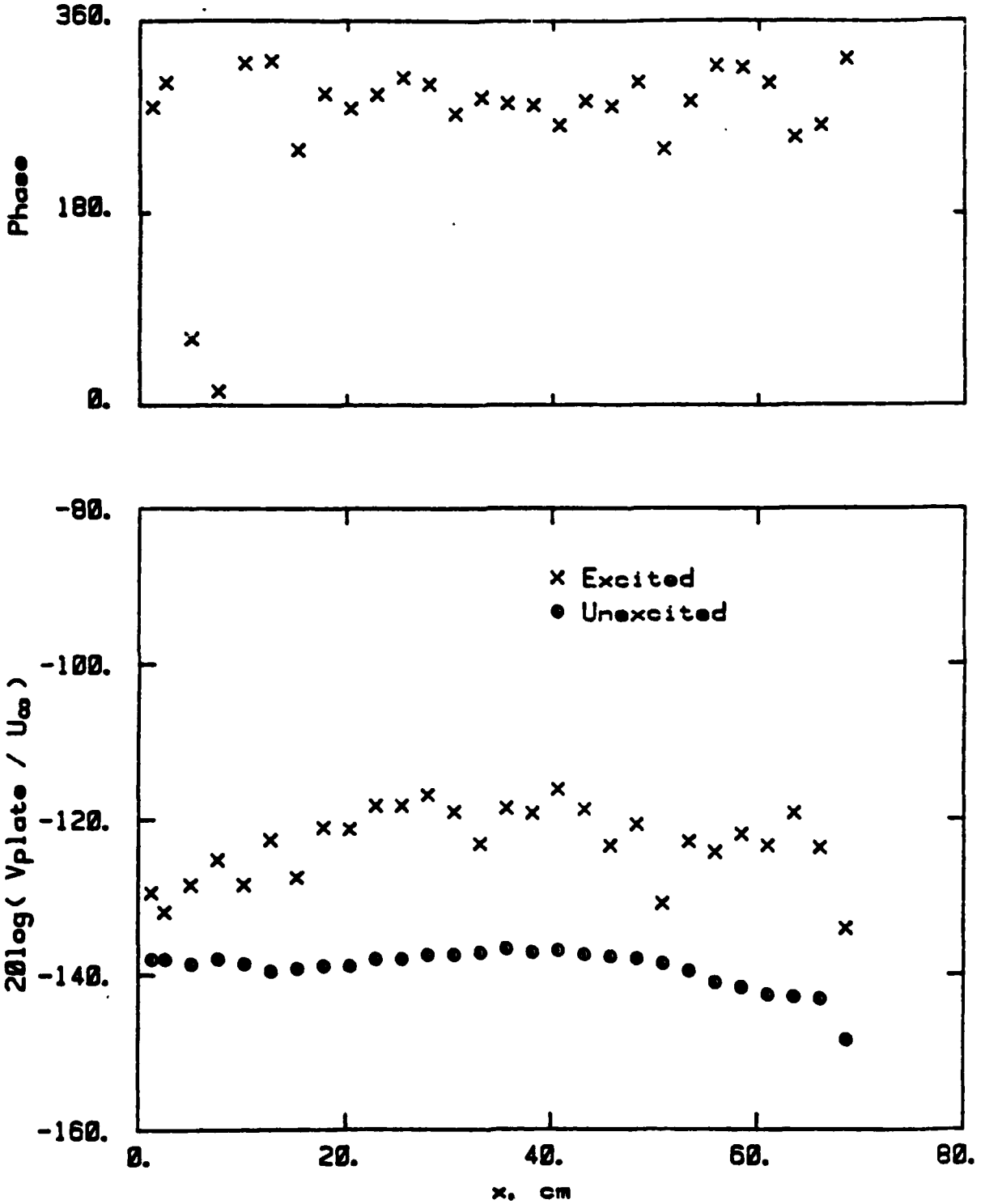

FIGURE 4.24 Plate vibration level at the excitation frequency (200 Hz) as a function of x, during the sound excitation tests.

particle velocity at the plate's leading edge during the sound excitation tests.

In the plate vibration tests, the motion of the plate produced a velocity oscillation in the stream. The streamwise component of this oscillation (measured in the locked in mode) is plotted as a function of x in Figure 4.25. The sound pressure level at a position 2.5 cm above the plate's leading edge was 78 dB re 20 μPa (measued with no mean flow).

During the ribbon excitation tests, the ribbon generated a small amount of sound and plate vibration. At the drive frequency, the sound pressure level (also measured without flow) 2.5 cm above the ribbon was only 50 dB re 20 μPa. The transverse velocity of the leading edge of the plate measured in the lock-in mode, with flow, was 48 dB below the level used in the plate vibration tests.

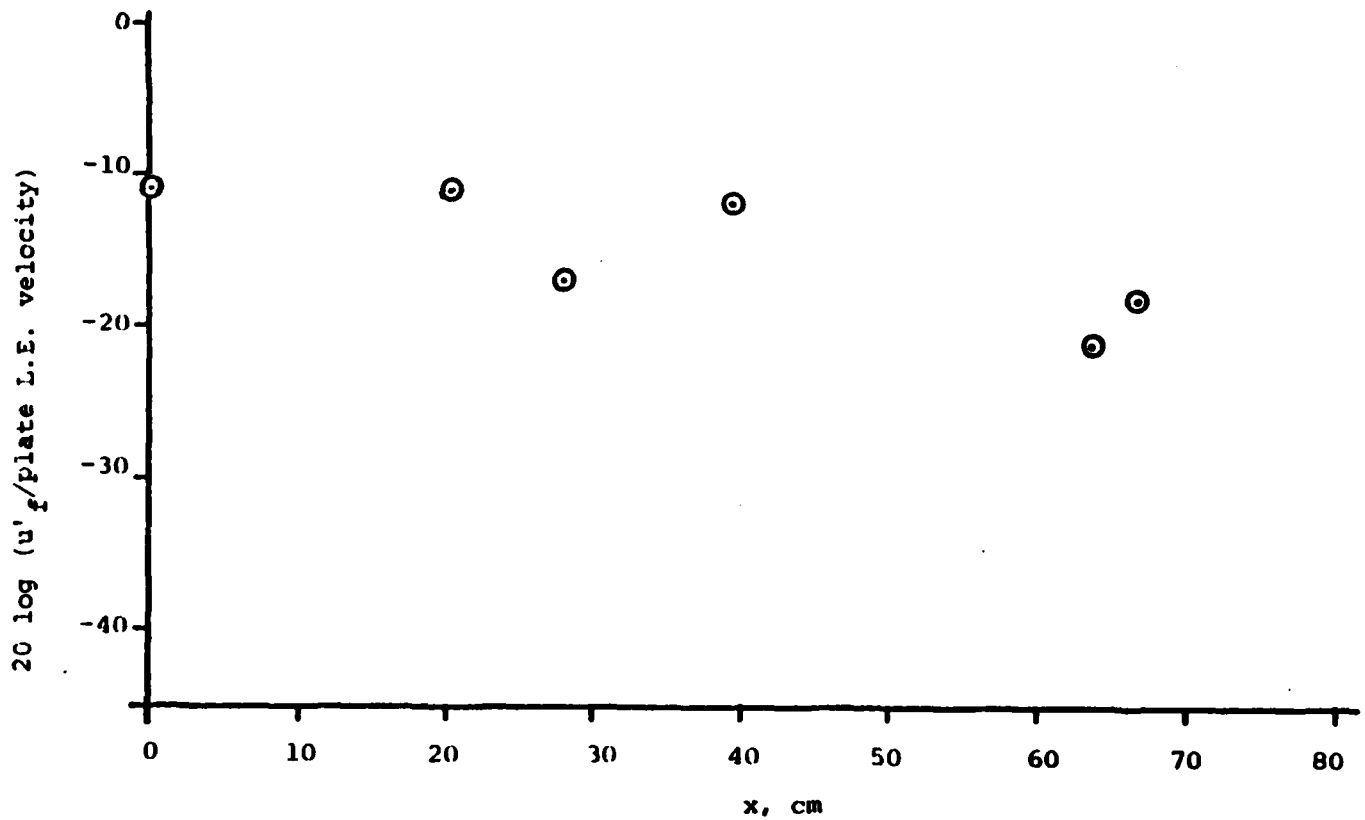

FIGURE 4.25 Free stream velocity fluctuations at the excitation frequency (200 Hz) as a function of x during the plate vibration tests (y = 1.27 cm, U_∞ = 18.5 m/s).

V. EXPERIMENTAL RESULTS

5.1 Comparisons at $\beta=112\times10^{-6}$

The first set of experiments were conducted at conditions identical to some of Shapiro's measurements. This provided a good check of the repeatibility of the experimental procedures and test conditions. These tests were conducted with a sound excitation frequency of 1.0 kHz and a free stream velocity of 29.0 m/s. The results are compared to Shapiro's results for both the excited and unecxited cases in Figure 5.1. This figure presents $\ln(A(x)/A_0)$ as a function of the boundary layer Reynolds number R and it shows the growth and decay of the boundary layer oscillations. A(x) is defined as the maximum amplitude of the oscillation at a given x, and A_0 is the value of A(x) at a reference position, x_0. x_0 is normally chosen to be the point at which the oscillations first begin to grow (i.e. the first point of the neutral stability curve). The values of R in Figure 5.1 were computed assuming that a Blasius boundary layer existed on the plate (that is, assuming the flow had no pressure gradients and the plate was flat to its leading edge). The region of unstable TS waves for the zero pressure gradient case is also shown in Figure 5.1. x_0 in this figure was chosen to be 2.5 cm (the first data point) since there the

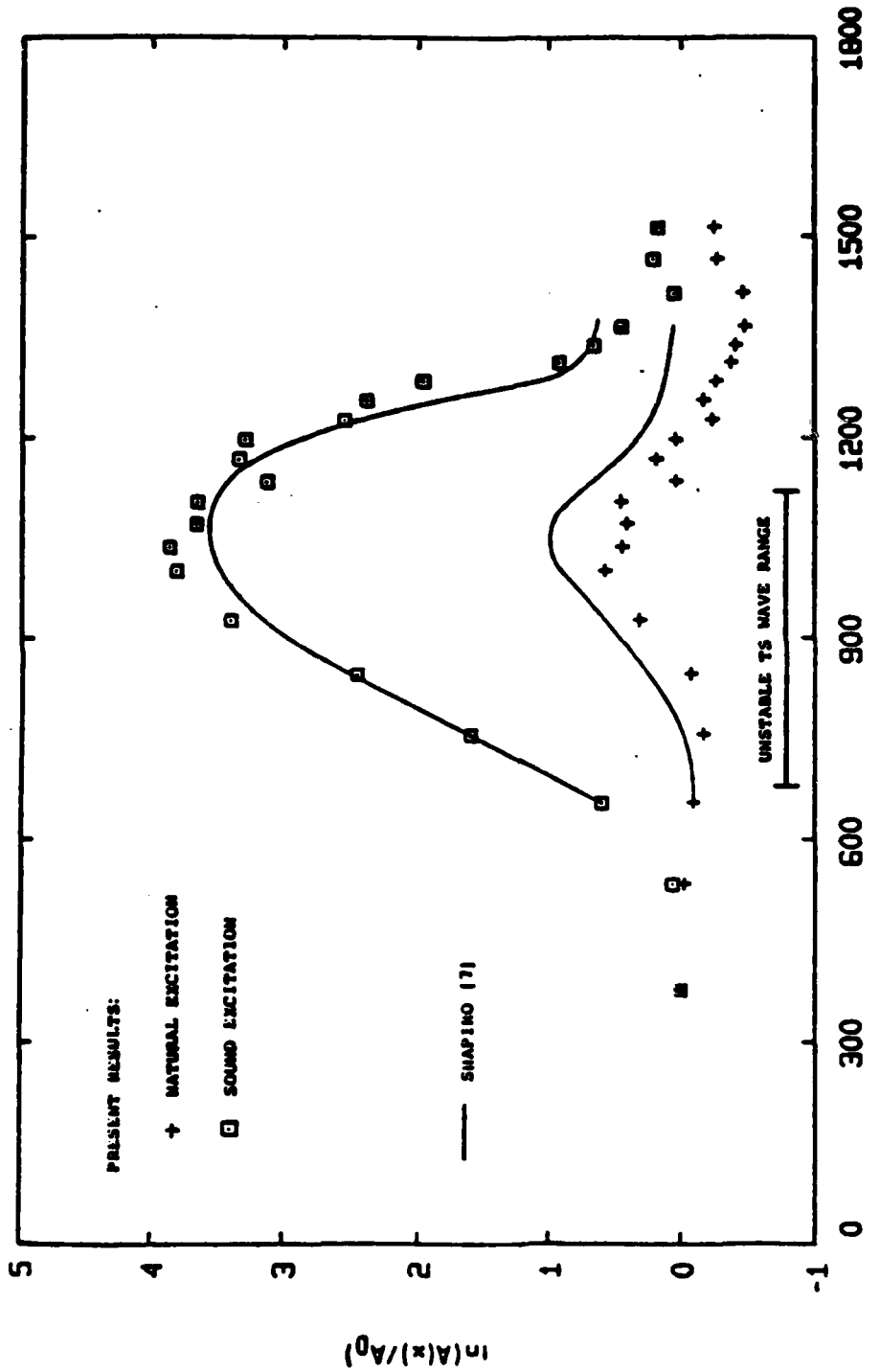

FIGURE 5.1 Boundary layer disturbance amplitudes (at $\beta = 112 \times 10^{-6}$) as functions of the Reynolds number (U_∞ = 29.0 m/s and f = 1000 Hz).

oscillations immediately began to grow. x_0 for Shapiro's data was adjusted until his results matched the present results at R=656 (the third data point). The oscillations of Figure 5.1 began to grow before the unstable TS wave range was reached because of the adverse pressure gradient (see Figure 4.19).

The close agreement with the data of Shapiro was encouraging, and further tests were then conducted. It should be noted that the data in Figure 5.1 were obtained with the same instrumentation as Shapiro, and the same test plate and wind tunnel were used. Later experiments were conducted using the instrumentation that was described in Chapter IV.

5.2 Natural Excitation of the Boundary Layer

The baseline for comparison of the experimental results in this work and in Shapiro's is the natural excitation (or unexcited) case. The increase in magnitude of the boundary layer oscillations due to the excitation is determined by comparing the excited and unexcited cases. As Shapiro points out, the growth of the oscillations is slower in the unexcited case than it is in the excited case or for the TS wave calculations. This is because in the natural excitation case the, excitation was mainly free stream

turbulence, and the propagation direction of the oscillations was therefore random. The average growth of these oscillations is less than the maximum (the calculated TS wave growth). In the sound excitation or plate vibration cases, a two-dimensional disturbance is produced at the leading edge which propagates in the stream direction. The growth of this disturbance is therefore the maximum growth. The disturbance produced by a vibrating ribbon is also nearly two-dimensional and propagates in the stream direction. The growth of this disturbance would also be the maximum.

Figure 5.2 shows the type of boundary layer disturbance that is generated in the unexcited case. This figure shows oscillographs of the velocity signal in both the unexcited (a) and the sound excited (b) cases. The sine wave in (b) is the sound excitation signal. In both (a) and (b), wave packets can be seen in the velocity signal. These packets appeared at random times and were not influenced appreciably by the sound. The packets indicate that the natural excitation of the boundary layer is indeed due mainly to free stream turbulence One should note the difference between these packets and the two-dimensional, nearly pure tone, naturally occuring oscillations reported by Liepmann et al [39]. The natural oscillations in Liepmann's experiments seem to be due to a disturbance in their tunnel

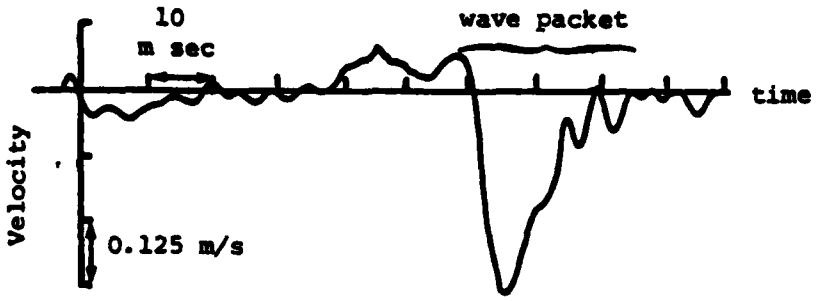

a) Natural Excitation

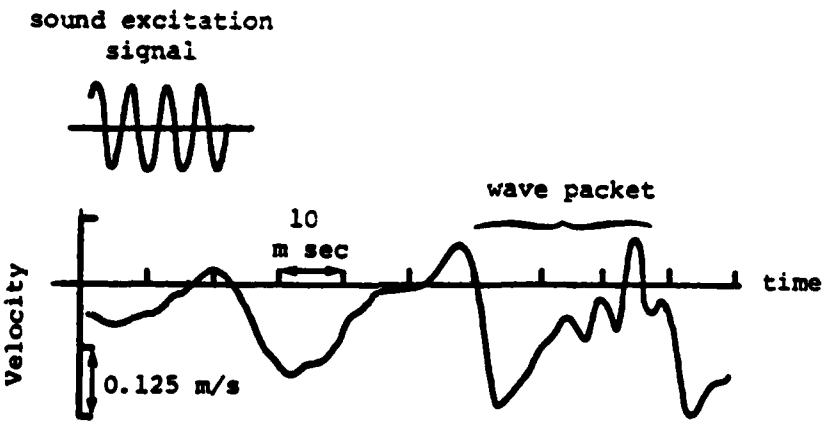

b) Sound Excitation

FIGURE 5.2 Velocity signal at x = 66.5 cm, y = 0.5 mm and U_∞ = 18.5 m/s.

which had a large spanwise correlation.

The growth of the naturally occurring disturbances at $\beta=56\times10^{-6}$ is shown in Figure 5.3. As in Figure 5.1, this figure is a plot of $\ln(A(x)/A_0)$ as a function of R, where once again R was computed assuming the mean flow was a Blasius boundary layer. The TS wave data in this figure are for the Blasius boundary layer. The data in Figure 5.3 were measured at three test speeds. The results at 29.0 and 41.0 m/s were taken from Shapiro and the 18.5 m/s data is from the present measurements. The results at 29.0 m/s and 41.0 m/s show spatial variations with wavelengths equal to the TS wavelengths. This indicates that a sound wave was present which generated a TS wave. (Recall that the spatial waves are due to the superposition of a sound wave and a TS wave of the same frequency.) The relative amount of sound and free stream turbulence that was present in each case is not known (Figure 4.2 does not discriminate between sound and turbulence). To compound matters, the pressure gradients at each flow speed were different. It is not surprising that Figure 5.3 shows different growths at the different test speeds.

The oscillations that were measured in the unexcited cases presumably included the following: 1) TS waves generated by free stream turbulence, propagating in random

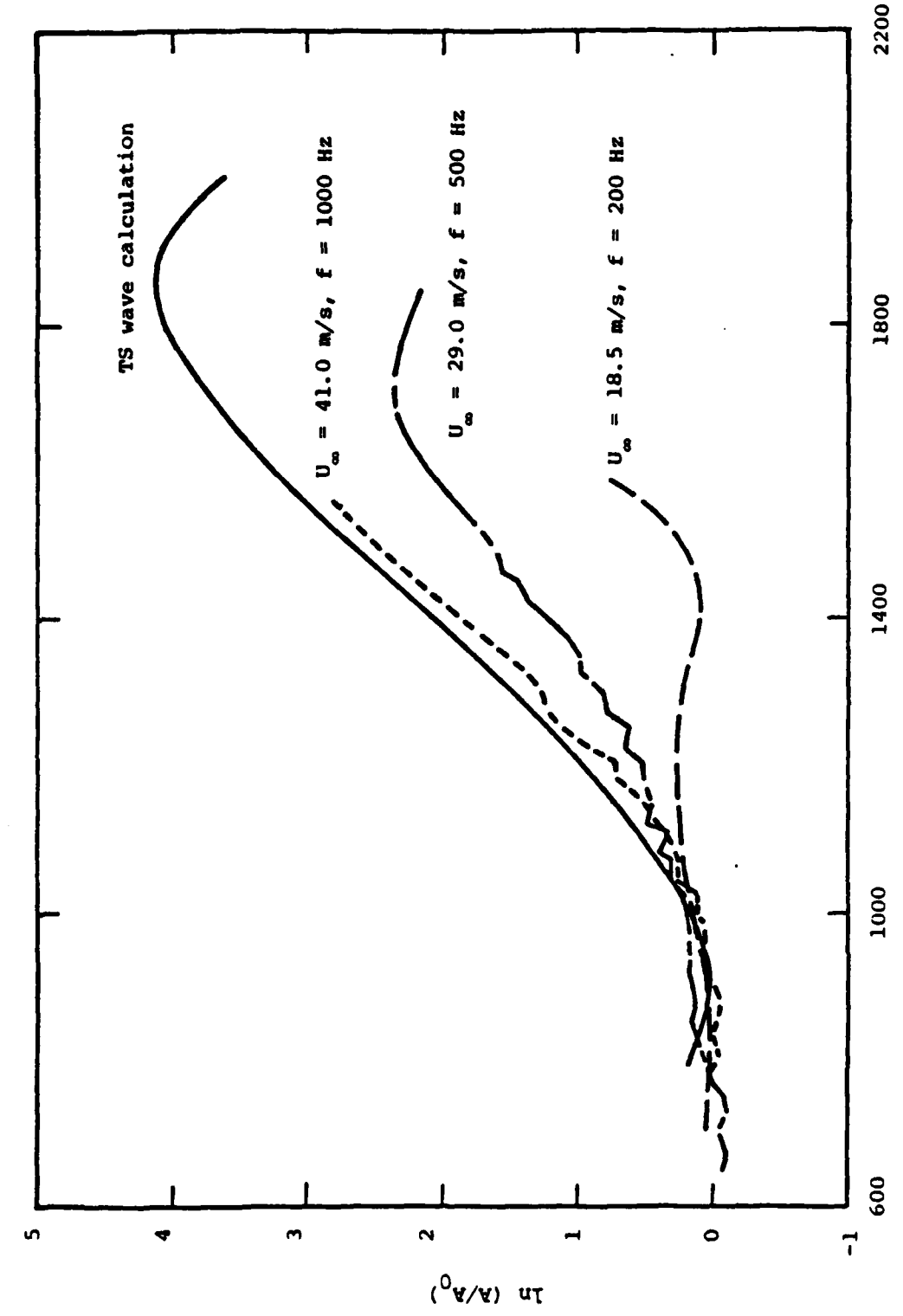

FIGURE 5.3 Boundary layer disturbance amplitudes (at $\beta = 56 \times 10^{-6}$) as functions of the Reynolds number with natural excitation.

directions and appearing in packets; 2) TS waves generated by the background acoustic noise; and 3) Stokes shear-waves due to the background noise. In the downstream portion of the boundary layer (where the Orr-Sommerfeld equation holds, and where the measurements were made) the other boundary layer disturbances (such as higher modes of the Orr-Sommerfeld equation) have decayed considerably and are not included in the measurements. Comparisons between the growth of the natural oscillations for various conditions are not conclusive. More information about the background acoustic disturbances is needed to quantify these results.

5.3 Sound Excitation of the Boundary Layer

Measurements of the excitation of a laminar boundary layer by a pure tone, plane sound wave propagating in the stream direction will now be discussed. The results are for a sound wave of magnitude 90 dB re 20 μPa (at the leading edge) and for $\beta=56\times10^{-6}$, f=200 Hz, and U_∞=18.5 m/s at the positions in the boundary layer: x=16.0, 20.3, 27.9, 39.4, and 63.5 cm. For a Blasius boundary layer, the corresponding values of R would be 759, 856, 1003, 1191, and 1513. Variations in the excitation frequency component of the velocity signal u'_f with the distance above the plate y are plotted in Figures 5.4 through 5.8 for these conditions. y is nondimensionalized by δ^* and u'_f is nondimensionalized

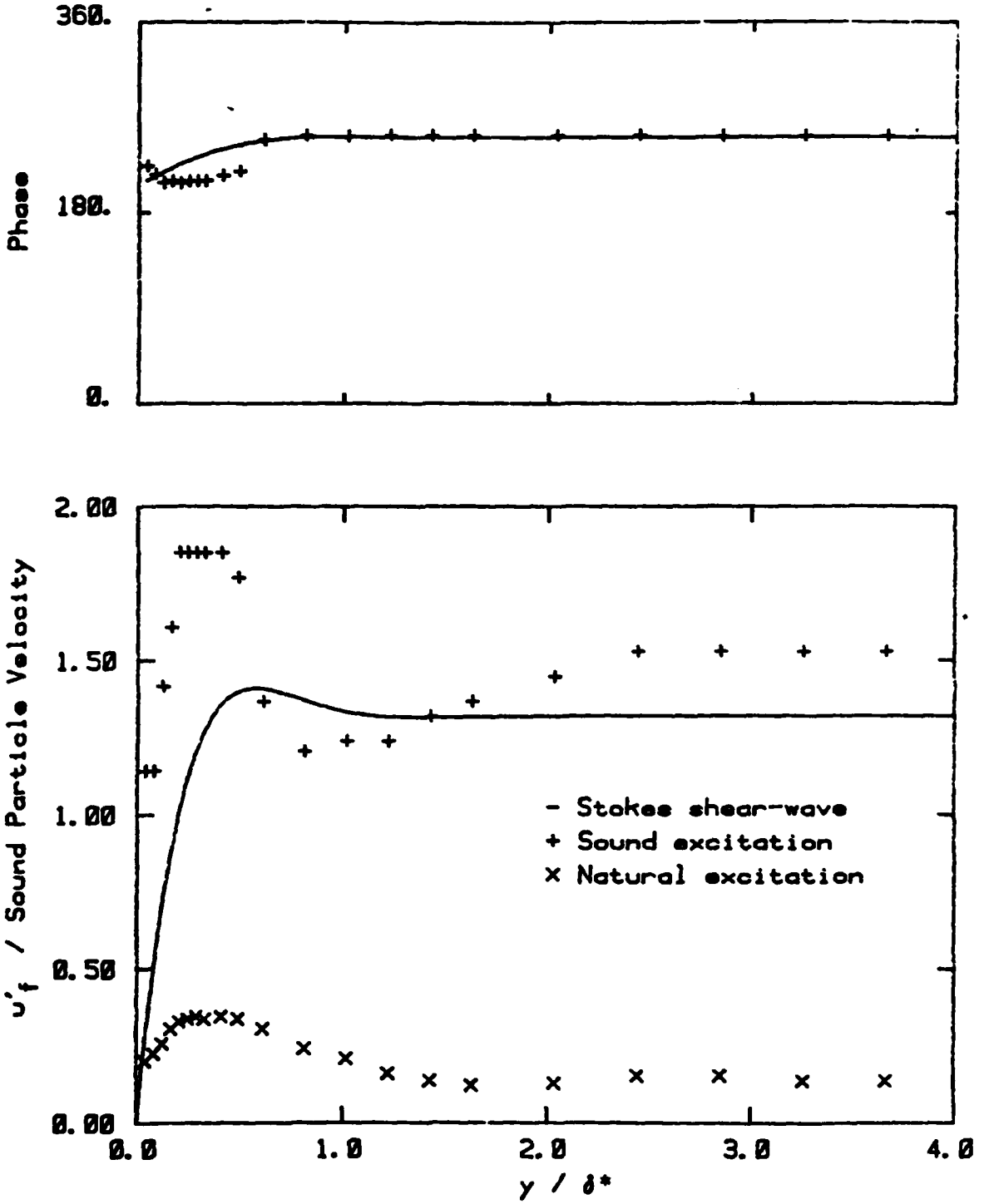

FIGURE 5.4 Velocity fluctuations (at 200 Hz) as functions of y for sound excitation (x = 16.0 cm. U_∞ = 18.5 m/s).

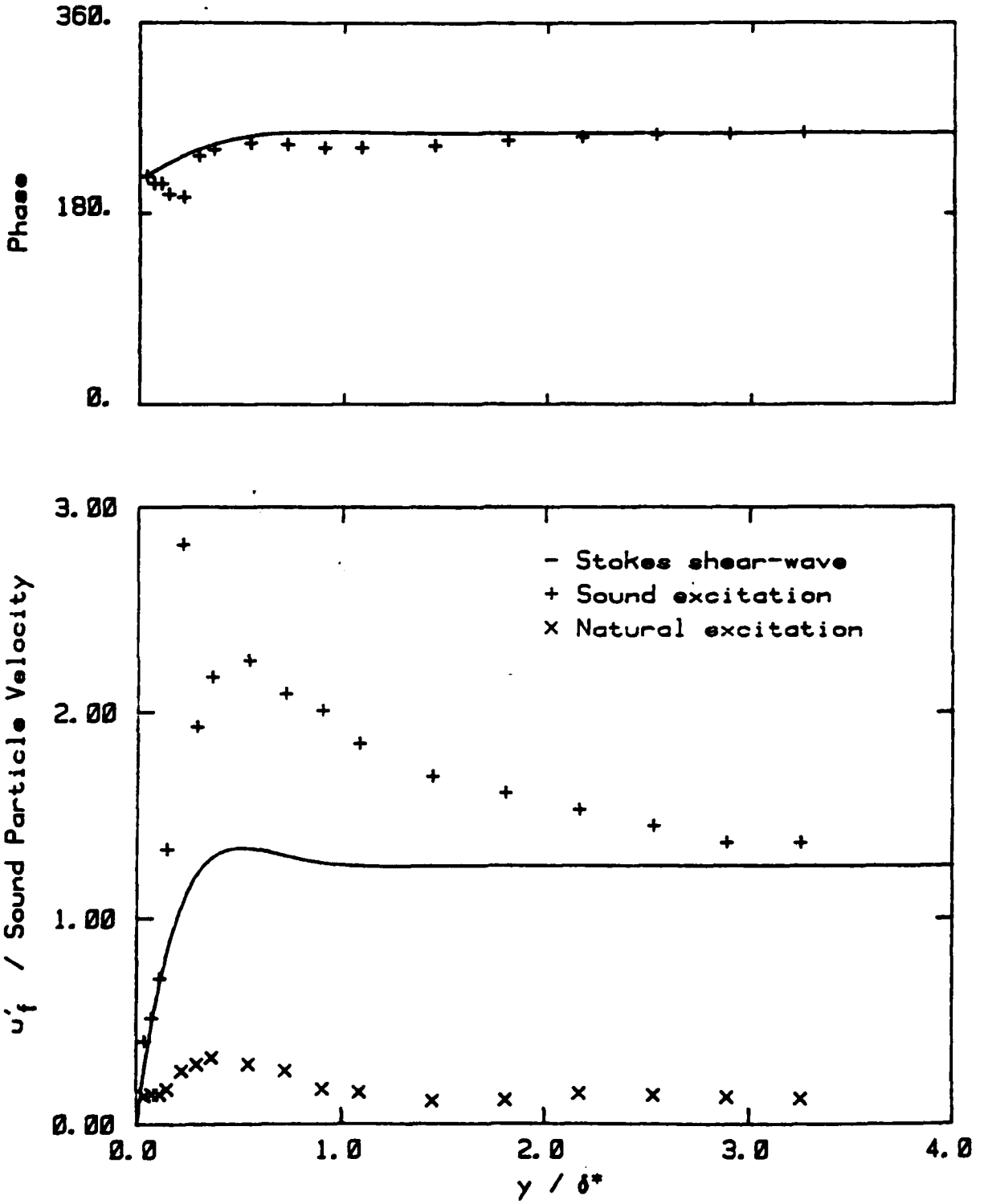

FIGURE 5.5 Velocity fluctuations (at 200 Hz) as functions of y for sound excitation ($x = 20.3$ cm, $U_\infty = 18.5$ m/s).

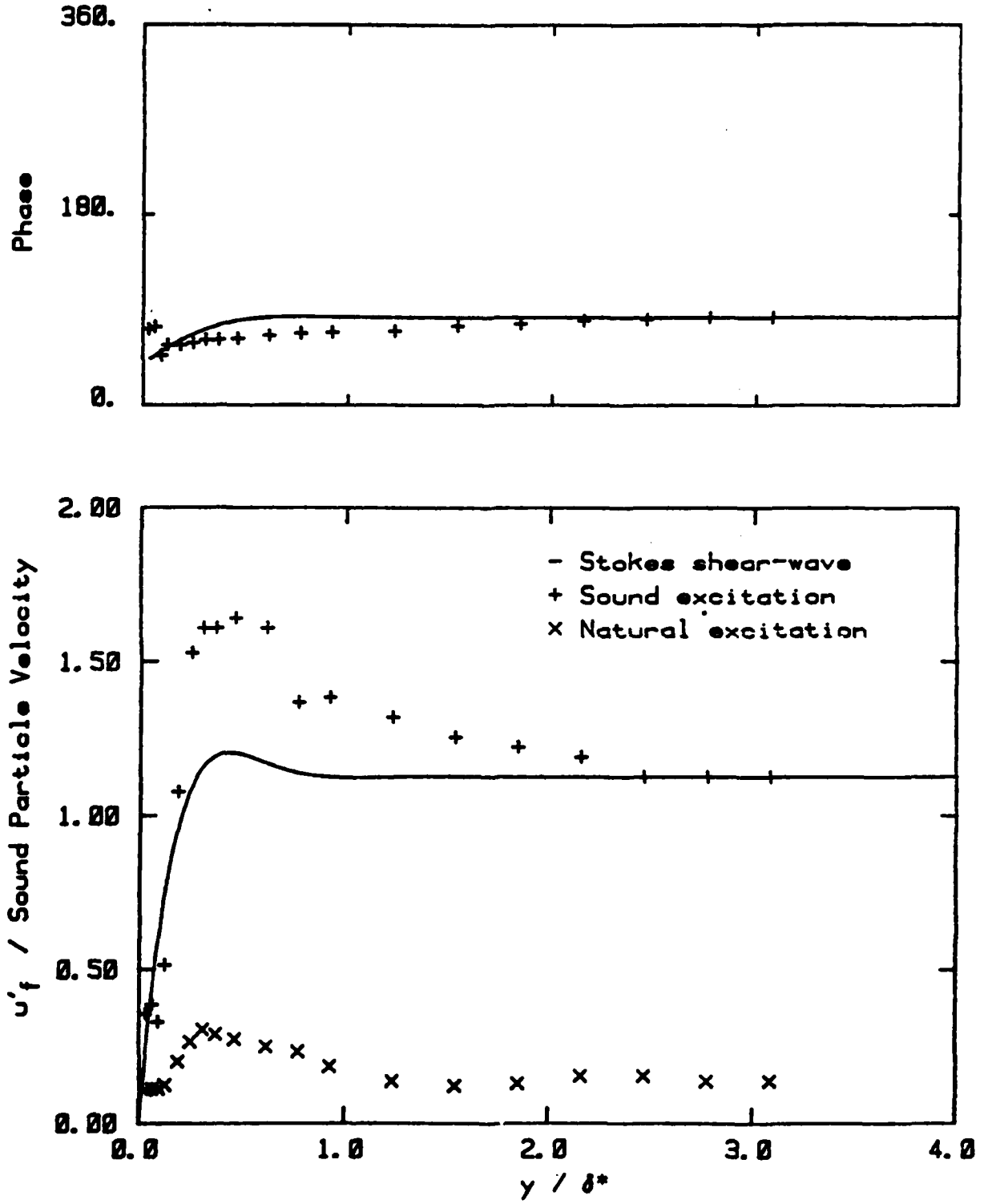

FIGURE 5.6 Velocity fluctuations (at 200 Hz) as functions of y for sound excitation (x = 27.9 cm, U_∞ = 18.5 m/s).

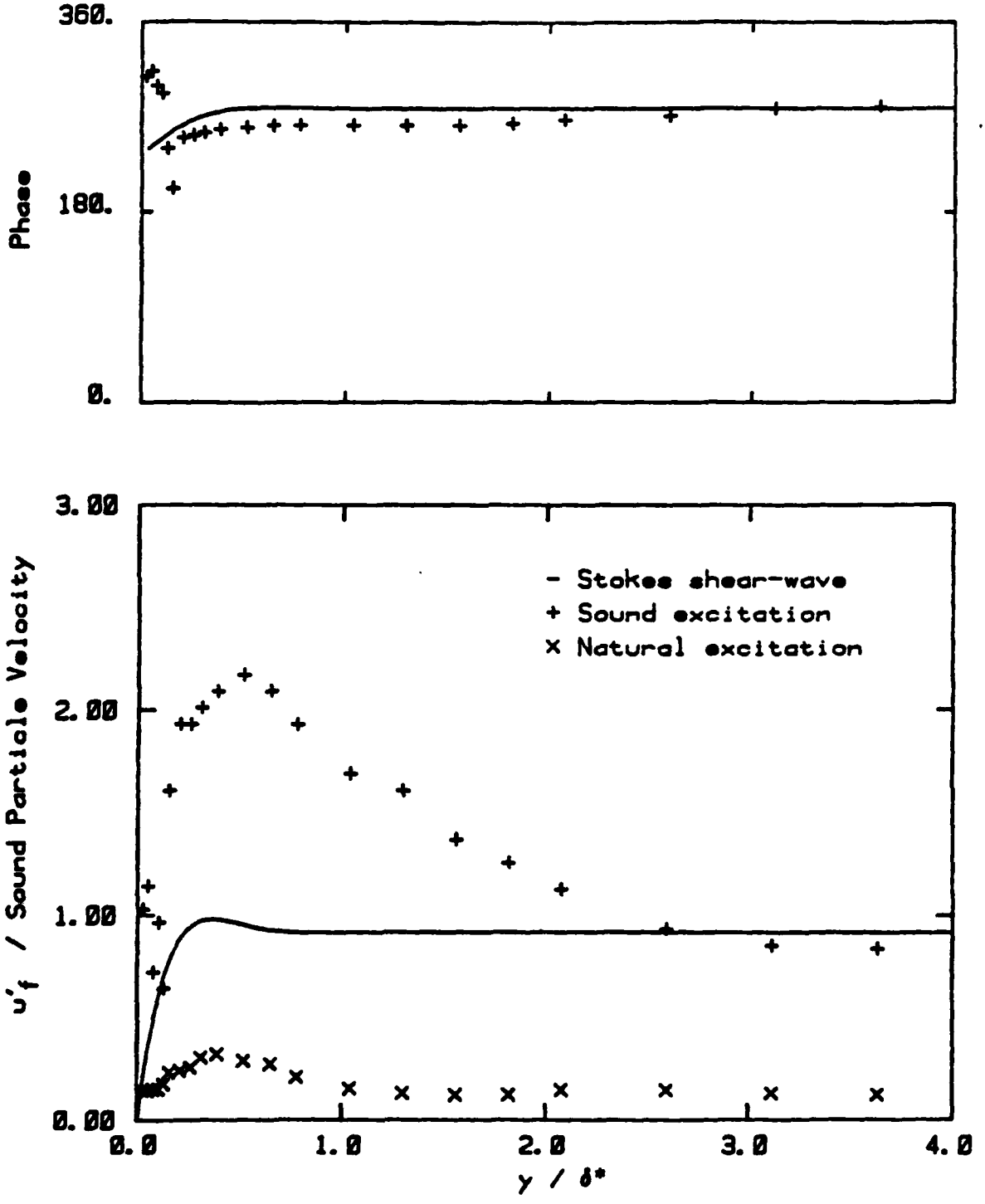

FIGURE 5.7 Velocity fluctuations (at 200 Hz) as functions of y for sound excitation (x = 39.4 cm, U_∞ = 18.5 m/s).

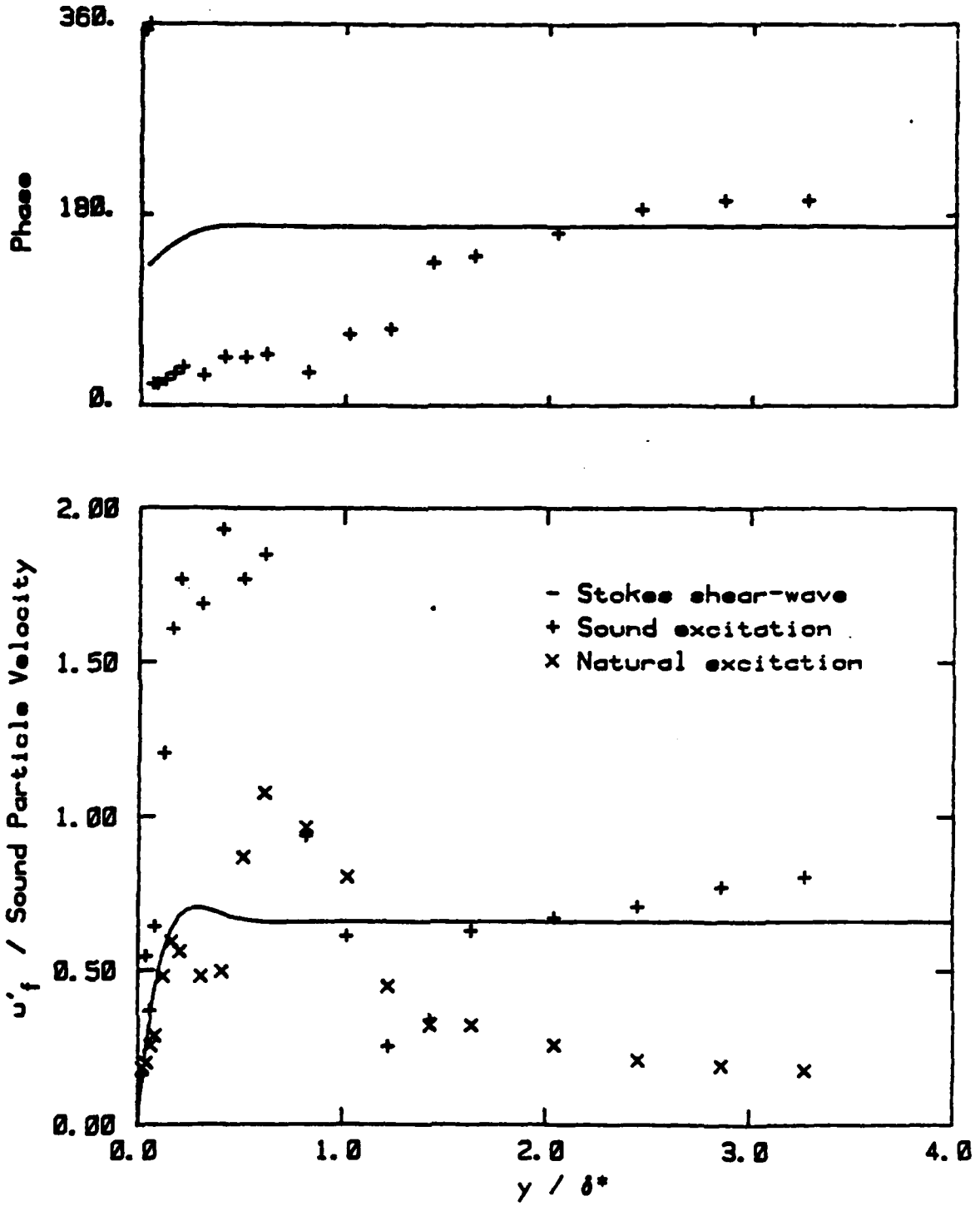

FIGURE 5.8 Velocity fluctuations (at 200 Hz) as functions of y for sound excitation ($x = 63.5$ cm, $U_\infty = 18.5$ m/s).

by the sound particle velocity at the plate's leading edge. δ^* was computed assuming that the flow was a Blasius boundary layer (with zero pressure gradient). In these figures, data for both the sound excitation and the natural excitation cases are shown. The theoretical solution for a Stokes shear-wave is also shown in the figures. The magnitude and phase of the shear wave were set to the magnitude and phase of the sound wave, outside of the boundary layer.

In Figures 5.4 through 5.8 the magnitude of the velocity, u'_f, is larger in the excited case than it is in the unexcited case. However, other than a resemblance to the shear wave in some of the figures, the excited data show no clear trends. Since the Stokes shear-wave is completely decoupled from the TS wave in the double layer (in the linear approximation), the shear wave was (vectorily) subtracted from the excited data in Figures 5.4 through 5.8. The results of this subtraction are plotted in Figures 5.9 through 5.13. In these figures, the same scales are used, and the computed TS wave shapes are shown. The TS wave shapes were computed assuming the flow was a Blasius boundary layer, and the magnitudes and phases were adjusted to best match the excited data. These figures show that the excited results still have larger magnitudes than the unexcited results and they generally agree well with the TS

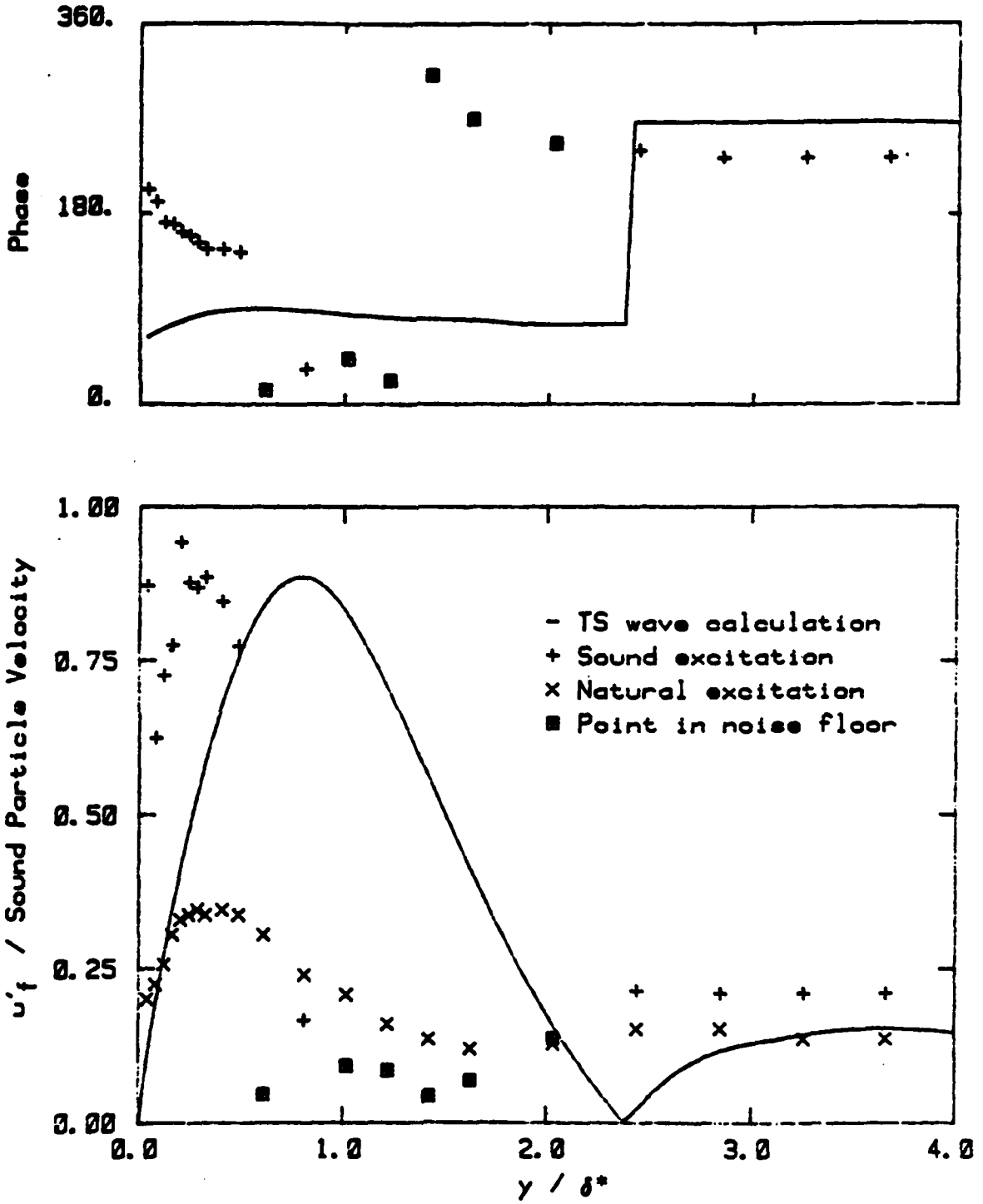

FIGURE 5.9 Velocity fluctuations (at 200 Hz) as functions of y for sound excitation. The sound excited results do not include the Stokes shear-wave ($x = 16.0$ cm, $U_\infty = 18.5$ m/s).

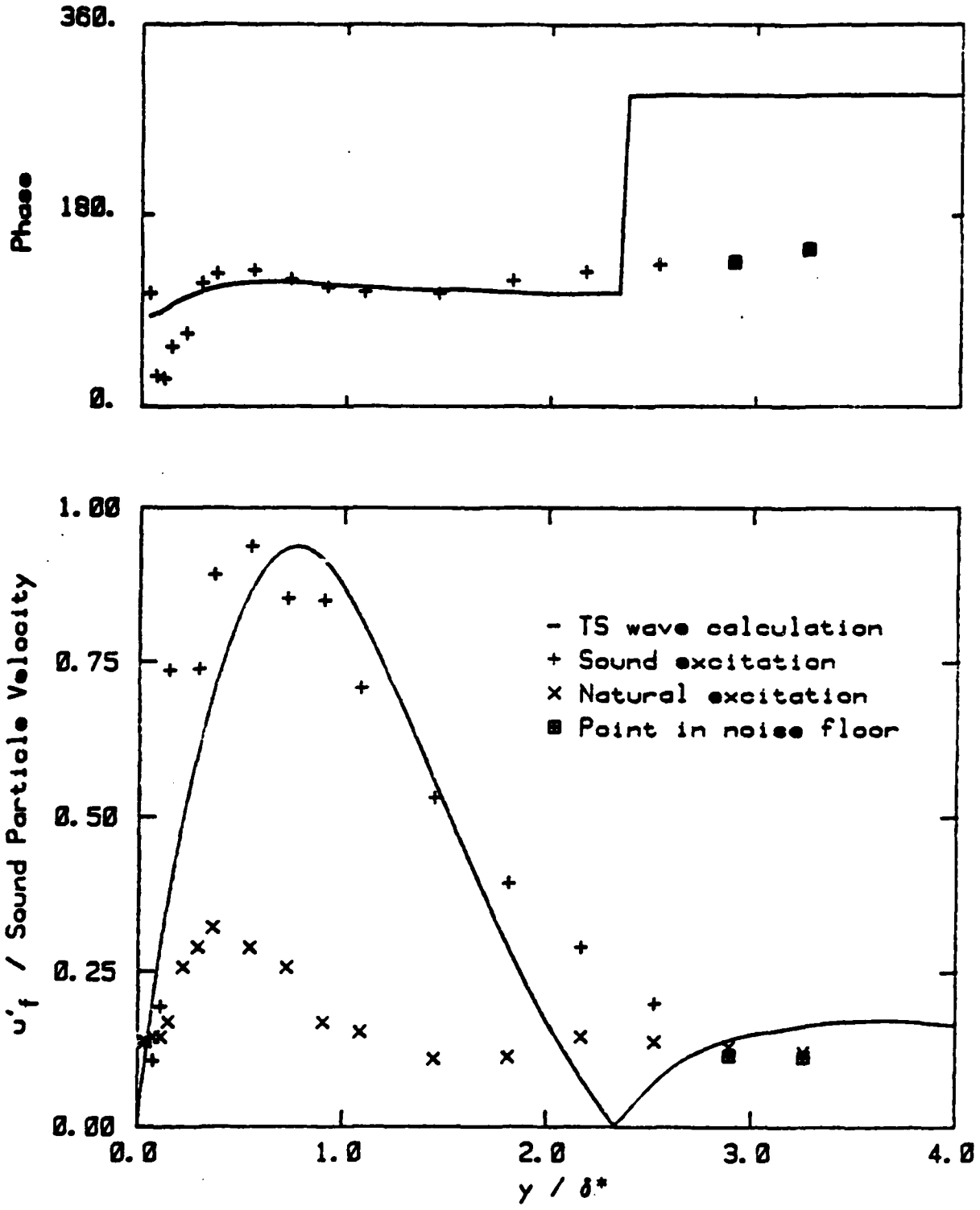

FIGURE 5.10 Velocity fluctuations (at 200Hz) as functions of y for sound excitation. The sound excited results do not include the Stokes shear-wave (x = 20.3 cm, U_∞ = 18.5 m/s).

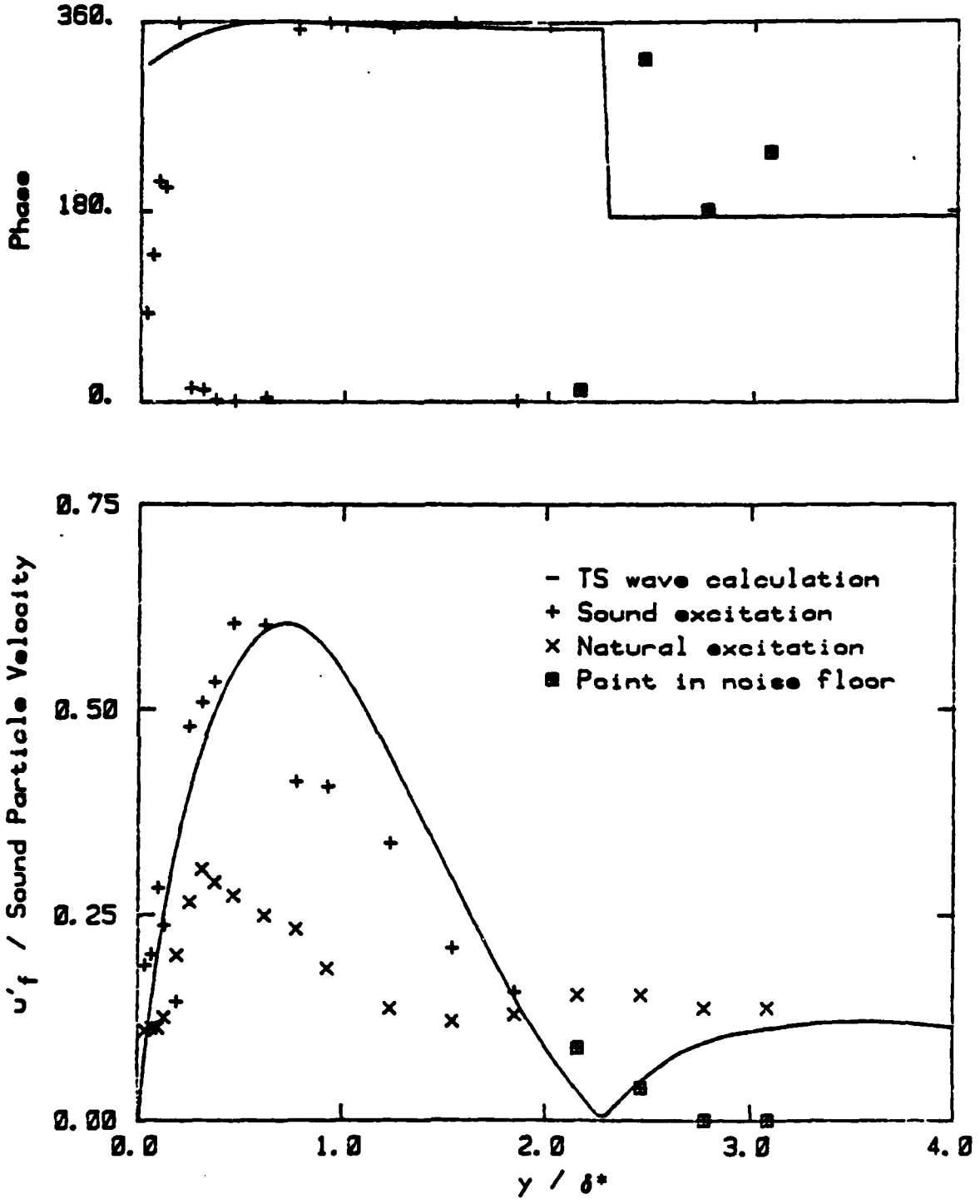

FIGURE 5.11 Velocity fluctuations (at 200 Hz) as functions of y for sound excitation. The sound excited results do not include the Stokes shear-wave (x = 27.9 cm, U_∞ = 18.5 m/s).

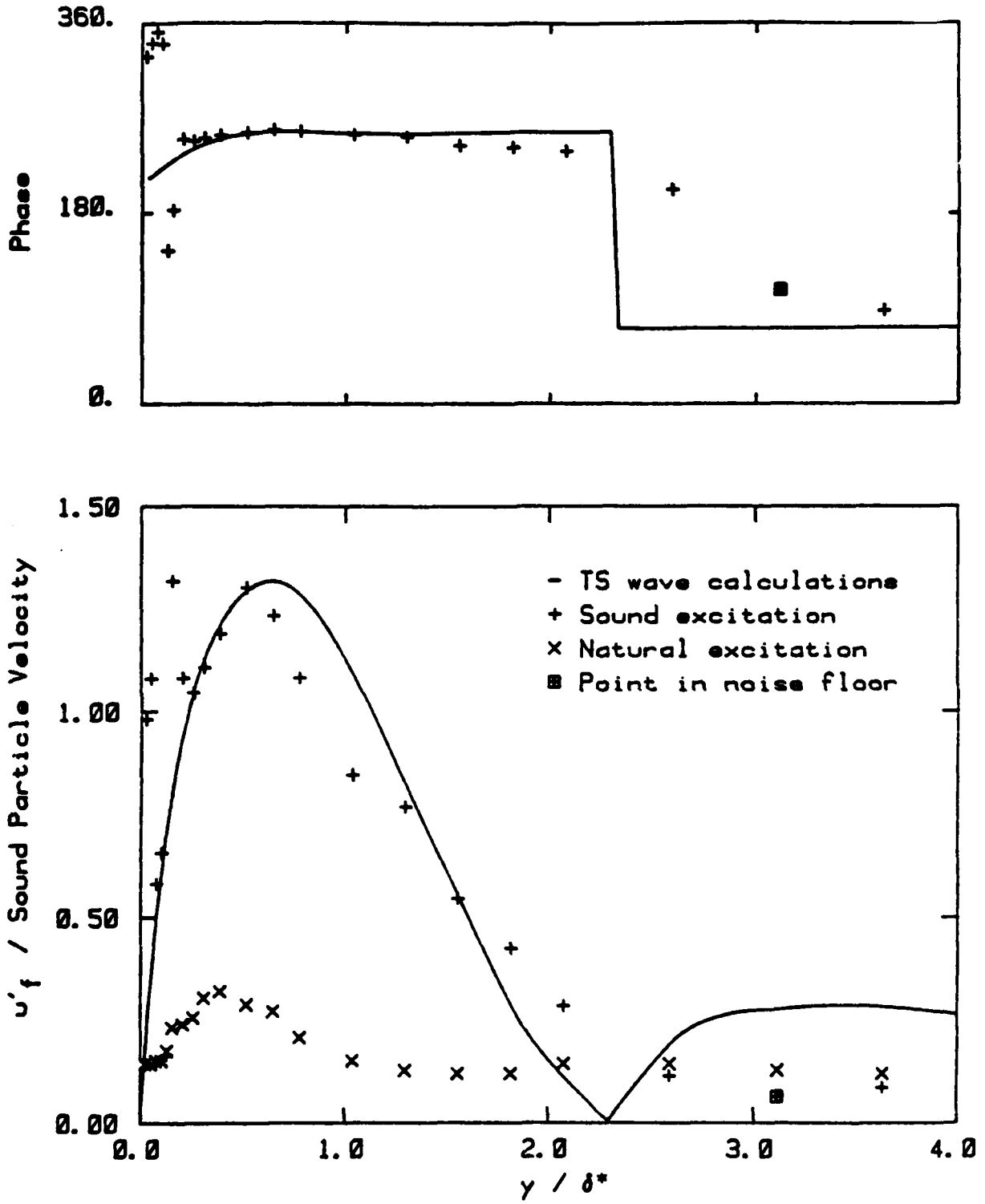

FIGURE 5.12 Velocity fluctuations (at 200 Hz) as functions of y for sound excitation. The sound excited results do not include the Stokes shear-wave (x = 39.4 cm, U_∞ = 18.5 m/s).

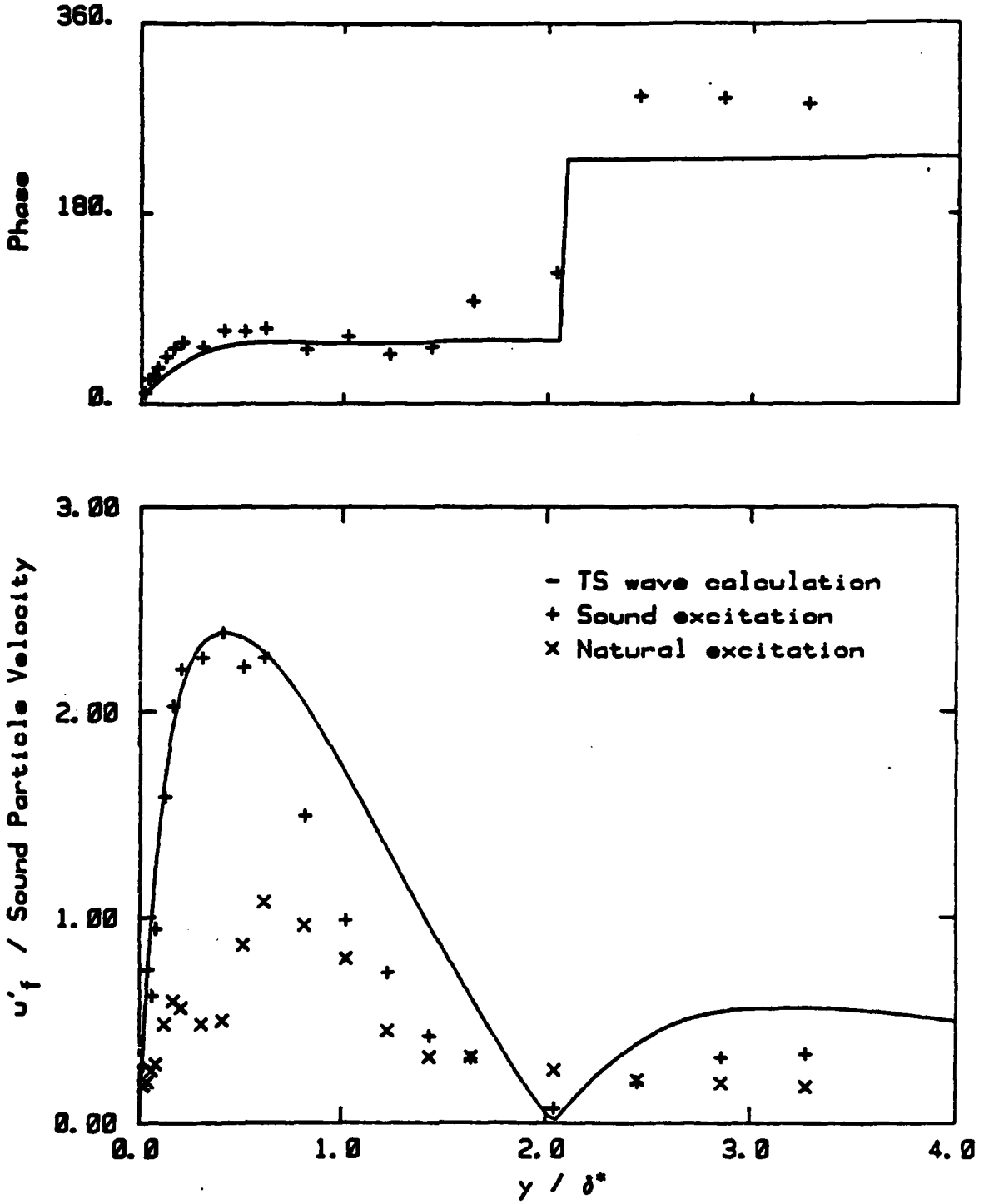

FIGURE 5.13 Velocity fluctuations (at 200 Hz) as functions of y for sound excitation. The sound excited results do not include the Stokes shear-wave (x = 63.5 cm. U_∞ = 18.5 m/s).

wave shapes. Near the plate ($y/\delta^*<0.3$), the data were influenced by heat transfer to the plate and do not agree well with the TS wave calculations. Some of the data points in these figures are marked as being in the noise of the measurements. At these points, the result of the subtraction was less than 10% of the original measurement.

Figures 5.9 to 5.13 show that the sound excitation does indeed generate a TS wave in the downstream portion of the boundary layer which has a magnitude that is larger than the oscillations occuring in the unexcited case. At each point in the boundary layer, the phase of this TS wave is constant in time with respect to the sound wave, indicating that its origin is at a fixed location in the boundary layer. The results of Goldstein [47] and Murdock [48] suggest that the origin of the TS wave is the leading edge of the plate.

5.4 Excitation of the Boundary Layer by Plate Vibration

Motions of the plate can also excite a laminar boundary layer. The oscillations u'_f within the boundary layer due to plate vibration are presented in Figures 5.14 through 5.17. The results are for transverse vibration of the plate, again at $\beta=56\times10^{-6}$, f=200 Hz, and U_∞=18.5 m/s with the magnitude of the vibration at the leading edge equal to the sound particle velocity at the leading edge in the sound

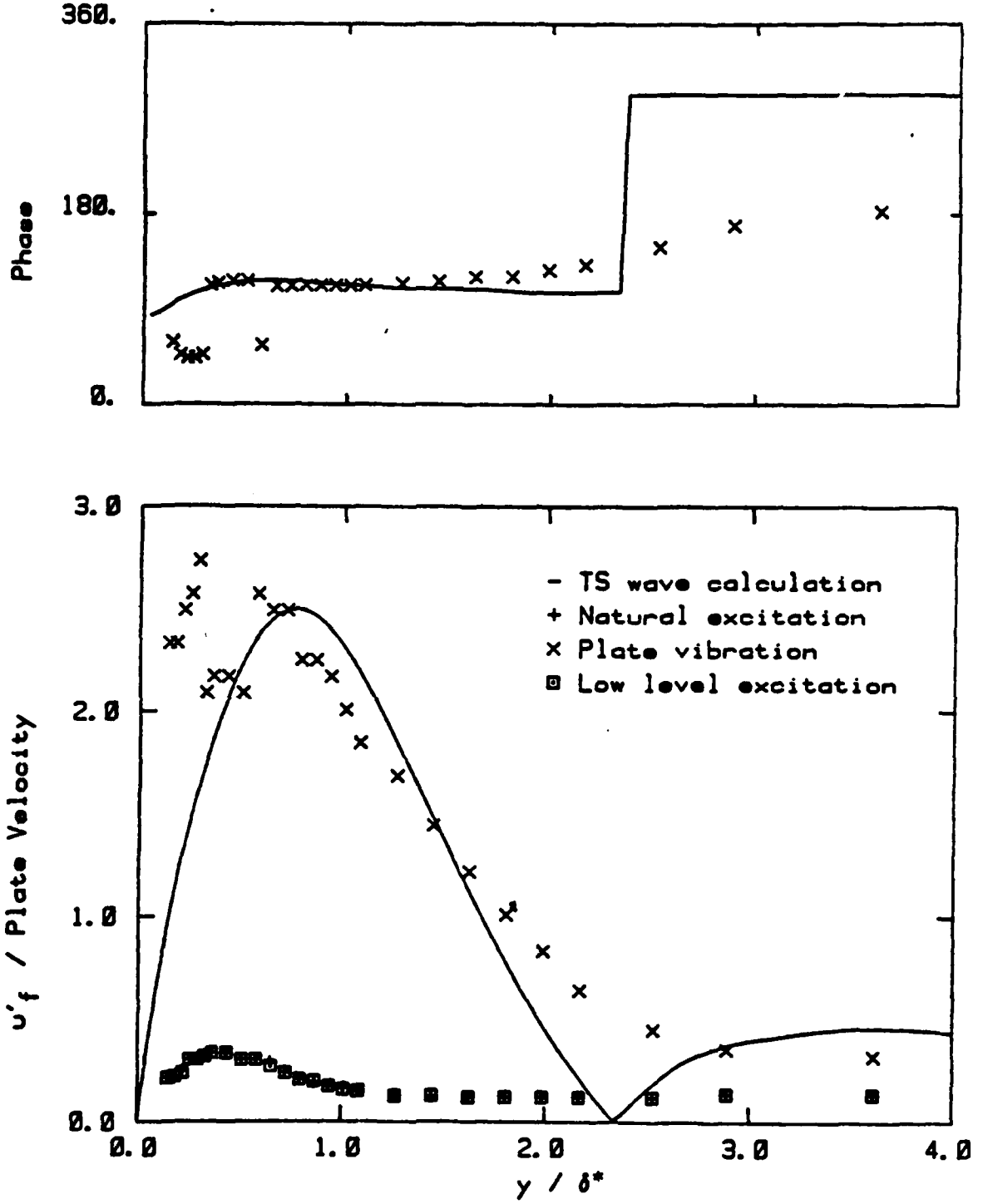

FIGURE 5.14 Velocity fluctuations (at 200 Hz) as functions of y for plate vibration ($x = 20.3$ cm, $U_\infty = 18.5$ m/s).

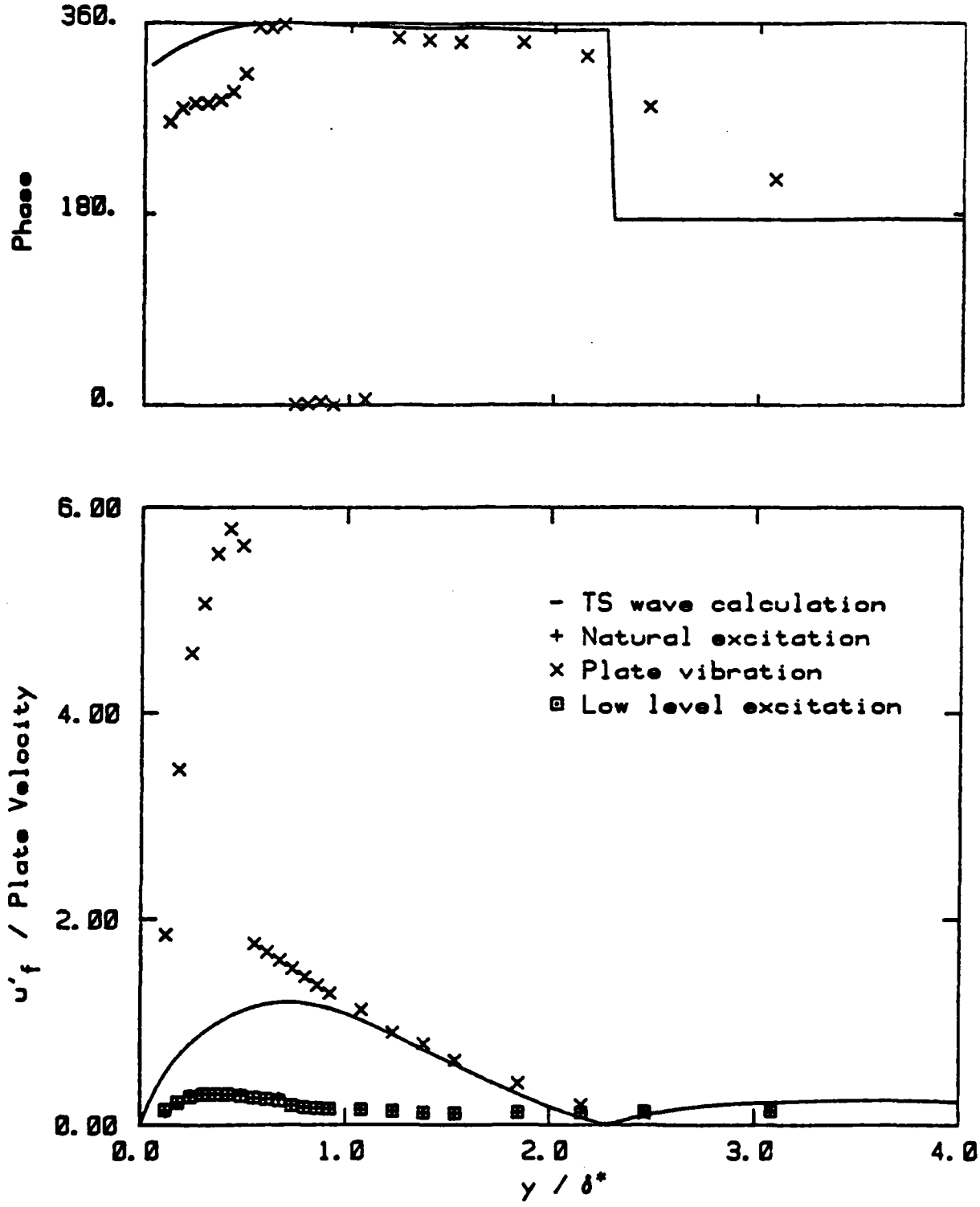

FIGURE 5.15 Velocity fluctuations (at 200 Hz) as functions of y for plate vibration (x = 27.9 cm, U_∞ = 18.5 m/s).

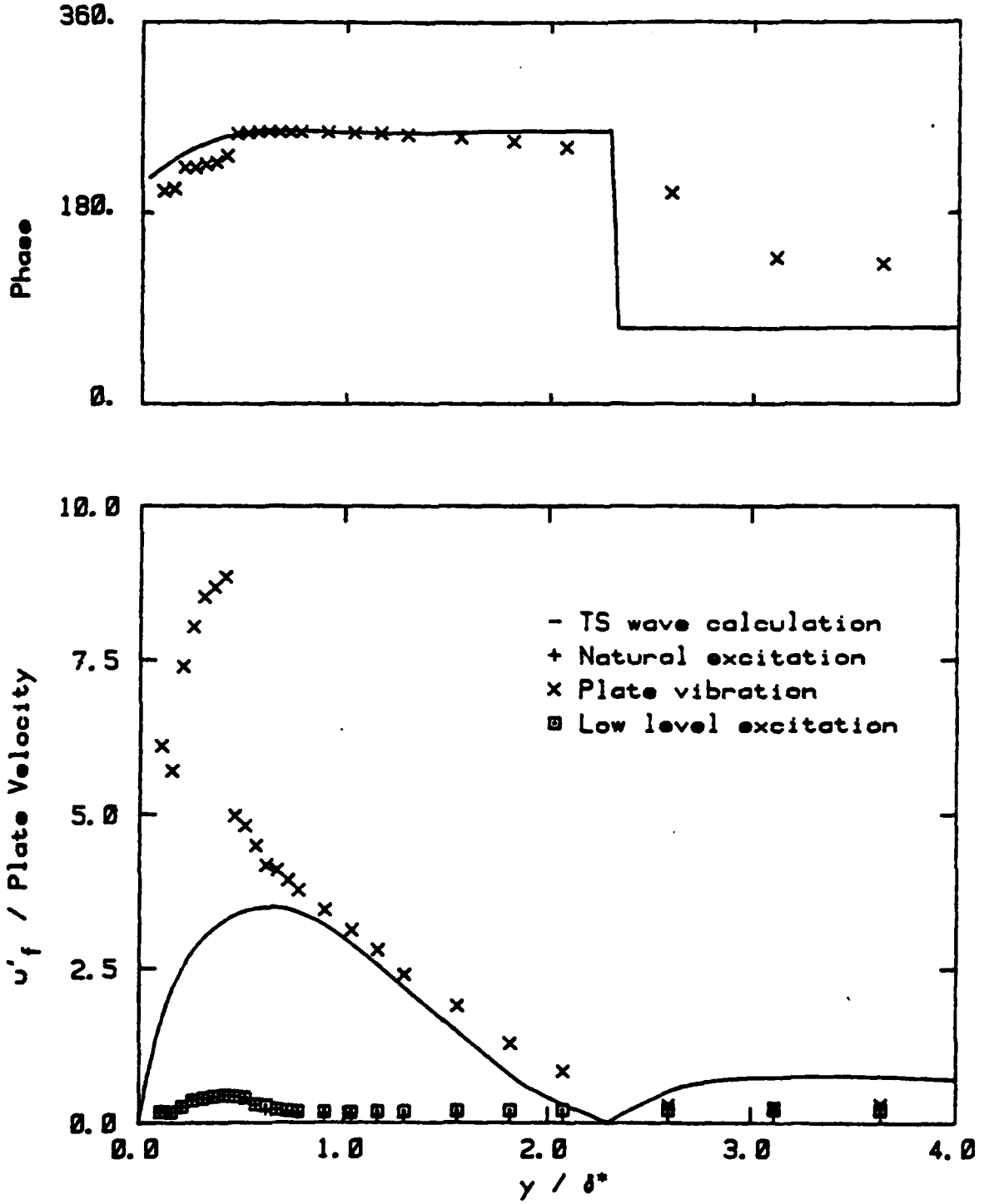

FIGURE 5.16 Velocity fluctuations (at 200 Hz) as functions of y for plate vibration (x = 39.4 cm, U_∞ = 18.5 m/s).

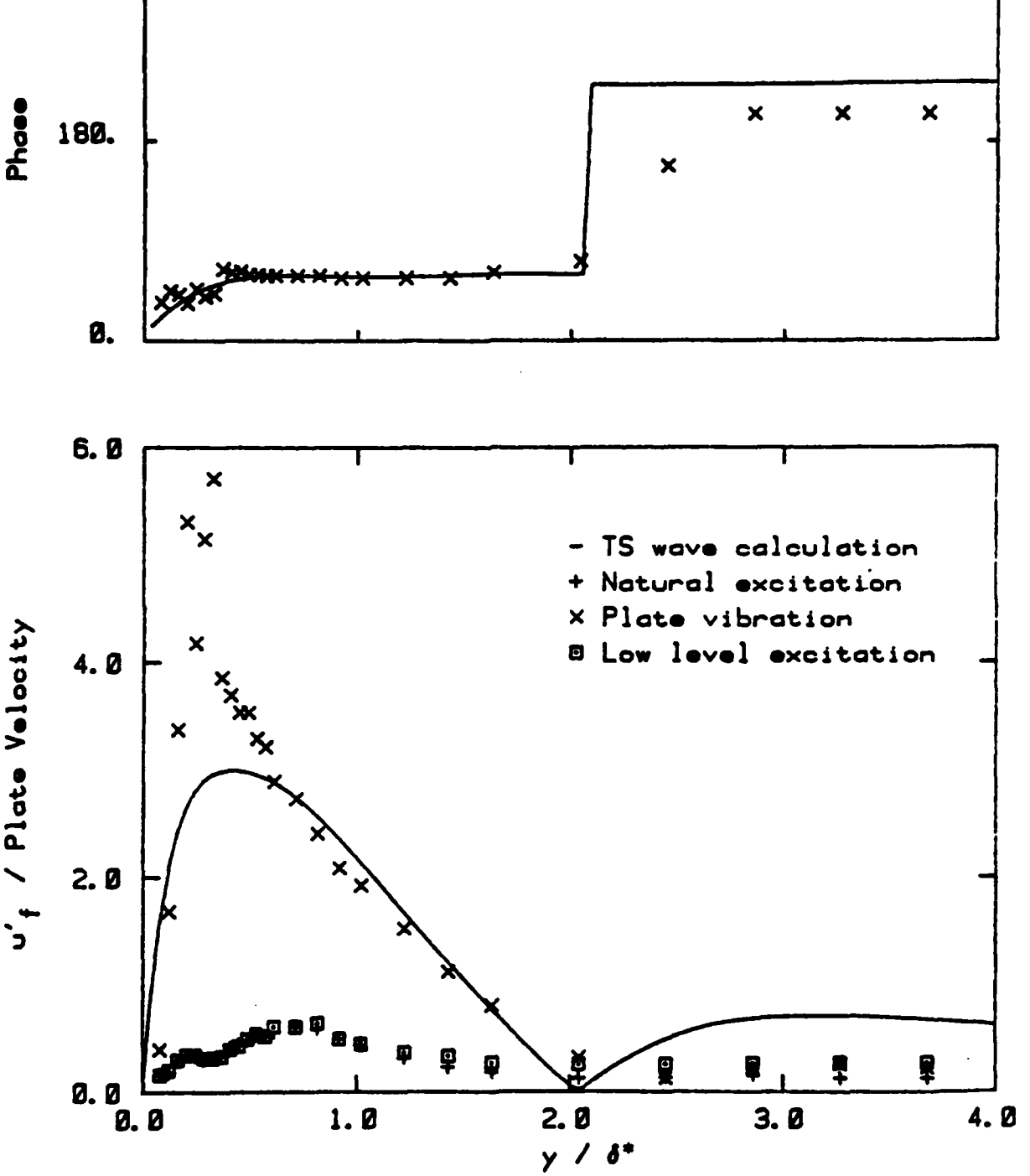

FIGURE 5.17 Velocity fluctuations (at 200 Hz) as functions of y for plate vibration ($x = 63.5$ cm, $U_\infty = 18.5$ m/s).

excitation case (1.55×10^{-3} m/s). Figures 5.14 through 5.17 are for x=20.3, 27.9, 39.4, and 63.5 cm, respectively. (The corresponding values of R for the Blasius case are 856, 1003, 1191, and 1513). The scales of the abscissa and the ordinate of these figures are the same as for the previous sound excitation figures, and data are presented for both the excited and unexcited cases.

One extra set of data is presented in Figures 5.14 through 5.17. This set of data will be called the low level excitation case. The excitation for this case was transverse vibration of the plate, where the level of vibration at the leading edge of the plate was equal to the level of vibration that was induced in the plate by the sound field, during the sound excitation tests (approximately 7.3×10^{-6} m/s, see Figure 4.24). The low level excitation measurements were made with the lock-in amplifier in the band-pass mode. The figures show no appreciable difference between the low level excitation data and the unexcited data, indicating that the boundary layer was unaffected by plate vibration during the sound excitation tests.

Figures 5.14 through 5.17 show an appreciable increase in the magnitude of the boundary layer oscillations due to plate vibration in the excited case. The computed TS wave

shapes are also shown in Figures 5.14 through 5.17. Again the TS wave shapes were computed assuming the mean flow was a Blasius boundary layer. The excited oscillations resemble the TS wave, but the sound waves generated by the vibrating plate are included in these measurements, causing noticeable differences. These differences are largest in the region near the plate ($y/\delta^*<1$). Our measurements have shown that the sound generated by the moving plate decrease in magnitude with distance from the plate. This decrease is most likely due to the sound propagation out of the ends of the test section duct, along with the absorption of sound by the duct walls. For this reason the calculated TS wave magnitudes and phases shown in Figures 5.14 through 5.17 were adjusted to best fit the excited data in the region where $1<y/\delta^*<4$. The TS waves fit the excited data reasonably well in this range. It should be noted that, even in the range $1<y/\delta^*<4$, sound waves are included in the excited data of these figures. The magnitudes of the fitted TS waves will be taken as the approximate magnitudes of the TS wave generated by the plate vibration and will be plotted in Figure 5.22 below.

Figures 5.14 through 5.17 provide evidence that the plate vibration generates a TS wave, just as in the sound excitation case. The approximate magnitude of the TS wave is greater than the unexcited data. The phase of the TS

wave at each point in the boundary layer is constant in time with respect to the plate vibration. As in the sound excited case, this indicates that the TS wave origin is at a fixed location which most likely is the plate's leading edge.

5.5 Excitation of the Boundary Layer with a Vibrating Ribbon

Experiments were conducted in which a vibrating ribbon was used to excite the boundary oscillations for two reasons. First, the ribbon generated a large, two-dimensional disturbance propagating in the stream direction and the growth of this disturbance could be easily measured. Any effect of the experimental conditions (such as the nonzero pressure gradient) on this growth would be included in the measurements. Also, a sound wave could be added to the ribbon excitation to see if the sound influenced the growth of the disturbance. The excitation was again conducted at $\beta=56\times10^{-6}$, f=200 Hz, and U_∞=18.5 m/s, and the sound excitation level was 90 dB re 20 μPa at the plate's leading edge.

Since two simultaneous excitations were to be applied, the relative phase of each excitation had to be selected. Figure 5.18 is a plot of the rms level of u'_f at a point in the boundary layer (measured in the band-pass mode) as a

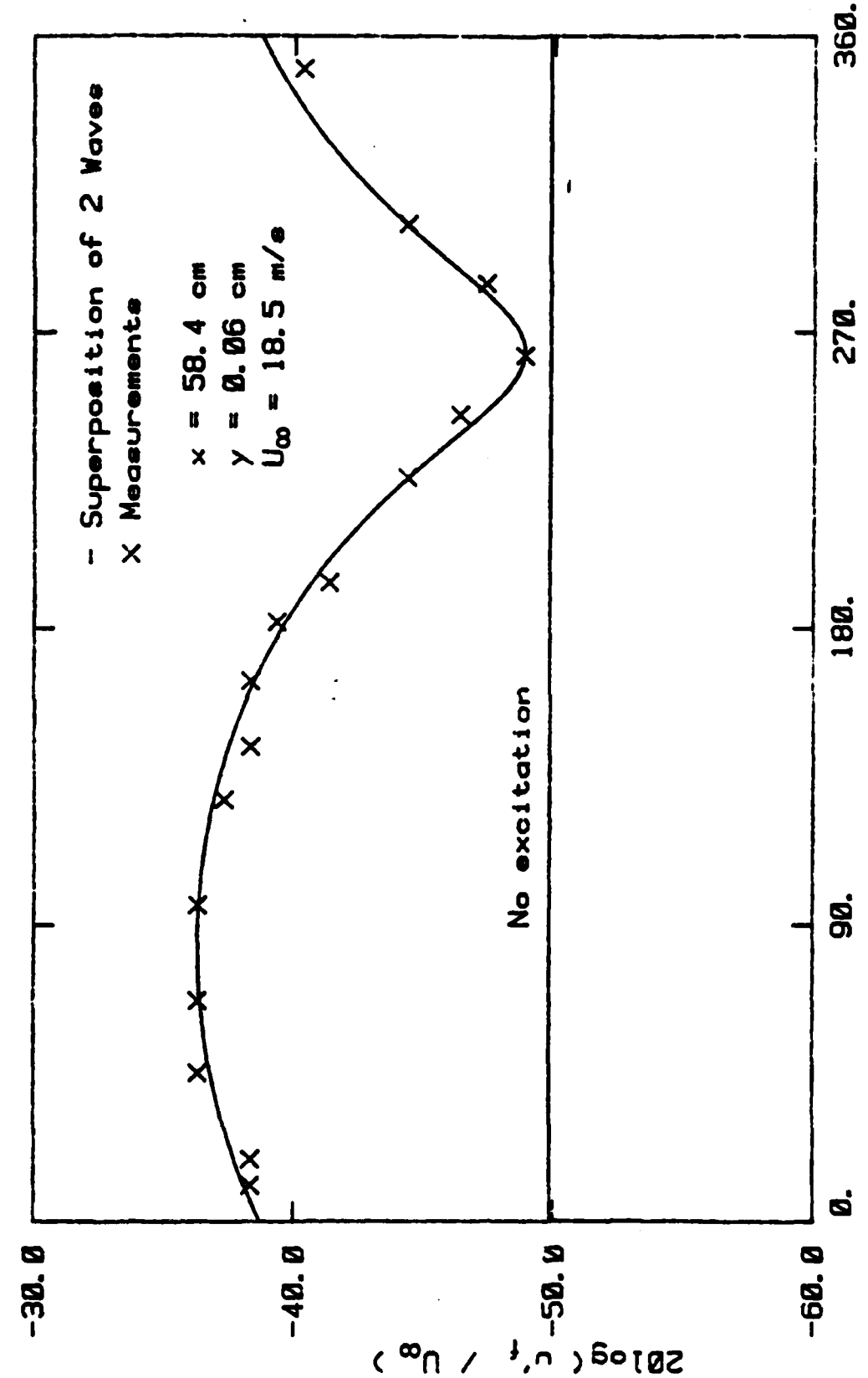

FIGURE 5.18 Fluctuating velocity in the boundary layer (at 200 Hz) as a function of the excitation phase difference (phase of speaker minus phase of ribbon drive).

function of the phase difference between the sound and ribbon excitation signals. This figure also shows the result of superimposing two waves. This result was computed from the relation

$$(u'_f)_{rms} = \sqrt{1/2(D^2 + E^2 + DE \cos(\theta_2 - \theta_1)} \qquad (5.1)$$

where $(\ )_{rms}$ denotes the root mean square, D and E are the magnitudes of the two waves, and θ_1 and θ_2 are the phases of the waves. In Figure 5.18 D, E, θ_1 and θ_2 were adjusted so the maximum and minimum values of the calculation agreed with the measurements. This figure indicates that the oscillations due to the two excitations superimpose linearly. At 270 degrees phase difference the two oscillations nearly cancel, and at 90 degrees they combine. A 90 degree phase difference was selected for the tests.

The excitation frequency component of the velocity signal u'_f is plotted versus the distance above the plate y in Figures 5.19 through 5.21, for ribbon excitation only and for both ribbon and sound excitation. Again, u'_f is nondimensionalized by the sound particle velocity at the plate's leading edge and y is nondimensionalized by δ^*. δ^* was again computed assuming that the flow was a Blasius

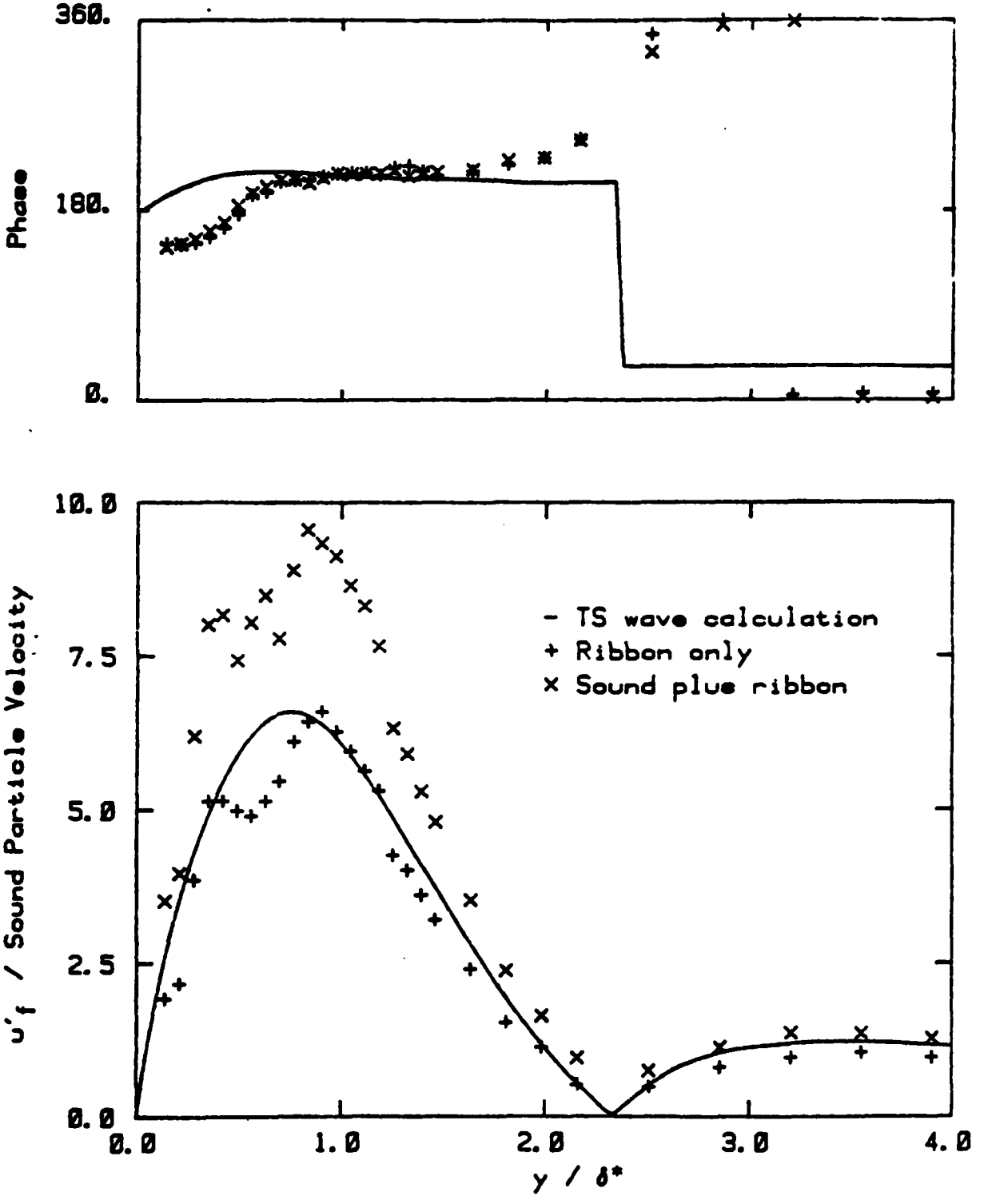

FIGURE 5.19 Velocity fluctuations (at 200 Hz) as functions of y for ribbon excitation (x = 21.8 cm, U_∞ = 18.5 m/s).

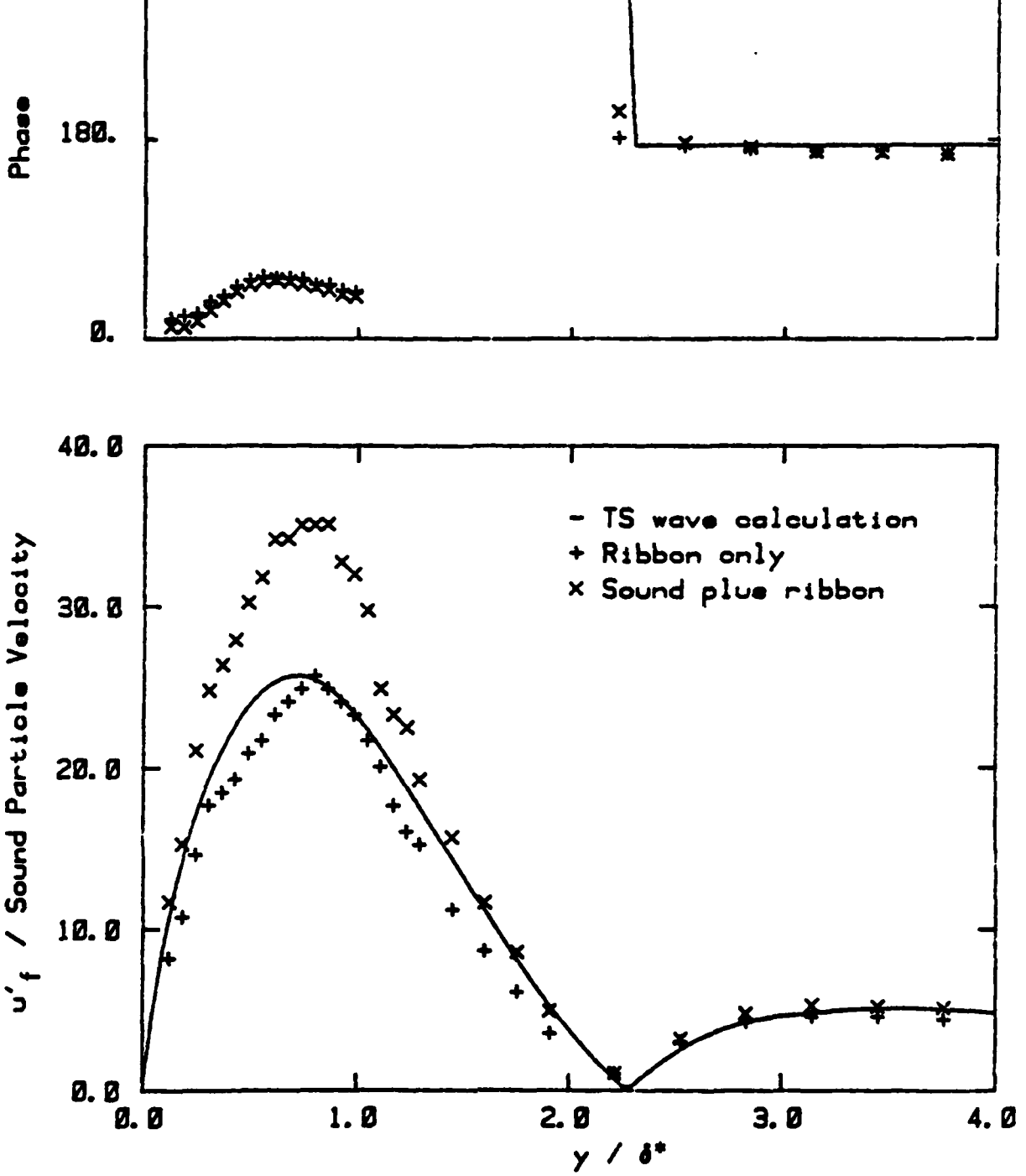

FIGURE 5.20 Velocity fluctuations (at 200 Hz) as functions of y for ribbon excitation (x = 27.9 cm, U_∞ = 18.5 m/s).

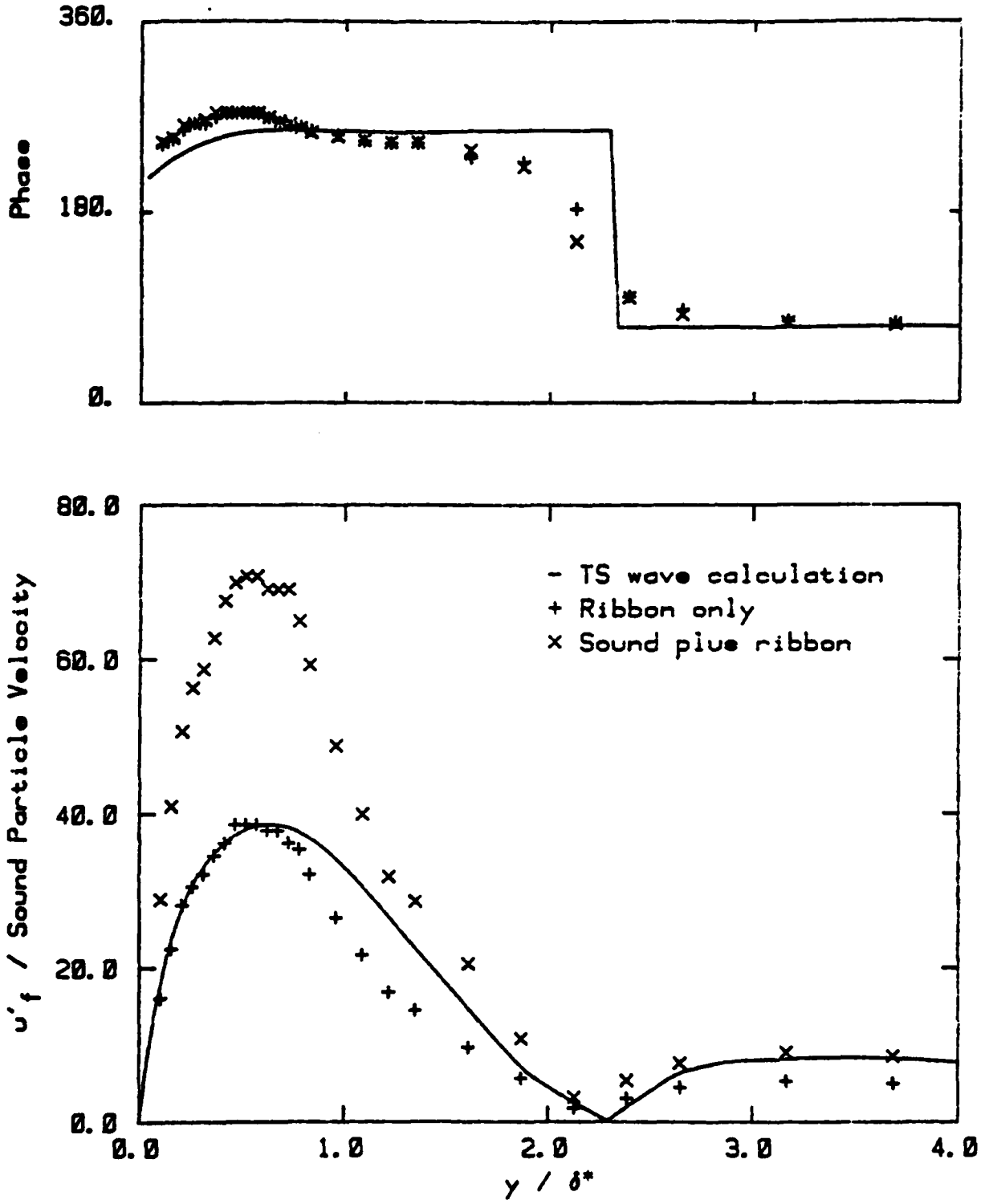

FIGURE 5.21 Velocity fluctuations (at 200 Hz) as functions of y for ribbon excitation (x = 39.4 cm, U_∞ = 18.5 m/s).

boundary layer with no pressure gradient. The data for these figures were measured at x=21.8, 27.9, and 39.4 cm (the corresponding values of R for the Blasius case are: 887, 1003, and 1191). The calculated TS wave shapes are also shown (for the Blasius boundary layer case), and the magnitudes and phases of the TS waves were adjusted to best match the ribbon excitation data. The Stokes shear-wave has been removed from the sound excited data. These figures indicate that the addition of sound increased the magnitude of the oscillation, while the phase and y distribution remained the same. The agreement between the TS wave and the ribbon excited data is reasonably good. There is however a noticeable difference between these two sets of data near the peak of the TS wave, particularly in the x=21.8 cm case. This is most likely due to the higher modes of the Orr-Sommerfeld equation that were generated at the ribbon (as in the analysis of Gaster [54]). These higher modes decay as they propagate away from the ribbon, but x=21.8 cm was only 1.5 cm downstream of the ribbon (less than one wavelength), so the decay was not appreciable. The difference in the location of the TS wave peak and the peak in the ribbon excited data at x=39.4 cm (Figure 5.21) is probably due to the slightly favorable pressure gradient that was present in this region of the flow (see Figure 4.19). Our numerical calculations of the TS wave shape have shown that a favorable gradient moves the TS wave peak

toward the wall, while an adverse gradient moves the peak away from the wall. Figure 5.20 indicates that a jump in the phase of the measurements occurred near $y/\delta^* = 1$. This was actually due to a shift in the relative phase of the ribbon exciter. This phase shift should not be attributed to an unusual characteristic of the data at this point.

One would expect the higher modes of the Orr-Sommerfeld equation to merely superimpose with the TS wave near the ribbon. The effect of the higher modes could then be obtained by subtracting the TS wave from the measured data. However, this would require knowledge of the magnitude and phase of the TS wave as well as the higher modes involved. Clearly, this area warrants further research.

The growth of the disturbances generated by the ribbon and the sound wave is shown in Figure 5.22. As in Figure 5.1, $\ln(A(x)/A_0)$ is plotted versus R. Three sets of data are plotted in Figure 5.22, viz: 1) the calculated growth of a TS wave for the Blasius case, 2) the growth of the disturbance generated by the ribbon alone, and 3) the growth of the disturbance generated by the sound and the ribbon acting simultaneously (the Stokes shear-wave has been subtracted from this data). The most noticeable feature of Figure 5.22 is that when sound is added, the growth of the disturbance is unchanged. This indicates that the sound has

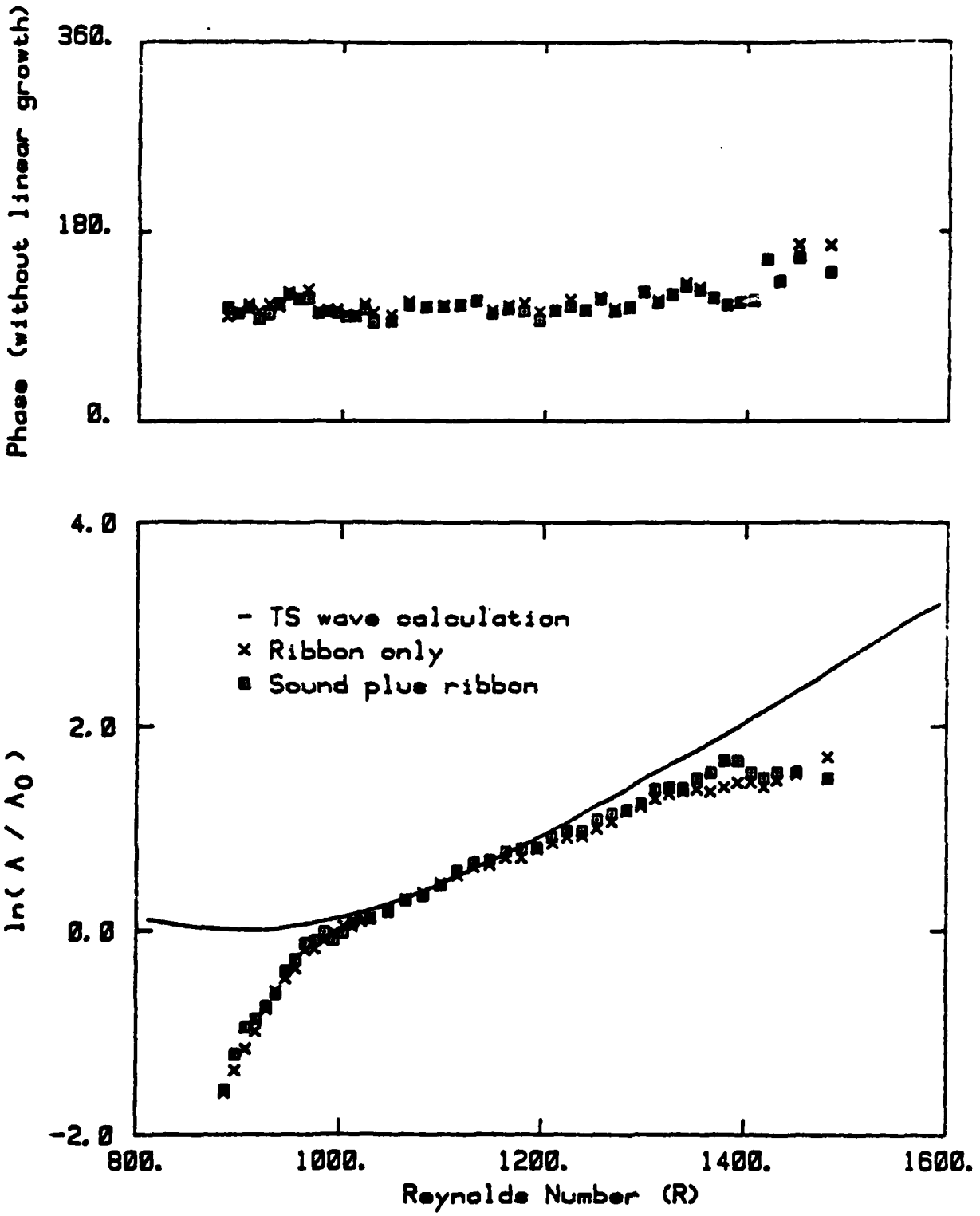

FIGURE 5.22 Boundary layer disturbance amplitudes (at $\beta = 56 \times 10^{-6}$) as functions of R ($U_\infty$ = 18.5 m/s, f = 200 Hz).

no noticeable influence on these disturbances, as the linear theory predicts. A constant linear phase increase of 115 degrees/cm was subtracted from the phase measurements before they were plotted in Figure 5.22. The value 115 degrees/cm was chosen because the resulting phase showed very little variation. A phase increase of 115 degrees/cm corresponds to a constant wavelength of 3.1 cm. Our calculations have shown that the TS wavelength for the Blasius case ranges from 3.0 cm at R=856 to 3.1 cm at R=1513 for the conditions of Figure 5.22. These results indicate that the measured phase agrees well with the predicted phase of a TS wave.

Figure 5.22 also shows a strong growth in the measured fluctuations in the region where R varies from 900 to 1000. This is most likely due to the influence of the higher modes of the Orr-Sommerfeld equation that were excited at the ribbon. Recall that A(x) was measured at the point where the oscillation was maximum for each x position, and that Figure 5.19 indicates that a considerable amount of distortion occurs in the data near this maximum (when x is close to the ribbon). In order to neglect this apparent growth region, x_0 for the measured data in Figure 5.22 was adjusted until the measured data agreed with the calculated TS wave result at R=1100. Downstream of R=1200, the measured data in Figure 5.22 drops below the TS wave. This is due to the favorable pressure gradient that was present

in this region of the flow.

These results show that the vibrating ribbon generated a disturbance that quickly developed into a TS wave. This TS wave linearly superimposed with the TS wave generated by the sound. Other than generating this superimposed wave, the sound had no noticeable influence on the ribbon-generated wave. This supports the linear theory's prediction that the Stokes shear-wave and the TS wave are completely decoupled in the double layer. Evidence of the presence of the Orr-Sommerfeld equation's higher modes has also been noted.

5.6 Disturbance Growth Comparison

The growth of the TS waves excited by sound, plate vibration, and the vibrating ribbon is plotted in Figure 5.23. As in Figure 5.1, $\ln(A(x)/A_0)$ is plotted against R, with $\beta=56\times10^{-6}$. The calculated result for a TS wave in a Blasius boundary layer flow is also presented in Figure 5.23. x_0 for the sound and plate vibration data has been adjusted to match the calculated results at R=1003. x_0 for the ribbon data has been adjusted as in Figure 5.22. The Stokes shear-wave has been removed from the sound excitation data. The plate vibration data in Figure 5.22 was taken as the peak levels of the fitted TS waves of Figures 5.14

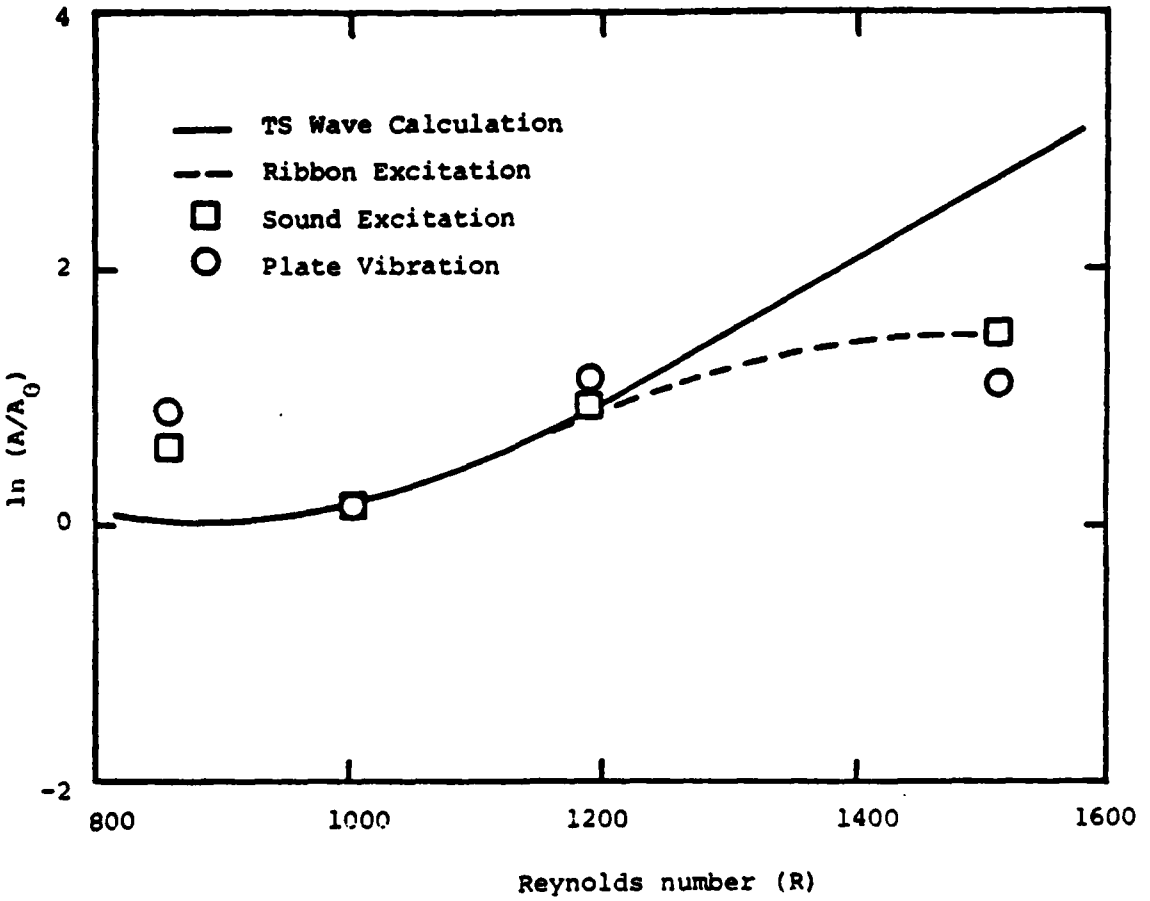

FIGURE 5.23 Boundary layer disturbance amplitudes (at $\beta = 56 \times 10^{-6}$) as functions of the Reynolds number (U_∞ = 18.5 m/s, f = 200 Hz).

through 5.17. This avoids the region of data contamination near the plate. The sound and plate vibration data follow the predicted TS wave growth except at R=856 (downstream of R=1100. the data follow the ribbon results due to the favorable pressure gradient). Figure 5.23 supports the conclusion that both the sound excitation and the plate vibration generate a TS wave in the boundary layer.

Figure 5.24 is a growth curve plot, comparing Shapiro's results to the computed TS wave growth for the Blasius case, at $\beta=56\times10^{-6}$. Shapiro did not subtract the Stokes shear-wave from his data, so the spatial waves appear in the R=600 to 1400 range. Since the shear wave and the TS wave superimpose, the effect of the shear wave can be removed by drawing a faired line through the spatial wave, as Shapiro did. The growth measured by Shapiro is larger than the computed TS wave growth because of the pressure gradients in the flow (see Figure 4.19). This increase in growth cannot be caused by the sound wave, as the sound and TS waves are completely decoupled. The result of increasing U_∞ while β remains constant is to move the adverse pressure gradient region of the flow to a higher Reynolds number range (see again Figure 4.19). Thus, one would expect higher TS wave growth rates for higher values of U_∞, if β remained constant. If there were no pressure gradients in the flow, no change in the growth rates would be expected. Figure

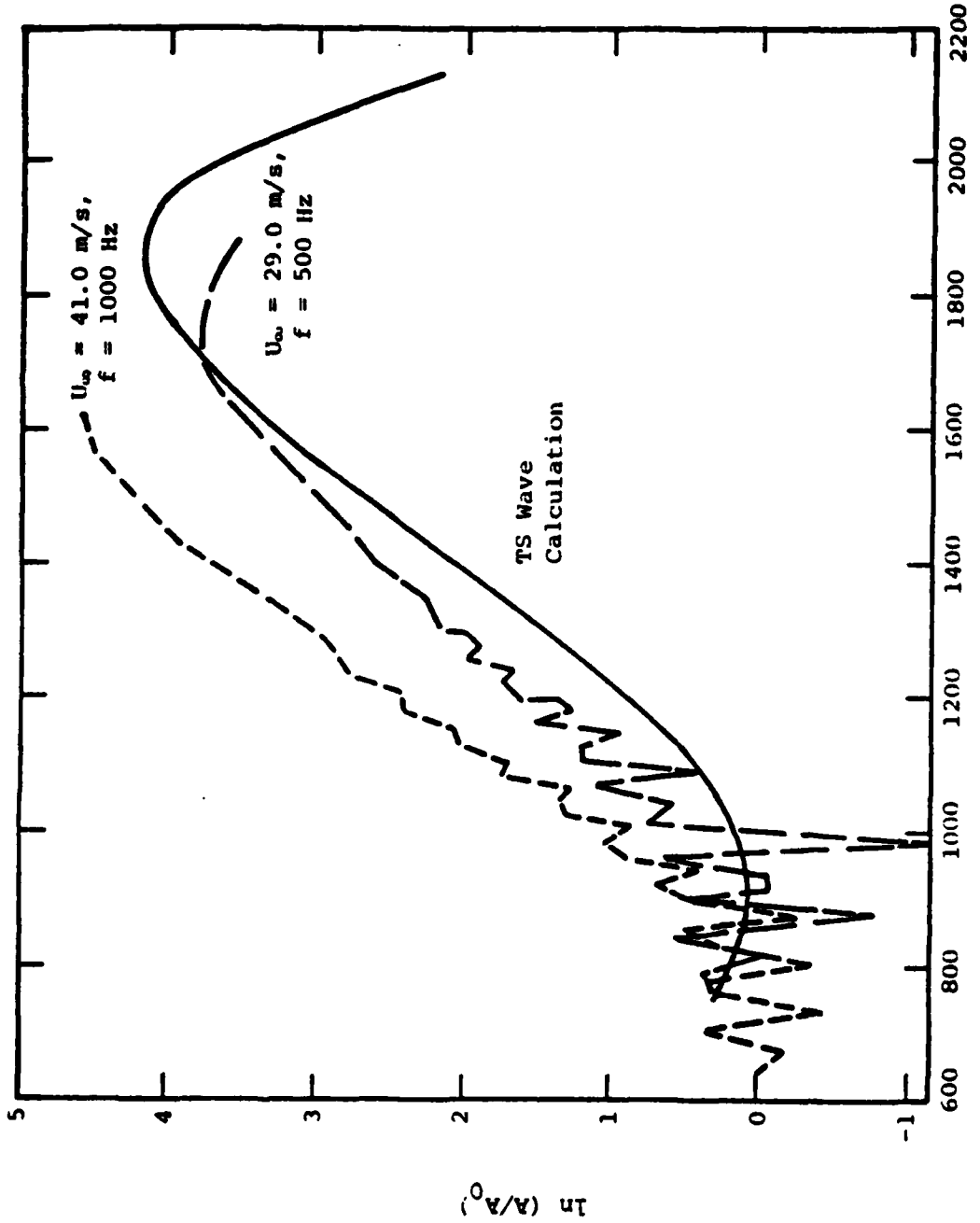

FIGURE 5.24 Sound excited boundary layer disturbance amplitudes (at $\beta = 56 \times 10^{-6}$) as functions of the Reynolds number (from Shapiro [7]).

5.24 supports these conclusions.

5.7 Cancellation of a Sound-Excited TS Wave with Plate Vibration

The results of Section 5.5 show that the TS waves generated by a sound wave and the ribbon superimpose linearly. It was thought that this superposition could possibly be used to cancel a TS wave, and thereby delaying the eventual transition to turbulence. Artificially generated TS waves have been cancelled before [32,38-40], but sound or plate vibration have not been used. The objective of this experiment was to excite a TS wave with sound and then to try disrupting the development of this wave by forcing the plate to vibrate near its leading edge. Since the naturally occurring TS waves appeared in random packets, no attempt was made to interfere with them, as Liepmann and Nosenchuck [40] did. Recall that the naturally occuring disturbances in Liepmann's experiments were two-dimensional, nearly pure tone oscillations. The present experiment was conducted at $\beta=56\times10^{-6}$, but with $U_\infty=29.0$ m/s and f=500 Hz.

The following procedure was used in the execution of the experiment. The tunnel was started and a free stream velocity of 29.0 m/s was established. A sound excitation

was then introduced at 500 Hz, and its amplitude was steadily increased until the transition to turbulence in the boundary layer moved upstream by an appreciable amount. The sound pressure level at a point 0.82 cm above the leading edge of the plate was found to be 89 dB re 20 μPa. The corresponding particle velocity was 1.3×10^{-3} m/s. The shaker was then switched on, initiating the plate vibration at 500 Hz as well. The plate vibration's magnitude and phase (with respect to the sound) were carefully adjusted until the transition region moved downstream as far as possible. The vibration velocity amplitude at the leading edge was then 2.9×10^{-2} m/s; its phase lagged the sound particle velocity by 340 degrees. Measurements of the velocity fluctuations were then made for the four excitation cases, viz: 1) no excitation, 2) sound excitation, 3) both sound and plate vibration, and 4) plate vibration only.

Figure 5.25 shows the variation in the turbulent intermittency I (the fraction of time the boundary layer is turbulent at a given point) with the streamwise Reynolds number R_x. The intermittency was estimated from oscilloscope traces of the velocity signal measured at the position within the boundary layer where the mean velocities for the turbulent and laminar intervals were equal. This method, while only an estimate, did provide a good measure of the transition to turbulence for the various excitation

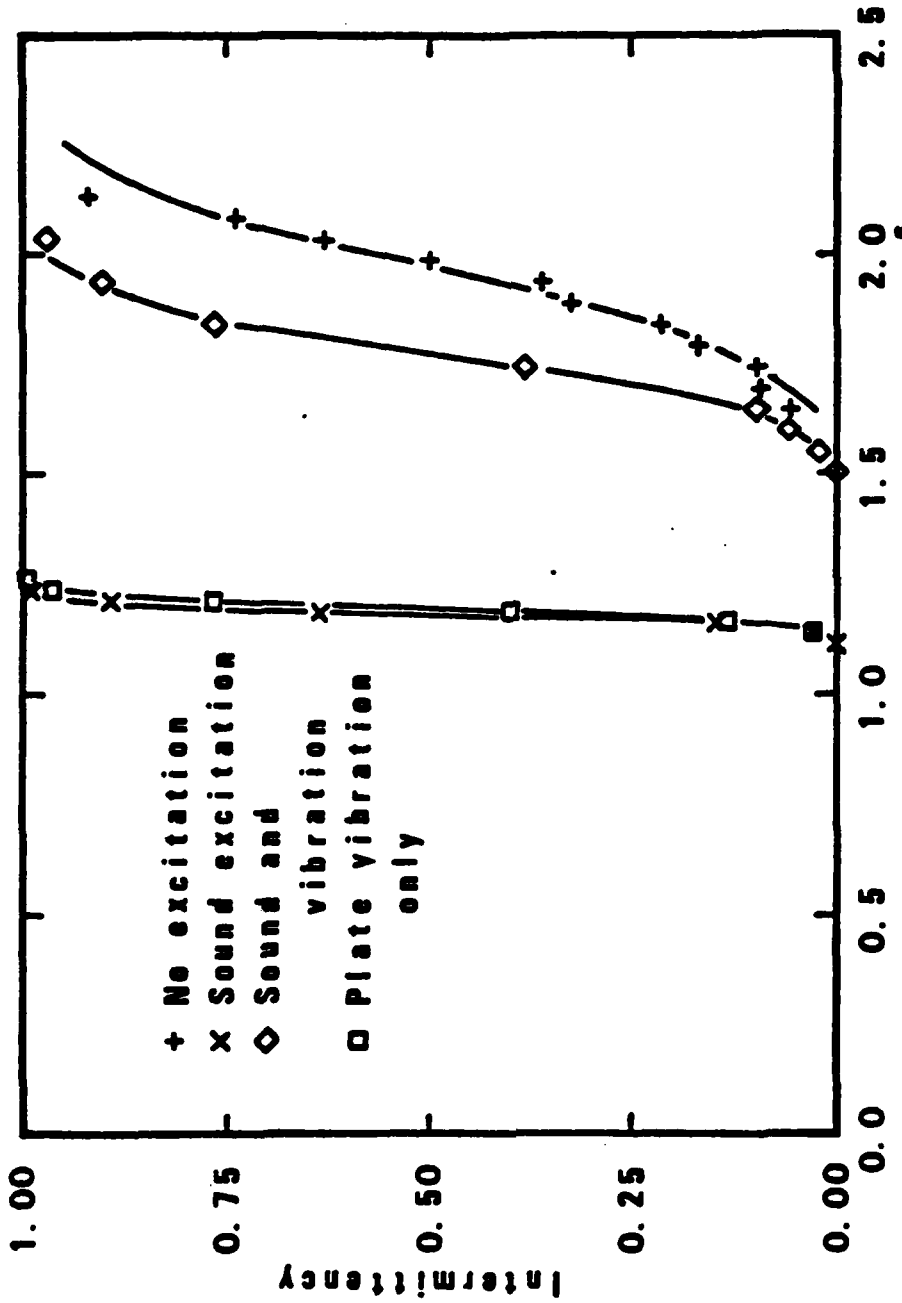

FIGURE 5.25 Intermittency as a function of streamwise Reynolds number (R_x).

cases. With no excitation, transition occurred (I=0.5) at $R_x=2.0x10^6$. In the sound excitation case, a very rapid transition occurred at $R_x=1.2x10^6$, and when plate vibration was added, the transition was delayed to $R_x=1.8x10^6$. With plate vibration as the only excitation, the transition to turbulence occurred almost at the same location as for sound excitation. The results of Figure 5.25 show that a considerable amount of cancellation does indeed occur within the boundary layer when the two excitations are applied simultaneously, and that this cancellation has a dramatic effect on transition.

The component of the streamwise velocity at the exciting frequency u'_f is plotted versus y in Figure 5.26. The measurements in this figure were made in the laminar region of the flow at $R_x=0.97x10^6$. The lock-in mode was used to measure the data for sound excitation or plate vibration alone. The measurements for the other two cases were made in the band-pass mode. In Figure 5.26 the results for these last two cases were multiplied by ten to separate the data points from the horizontal axis. One notes that u'_f was very large (more than one hundred times the sound excitation particle velocity) when the excitation was either sound or plate vibration. It also shows that the magnitude of u'_f was almost identical for the two excitation cases, while their phases were very nearly 180 degrees apart.

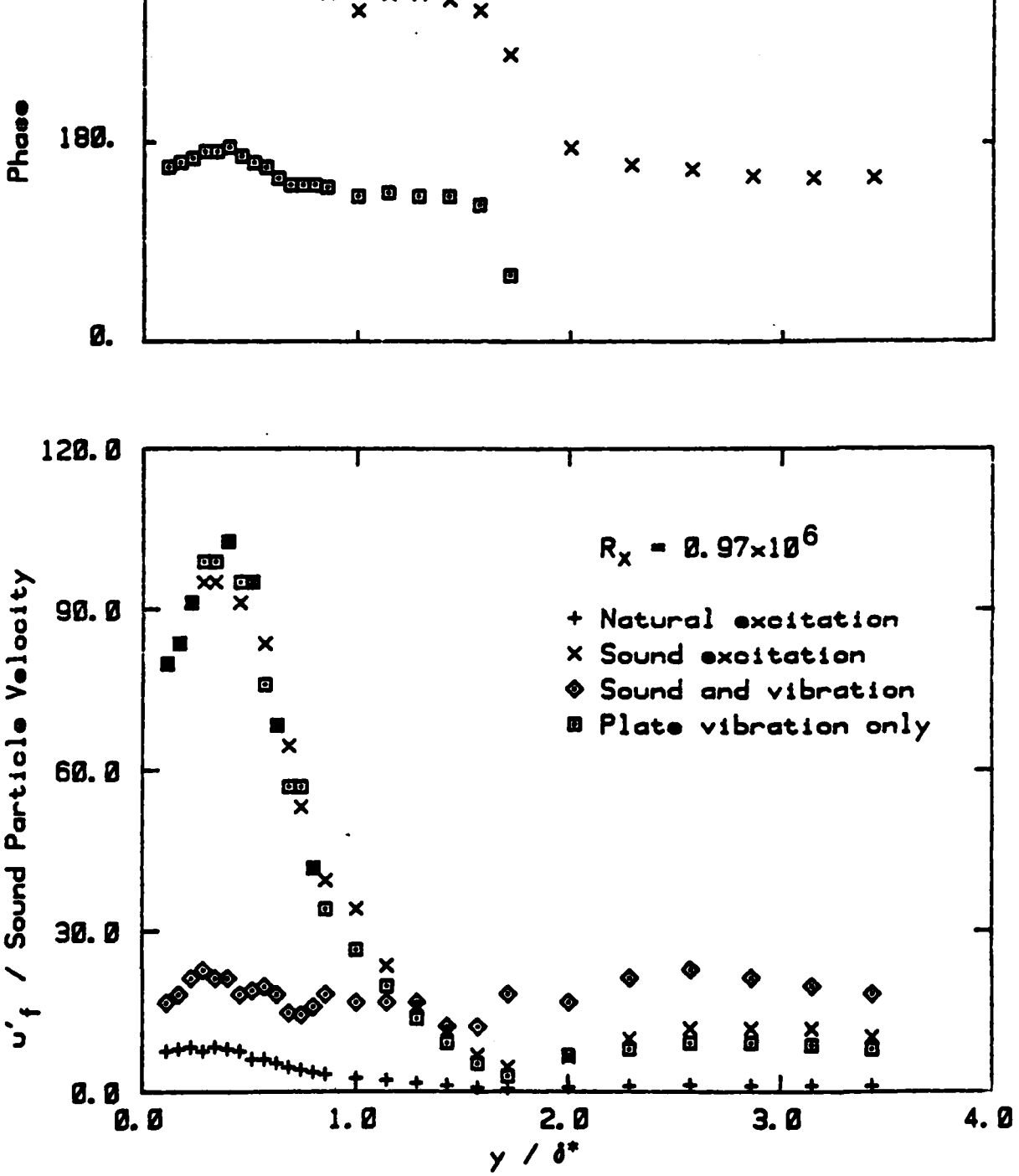

FIGURE 5.26 Velocity fluctuations (at 500 Hz) as functions of y. U_∞ = 29.0 m/s. (+ and ◇ are 10 times their actual magnitudes.)

Figure 5.26 also indicates that, when the sound and the plate vibration were simultaneously applied, u'_f decreased to about 1/50th of the level corresponding to either excitation alone.

It is well known that boundary layer transition is a highly nonlinear process. However, this experiment demonstrates that boundary layer transition can be strongly influenced by a linear interaction between the effects of sound excitation and plate vibration. This interaction clearly takes place upstream of the transition region, where the velocity fluctuations are small. This experiment also demonstrates the linearity involved in the generation of a TS wave by sound or by plate vibration. Shapiro [7] and Goldstein [47] have also demonstrated that sound generates a TS wave linearly. The results of Section 5.5 suggest that cancellation may also be possible using a vibrating ribbon in conjunction with sound or plate vibration. These results also support the evidence, presented in Sections 5.3 and 5.4 that both sound and plate vibration generate TS waves through an interaction at the plate's leading edge.

One possible application of this result is to cases where boundary layer transition is strongly influenced by sound or plate vibration. It may be easier to provide an excitation to cancel the TS waves rather than to reduce the

original excitation. For example, in wind or water tunnel testing, the so-called "unit Reynolds number effect" is often due to excitation of the boundary layer by periodic, background acoustic waves. This excitation might be significantly reduced by the previously described cancellation technique.

5.8 Characteristics of the Boundary Layer Excitations

The Appendix contains potential flow calculations for the approximate motion of the stagnation point due to transverse vibration of the plate's leading edge. This motion gives a relative indication of the boundary layer excitation at the leading edge For the low-level plate vibration case (the equivalent level of vibration during the sound excitation, where the transverse plate velocity was 7.3×10^{-6} m/s), the amplitude of the stagnation point motion was 4.5×10^{-6} mm, vertically. This compares to 9.1×10^{-4} mm for the high level plate vibration case (transverse plate velocity = 1.55×10^{-3} m/s).

It was noted in Chapter III that the sound excitation contained an antisymmetric part and a symmetric part, where the symmetry is with respect to the plane at the center of the plate's thickness. This lack of symmetry was due to the following reason. The test section contained standing waves

above and below the plate during the sound excitation tests. Figure 4.6 shows the standing sound waves in the test section above the plate. Figure 5.27 shows the variation in the sound pressure level at the excitation frequency versus the distance downstream of the leading edge in the test section below the plate. Comparing Figures 4.6 and 5.27 reveals that the nodes and antinodes of the standing waves were in different locations and had different magnitudes in the two parts of the test section. This was due to the different acoustic impedances at the open end of the test section for the two sides of the plate.

To quantify the symmetric and antisymmetric components of the sound excitation, the velocity fluctuations at the excitation frequency u'_f due to the sound were measured near the leading edge of the plate. These measurements were taken at 200 Hz with U_∞=18.5 m/s, using the lock-in amplifier in the locked-in mode. The velocity fluctuations were measured at positions above and below the plate, equidistant from the center of the plate's thickness and where x=0 and 3.8 cm. These fluctuations were produced by the superposition of symmetric and antisymmetric components of the sound excitation. Since the phase of the hot wire response was determined relative to that of the signal driving the loudspeaker, it was not necessary to make simultaneous measurements above and below the plate in order

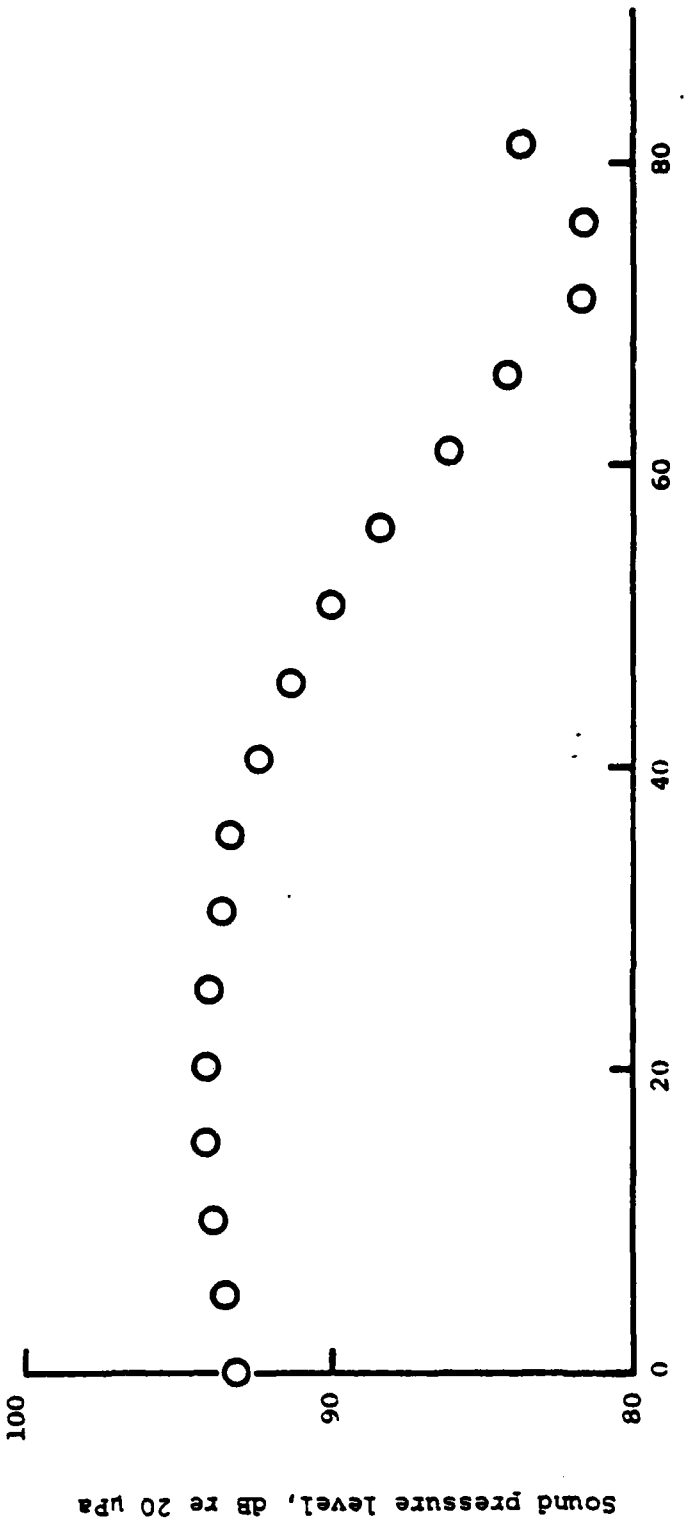

FIGURE 5.27 Sound pressure level (at 200 Hz) as a function of x under the test plate during the sound excitation tests (U_∞ = 18.5 m/s).

to separate the symmetric component from the antisymmetric component. The rms level of the symmetric component is plotted versus distance from the center of the plate's thickness in Figure 5.28. Figure 5.29 shows the antisymmetric component, plotted on the same coordinates as in Figure 5.28. The phase in Figure 5.29 is the phase of the antisymmetric component above the plate. Figure 5.28 shows that the magnitude and phase of the symmetric component are approximately constant with distance from the plate. This behavior would be expected for plane wave sound excitation. Figure 5.29 shows that the phase of the antisymmetric component is approximately constant with distance from the plate while its magnitude decays with distance from the plate.

It is apparent that the sound excitation does indeed contain symmetric and antisymmetric components in the region near the plate's leading edge. The boundary layer excitation during the sound tests was therefore a combination of these two components.

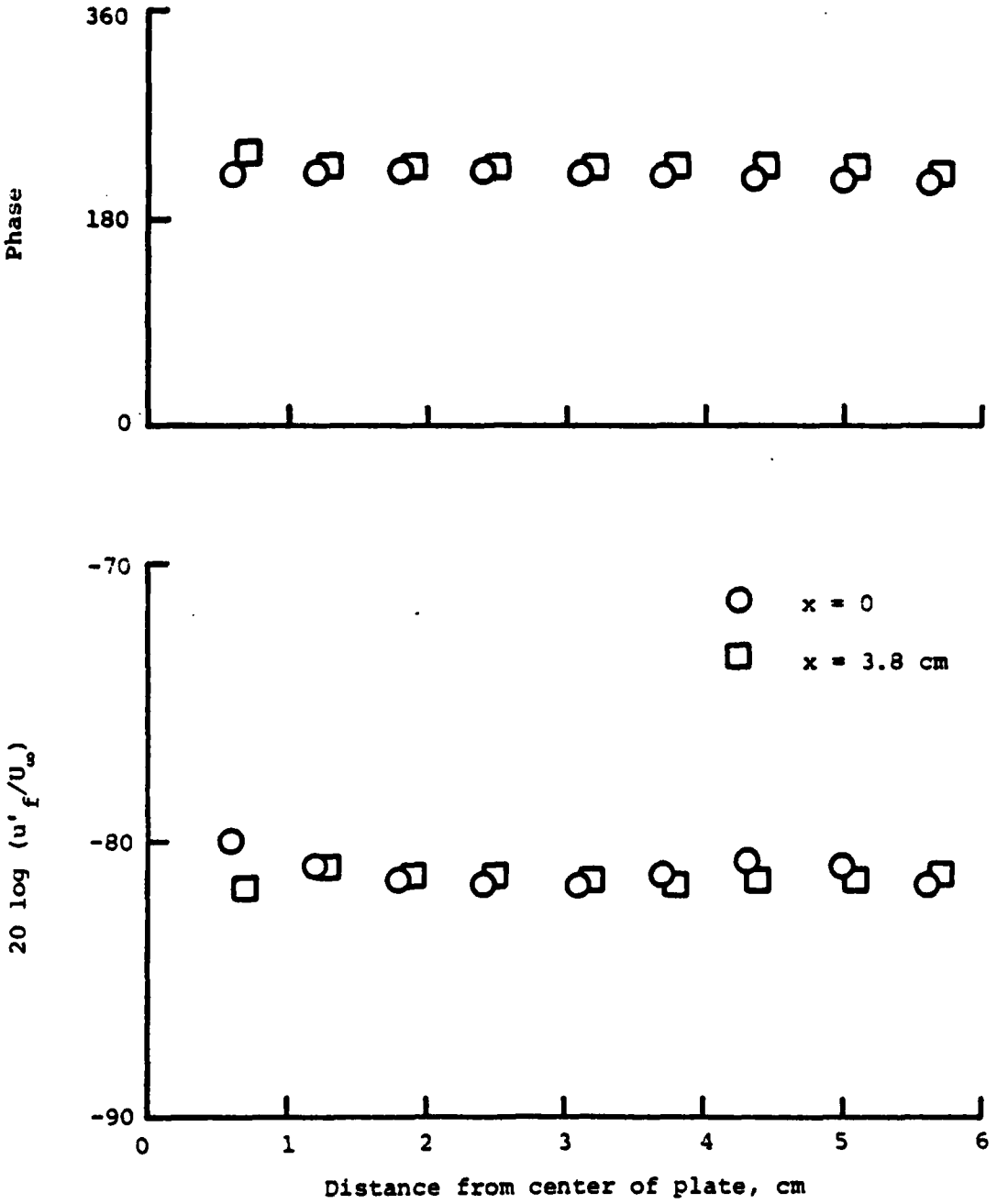

FIGURE 5.28 Symmetric component of the fluctuating velocity (at 200 Hz) as a function of the distance from the plate's center during the sound excitation tests (U_∞ = 18.5 m/s).

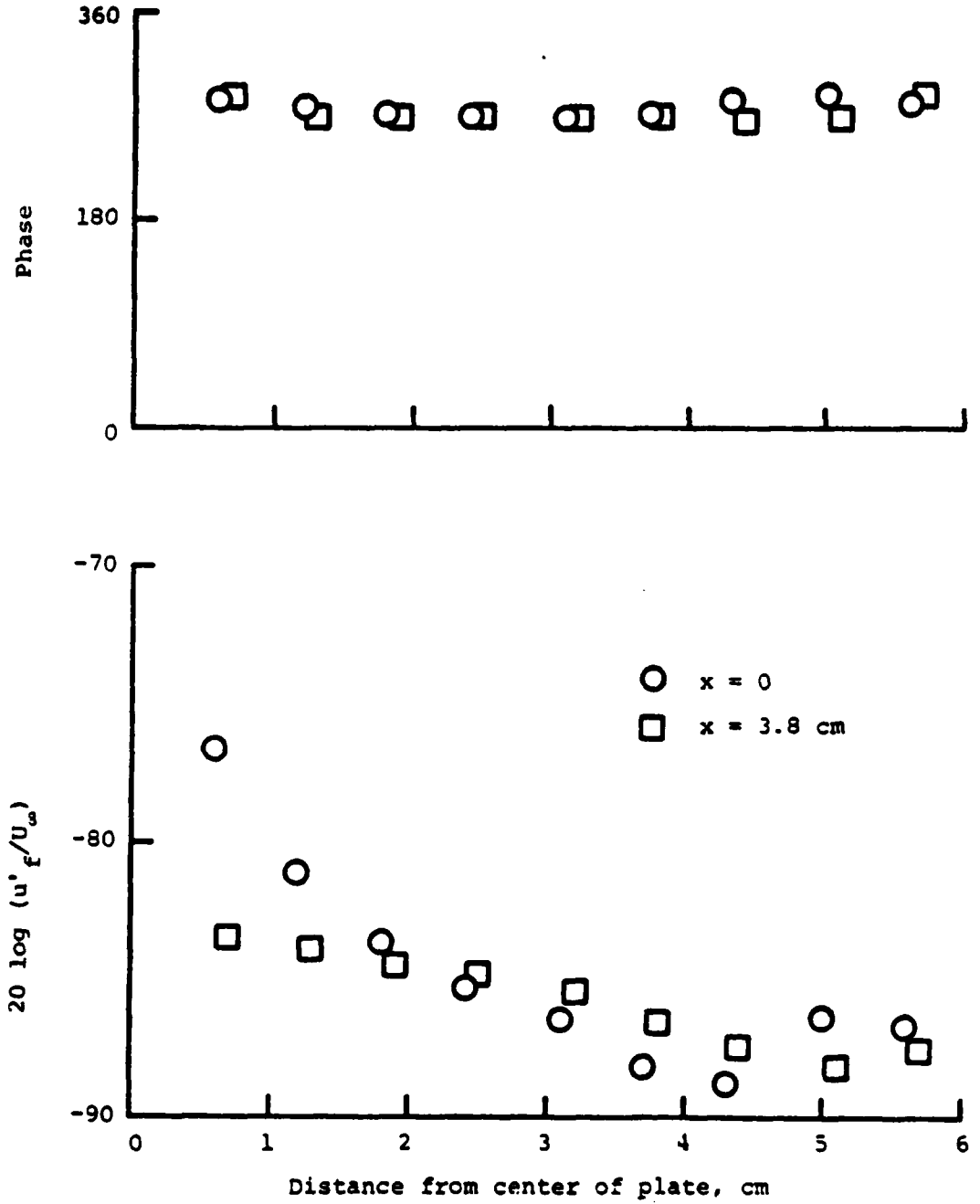

FIGURE 5.29 Antisymmetric component of the fluctuating velocity (at 200 Hz) as a function of the distance from the plate's center during the sound excitation tests (U_∞ = 18.5 m/s).

VI CONCLUSIONS

It has been shown that the naturally excited laminar boundary layer disturbances which appear in our wind tunnel are primarily due to free stream turbulence. These are presumably TS waves, and they appear in random packets with random propagation directions. Owing to the varying propagation directions of these waves, their growth is less than the maximum growth, as is predicted from the analysis of Squire [34] and as is given in Lin [35]. Along with these disturbances, there are small background acoustic waves (Stokes shear-waves) and the TS waves which are excited by these acoustic disturbances. The level of background acoustic waves is not known. The growth of the natural disturbances measured at the same nondimensional frequency β but different flow speeds is different. This is due to changes in the pressure gradient and in the background acoustic levels.

The excitation of a laminar boundary layer by streamwise propagating sound or by plate vibration has been shown to produce a TS wave disturbance in the downstream portion of the boundary layer. The magnitude of the excited TS wave can be considerably larger than the time averaged magnitude of the naturally occurring disturbances though the

naturally occurring wave packet may have a larger peak amplitude. At each point in the boundary layer, the phase of the excited TS wave is constant in time with respect to the phase of the excitation, indicating that the origin of the TS wave is at a fixed position in the boundary layer. The theoretical analyses of Goldstein [47] and Murdock [48] suggest that the TS wave origin is at the plate's leading edge.

The vibrating ribbon experiments have shown that the TS wave generated by the ribbon superimposes linearly with the TS wave generated by the sound excitation. The downstream influence of the sound upon the development of the TS wave is negligible. This supports the prediction of the linear theory that the Stokes shear-wave (the sound wave) is completely decoupled from the TS wave in the double layer. Evidence of higher modes of the Orr-Sommerfeld equation generated by the vibrating ribbon has also been given. The exact mode shapes and wave properties of these higher modes are needed if this experimental evidence is to be conclusive.

The linearity of the TS wave response to various excitations was exploited to produce dramatic changes in the transition process. Sound and plate vibration were used to excite the TS waves. It was demonstrated that the

transition Reynolds number (R_{xtr}) could be delayed from 1.2×10^6 to 1.8×10^6 by the cancellation of an excited TS wave. The cancellation reduced the level of the laminar boundary layer oscillations to 1/50th of their original level at $R_x = 0.97 \times 10^6$. It is clear that the transition process is dominated by a linear process which occurs near the leading edge when the previously described excitations are applied. This type of cancellation may be useful when two-dimensional streamwise propagating TS waves control the transition process. The random wave packets produced by free stream turbulence cannot be cancelled in this fashion.

The growth of the excited TS waves was shown to be equal to the predicted growth of two-dimensional, streamwise propagating TS waves once the effects of the pressure gradient were taken into account. This indicates that the waves were uniform in the spanwise direction. It would be interesting to attempt to produce a TS wave with a large spanwise component. This could be accomplished by including a spanwise component in the excitation at the plate's leading edge.

The physical phenomena that lead to boundary layer transition are complex and more research is clearly warranted. The theoretical analysis of Goldstein should be modified to include the effects of finite plate thickness

and the influence of the antisymmetric disturbance. Such an analysis should be compared with the experimental results. The analysis should also include the effects of leading edge motion. Very little quantitative information about the higher modes of the Orr-Sommerfeld equation is currently available for the boundary layer case. This information is necessary for comparisons to experimental work. The temporal and spatial stability problems for the boundary layer have been greatly improved by the orthogonality and completeness proofs of Salwen and Grosch [25]. However, the physical significance of the restrictions they impose on the upstream boundary conditions for the spatial problem need to be investigated.

The experimental methods used in this work could be greatly improved by using a digital computer for the control of experiments, data collection, and analysis. More accurate control over the flow speed and the probe positioning would also improve the measurements.

The characteristics of the naturally occurring boundary layer disturbances warrant further examination. The properties of the freestream velocity fluctuations should be more carefully investigated to determine the amounts of turbulent and acoustic energy present. This could possibly be done by measuring the spanwise correlation of these free

stream fluctuations and the spanwise correlation of the boundary layer disturbances they generate.

The generation of TS waves by sound and plate vibration also warrants further investigation. The puzzling results of Spangler and Wells [2] concerning standing sound waves might be explained by the position of the nodes. Since the interaction between the sound and the boundary layer takes place at the leading edge, the excitation of a boundary layer might be drastically reduced by simply moving the node to the leading edge. Experimental and theoretical analyses into these phenomena would provide a better understanding of the transition process.

REFERENCES

1. Schubauer, G.B. and Skramstad, H.K., "Laminar-Boundary-Layer Oscillations and Transition on a Flat Plate," NACA Report No. 909, 1948.

2. Spangler, J.G. and Wells, C.S., "Effects of Freestream Disturbances on Boundary-Layer Transition," AIAA Journal, Vol. 6, No. 3, 1968, p. 543.

3. Laehey, P., "The Influence of Environment in Laminar Boundary Layer Control," AIAA Progress in Astronautics and Aeronautics, Vol. 72, 1980.

4. Philippov, V.M., "Experimental Investigation of the Influence of a Pressure Gradient on Laminar-to-Turbulent Boundary Layer Transition," Scientific Annals TsAGI, Vol. 6, No. 6, 1975, (in Russian).

5. Polyakov, N.Ph., "The Influence of the Low Free Stream Perturbations on the Condition of Laminar Boundary Layer," Archives of Mechanics (Arch. Stos.), Vol. 31, Issue 3, 1979, p. 327.

6. Wells, C.S., "Effects of Freestream Turbulence on Boundary-Layer Transition," AIAA J., Vol. 5, 1967, p. 172.

7. Shapiro, P.J., "The Influence of Sound Upon Boundary Layer Instability," M.I.T. Acoustics and Vibration Laboratory Report No. 83458-83560-1, 1977.

8. Prandtl, L., Verh. 3d Int. Math. Kongr. Heidelb., (trans. as NACA Tech. Mem. 452), 1904, p. 484.

9. Blasius, H., Z. Angew. Math. Phys., Vol. 56, (trans. as NACA Tech. mem. 1256), 1908, p. 1.

10. Rayleigh, Lord., Scientific Papers, Vol. 1, Dover, NY, 1964, p. 474.

11. Orr, W.M.F., Proc. R. Irish Acad., Vol. 27, 1907, p. 9.

12. Sommerfeld, A., Atti. 4th Congr. Int. Math., Rome, Vol. 3, 1908, p. 116.

13. Tollmien, W., "The Production of Turbulence," NACA Tech. Mem. No. 609, 1931.

14. Tollmien, W., "General Instability Criterion of Laminar Velocity Distributions," NACA Tech. Mem. 792, 1936.

15. Schlichting, H, "Zur Entstehung der Turbulenz bei der Plattenstromung," Nach. Gesell. d. Wiss. z. Gottingen, Math.

Phys. Klasse, 1933, p. 181.

16. Schlichting, H., "Amplitudenverteilung und Energiebilanz der kleinen Storungen bei der Plattenstromung," Nach. Gesell. d. Wiss. z. Gottingen. Math. Phys. Klasse, Vol. 1, 1935, p. 47.

17. Schlichting, H., "Uber die Entstehung der Turbulenz in einem Rotierenden Zylinder," Nach. Gesell. d. Wiss. z. Gottingen, Math. Phys. Klasse, No. 2, 1932, p. 160.

18. Schlichting, H., "Turbulenz bei Warmeschichtung," Z.f.a. M.M., Vol. 15, No. 6, 1935, p. 313.

19. Jordinson, R., "The Flat Plate Boundary Layer. Part 1. Numerical Integration of the Orr-Sommerfeld Equation," J. Fluid Mech., Vol. 43, part 4, 1970, p. 801.

20. Barry, M.D.J., and Ross, M.A.S., "The Flat Plate Boundary Layer. Part 2. The Effect of Increasing Thickness on Stability," J. Fluid Mech., Vol. 43, part 4, 1970, p. 813.

21. Ross, J.A., Barnes, F.H., Burns, J.G., and Ross, M.A.S., "The Flat Plate Boundary Layer. Part 3. Comparison of Theory with Experiment," J. Fluid Mech., Vol. 43, part 4, 1970, p.

819.

22. Mack, L.M., "A Numerical Study of the Temporal Eigenvalue Spectrum of the Blasius Boundary Layer," J. Fluid Mech., Vol. 73, part 3, 1976, p. 497.

23. Corner, D.. Houston, D.J.R., and Ross, M.A.S., "Higher Eigenstates in Boundary-Layer Stability Theory," J. Fluid Mech., Vol. 77, part 1, 1976, p. 81.

24. Grosch, C.E. and Salwen, H., "The Continuous Spectrum of the Orr-Sommerfeld Equation. Part 1. The Spectrum and Eigenfunctions," J. Fluid Mech., Vol. 87, part 1, 1978, p. 33.

25. Salwen, H. and Grosch, C.E., "The Continuous Spectrum of the Orr-Sommerfeld Equation. Part 2. Eigenfunction Expansions," J. Fluid Mech., Vol. 104, 1981, p. 445.

26. Klebanoff, P.S., Tidstrom, K.D., and Sargent, L.M., "The Three-Dimensional Nature of Boundary-Layer Instability," J. Fluid Mech., Vol. 12, 1962, p. 1.

27. Reshotko, E., "Boundary-Layer Stability and Transition," Annual Review of Fluid Mechanics, Vol. 8, 1976, p. 311.

28. Landahl, M.T., "Wave Mechanics of Breakdown," J. Fluid Mech., Vol. 56, 1972, p. 775.

29. Saric, W.S. and Reynolds, G.A., "Experiments on the Stability of Nonlinear Waves in a Boundary Layer," I.U.T.A.M. Symp. on Laminar-Turbulent Transition, Stuttgart, September 1979.

30. Nayfeh, A.H., "Three-Dimensional Stability of Growing Boundary Layers," I.U.T.A.M. Symp. on Laminar-Turbulent Transition, Stuttgart, September 1979.

31. Schilz, W., "Untersuchungen uber den Einfluss biegeformiger Wandschwingungen auf die Entwicklung der Stromungsgrenzschidnt," Acustica, Vol. 15, No. 1, 1965, p. 6.

32. Schilz, W., "Experimentelle Untersuchungen zur akustischen Beeinflussung der Stromungsgrenzschicht in Luft," Acustica, Vol. 16, No. 4, 1965/66, p. 208.

33. Mechel, F. and Schilz, W., "Untersuchungen zur akustichen Beeinflussung der Stromungsgrenzschicht in Luft," Acustica, Vol. 14, 1964, p. 325.

34. Squire, H.B., "On the Stability of Three-Dimensional

Disturbances of Viscous Flow Between Parallel Walls," Proc. Roy. Soc. Lond. A., Vol. 142, 1933, p. 621.

35. Lin, C.C., The Theory of Hydrodynamic Stability, Cambridge University Press, London, 1955.

36. Kachanov, Yu.S., Kozlov, V.V., and Levchenko, V.Ya., "Generation and Development of Low-Amplitude Perturbations in a Laminar Boundary Layer in the Presence of an Acoustic Field," Izv. Sib. Otd. Akad. Nauk. SSSR, No. 13, Ser. Tekh. Nauk, Vol. 3, 1975, p. 18.

37. Thomas, A.S.W. and Lekoudis, S.G., "Sound and Tollmien-Schlichting Waves in a Blasius Boundary Layer," Phys. Fluids, Vol. 21, No. 11, 1978, p. 2122.

38. Milling, R.W., "Tollmien-Schlichting Wave Cancellation," Phys. Fluids, Vol. 24, No. 5, 1981, p. 979.

39. Liepmann, H.W., Brown, G.L., and Nosenchuck, D.M., "Control of Laminar-Instability Waves Using a New Technique," J. Fluid Mech., Vol. 118, 1982, p. 187.

40. Liepmann, H.W. and Nosenchuck, D.M., "Active Control of Laminar-Turbulent Transition," J. Fluid Mech., Vol. 118, 1982, p. 201.

41. Grosch, C.E. and Salwen, H., "The Stability of Steady and Time-Dependent Plane Poiseuille Flow," J. Fluid Mech., Vol. 34, part 1, 1968, p. 177.

42. Lighthill, M.J., "The Response of Laminar Skin Friction and Heat Transfer to Fluctuations in the Steam Velocity," Proc. Roy. Soc. Lond. A., Vol. 224, 1954, p. 1.

43. Lin, C.C., "Motion in the Boundary Layer with a Rapidly Oscillating External Flow," Proc. Int. Cong. App. Mech., Brussels, 1957.

44. Lam, S.H. and Rott, N., "Theory of Linearized Time-Dependent Boundary Layers," Cornell University, GSAE Rep. AFOSR TN-60-1100, 1960.

45. Ackerberg, R.C. and Phillips, J.H., "The Unsteady Laminar Boundary Layer on a Semi-Infinite Flat Plate due to Small Fluctuations in the Magnitude of the Free-Stream Velocity," J. Fluid Mech., Vol. 51, part 1, 1972, p. 137.

46. Patel, M.H., "On Laminar Boundary Layers in Oscillatory Flow," Proc. Roy. Soc. Lond. A., Vol. 347, 1975, p. 99.

47. Goldstein, M.E., "The Evolution of Tollmien-Schlichting Waves near a Leading Edge," J. Fluid Mech., Vol. 127, 1983,

p. 59.

48. Murdock, J.W., "The Generation of a Tollmien-Schlichting Wave by a Sound Wave," Proc. Roy. Soc. Lond. A., Vol. 372, 1980, p. 517.

49. Murdock, J.W., "Tollmien-Schlichting Waves Generated by Unsteady Flow Over Parabolic Cylinders," AIAA 19th Aerospace Sciences Meeting, St. Louis, January 1981.

50. Aizin, L.B. and Volodin, A.G., "Stability of the Boundary Layer Above the Surface of a Wave Travelling Over a Plate," Zhurnal Prikladroi Mekhaniki Tekhnicheskoi Fiziki, No. 5, 1979, p. 49.

51. White, F.M., Viscous Fluid Flow, McGraw-Hill, New York, 1974.

52. Loehrke, R.I., Morkovin, M.V., and Fejer, A.A., "Review-Transition in Nonreversing Oscillating Boundary Layers," J. Fluids Eng., Vol. 97, 1975, p. 534.

53. Schlichting, H., Boundary Layer Theory, 6th Edition, McGraw-Hill, New York, 1968.

54. Gaster M., "On the Generation of Spatially Growing

Waves in a Boundary Layer," J. Fluid Mech., Vol. 22, part 3, 1965, p. 433.

55. Orszag, S.A., "Accurate Solultion of the Orr-Sommerfeld Stability Equation," J. Fluid Mech., Vol. 50, part 4, 1971, p. 689.

56. Wasow, W., Annals of Mathematics, Vol. 49, 1948, p. 852,

57. Wasow, W., Annals of Mathematics, Vol. 52, 1950, p. 350.

58. Wasow, W., Annals of Mathematics, Vol. 58, 1953, p. 222.

59. Obremski, H.J., Morkovin, M.V., and Landahl, M., "A Portfolio of Stability Characteristics of Incompressible Boundary Layers," NATO AGARDograph 134, 1969.

60. Hanson, C.E., "The Design and Construction of a Low-Noise, Low-Turbulence Wind Tunnel," M.I.T. Acoustics and Vibration Laboratory, Report No. 79611-1, 1969.

61. Moeller, M.J., "Measurement of Unsteady Forces on a Circular Cylinder in Cross Flow at Subcritical Reynolds

Numbers," Ph.D. thesis, M.I.T., 1982.

62. Milne-Thomson, L.M., Theoretical Hydrodynamics, 4th ed., MacMillan and Co.,New York, 1960.

APPENDIX

Potential Flow Near the Leading Edge with Plate Vibration

The results of Chapter V have shown that plate vibration produces a disturbance at the leading edge which eventually leads to a TS wave in the downstream portion of the flow (where the Orr-Sommerfeld equation is applicable). The actual phenomena involved in generating the disturbance and how the disturbance evolves into a TS wave are unclear. An exhaustive analysis, as in Goldstein's [47] analysis for sound excitation, is necessary to clarify these details. However, an approximate analysis into the generation of the disturbance may be obtained by examining the stagnation point at the plate's leading edge. This analysis is outlined below.

In the immediate vicinity of a rounded leading edge, the boundary layer is very thin and a first approximation to the flow may be obtained by neglecting viscosity. If the acoustic wavelength is large compared to any dimension of the leading edge, compressibility may also be neglected. These approximations may be written as follows.

$$\kappa(x) >> \delta(x) \tag{A.1}$$

$$\delta(x) << L \tag{A.2}$$

$$c/_{\omega} >> L \tag{A.3}$$

where $\kappa(x)$ is the radius of curvature of the leading edge, $\delta(x)$ is the boundary layer thickness, c is the sound speed, ω is the circular frequency and L is a typical dimension of the leading edge. With these approximations, the analysis becomes a potential flow problem. Since the current interest is in the flow at the extreme leading edge, the plate itself will be neglected and the flow about an elliptic cylinder will be examined. The technique which will be used to obtain a solution is to first determine the flow about a circular cylinder and map this solution onto an elliptic cylinder.

The complex velocity potential for a two-dimensional flow in an unbounded, ideal fluid with a constant velocity in the x direction and a pure tone oscillatory velocity in the y direction (with a constant amplitude throughout the fluid) is

$$f(\bar{z}) = (U_\infty - i\varepsilon_v \cos \omega t)\bar{z} \qquad (A.4)$$

where $\bar{z} = x + iy$, $f(\bar{z}) = \phi(\bar{z}) + i\psi(\bar{z})$, ϕ is the velocity potential, and ψ is the stream function. U_∞ is the mean velocity, ε_v is the oscillatory velocity amplitude and ω is the frequency of the oscillation. Invoking the circle theorem [62], the complex velocity potential for the flow of equation (A.4) with a circular cylinder inserted at the origin is obtained. This potential may be written

$$f(\bar{z}) = U_\infty \left(\bar{z} + \frac{r_0^2}{\bar{z}}\right) - i\varepsilon_v \left(\bar{z} - \frac{r_0^2}{\bar{z}}\right) \cos \omega t \qquad (A.5)$$

where r_0 is the radius of the cylinder. Equation (A.5) represents a circular cylinder in cross flow with an oscillatory y component of the velocity in the outer flow. If the coordinate system is shifted so that the outer flow is just U_∞ with no oscillation, the cylinder will oscillate vertically with velocity $-\varepsilon_v \cos\omega t$. This coordinate transformation does not effect the flow field because the fluid is incompressible.

A Joukowski mapping function,

$$\bar{\zeta} = \bar{z} + a^2/\bar{z}, \tag{A.6}$$

may be used to map the circular cylinder in the $\bar{z}$ plane to an elliptic cylinder in the $\bar{\zeta}$ plane, if $a < |z|$. The complex velocity in the $\bar{\zeta}$ plane, $w(\bar{\zeta}) = u - iv$, is related to $f(\bar{z})$ by

$$w(\bar{\zeta}) = \frac{df}{d\bar{\zeta}} = \frac{df}{d\bar{z}} \frac{d\bar{z}}{d\bar{\zeta}}, \tag{A.7}$$

or

$$w(\bar{\zeta}) = [U_\infty (1 - \frac{r_0^2}{\bar{z}^2}) - i\varepsilon_v (1 + \frac{r_0^2}{\bar{z}^2}) \cos \omega t] \frac{1}{1 - a^2/\bar{z}^2} \tag{A.8}$$

On the cylinder, $\bar{z} = r_0 e^{i\theta}$, and the stagnation point may be found by setting $w(\bar{\zeta})$ to zero. The term $1/(1 - a^2/\bar{z}^2)$ cannot be zero on the cylinder, so the bracketed term must be zero at the stagnation point. This may be written as

$$U_\infty (1 - e^{-i2\theta}) = i\varepsilon_v (1 + e^{-i2\theta}) \cos \omega t \qquad (A.9)$$

Expressing $\overline{\zeta}$ as $\eta + i\xi$, θ may be related to η and ξ on the cylinder as follows.

$$\xi = (r_0 + a^2/r_0)\cos\theta \qquad (A.10)$$

and $$\eta = (r_0 - a^2/r_0)\sin\theta. \qquad (A.11)$$

The insertion of equation (A.11) into (A.9) yields the vertical displacement of the stagnation point, expressed as

$$\eta^2 = (r_0 - \frac{a^2}{r_0})^2 \left(\frac{(\varepsilon_v^2/U_\infty^2)\cos^2 \omega t}{1 + (\varepsilon_v^2/U_\infty^2)\cos^2 \omega t} \right) \qquad (A.12)$$

which is maximum when $\cos\omega t = \pm 1$. Therefore,

$$\eta^2_{max} = (r_0 - \frac{a^2}{r_0})^2 \left(\frac{\varepsilon^2_v/U^2_\infty}{1 + \varepsilon_v^2/U^2_\infty} \right). \qquad (A.13)$$

For the results discussed in Chapter V (6:1 ellipse with 1.27 cm thickness),

$$r_0 - a^2/r_0 = 6.35 \text{ mm} \quad \text{and} \quad U_\infty = 18.5 \text{ m/s}.$$

In the $\bar{z}$ plane, $\varepsilon_v = 1.3\text{x}10^{-5}$ m/s, for the sound excitation tests and $2.66\text{x}10^{-3}$ m/s for the plate vibration tests. Therefore,

$$\eta_{max} = 4.5\text{x}10^{-6} \text{ mm}$$

due to plate motion in the sound excited tests and

$$\eta_{max} = 9.1\text{x}10^{-4} \text{ mm}$$

due to plate motion in the plate vibration tests. These results show that the motion of the stagnation point is indeed small (only 0.007% of the thickness of the ellipse). The magnitude of η_{max} provides an approximate relative

magnitude for the generated boundary layer disturbance, which eventually leads to a TS wave.

Distribution List

Defense Technical Information Center
Cameron Station
Alexandria, VA 22314

Office of Naval Research
Code 432
Fluid Mechanics Division
800 N. Quincy Street
Arlington, VA 22217

Professor Bruce Johnson
U.S. Naval Academy
Engineering Department
Annapolis, MD 21402

NASA Scientific and Technical
Information Facility
P.O. Box 8757
Baltimore/Washington International
Airport
Maryland 21240

Technical Library
David W. Taylor Naval Ship Research
& Development Center
Annapolis Laboratory
Annapolis, MD 21402

Prof. Paul M. Naghdi
Department of Mechanical Engineering
The University of California
Berkeley, CA 94720

Prof. C.-S. Yih
Department of Engineering Mechanics
The University of Michigan
Ann Arbor, MI 48109

Librarian
Department of Naval Architecture
The University of California
Berkeley, CA 94720

Office of Naval Research
Code 200B
Technology Program
800 N. Quincy Street
Arlington, VA 22217

Prof. John V. Wehausen
Department of Naval Architecture
The University of California
Berkeley, CA 94720

Library
David W. Taylor Naval Ship Research
& Development Center
Code 522.1
Bethesda, MD 20084

Technical Library
Naval Surface Weapons Center
Dahlgren Laboratory
Dahlgren, VA 22418

Mr. Justin H. McCarthy, Jr.
David W. Taylor Naval Ship Research
& Development Center
Code 1540
Bethesda, MD 20084

Technical Documents Center
Army Mobility Equipment Research Ctr.
Building 315
Fort Belvoir, VA 22060

Dr. William B. Morgan
David W. Taylor Naval Ship Research
& Development Center
Code 1500
Bethesda, MD 20084

Technical Library
Webb Institute of Naval Architecture
Glen Cove, NY 11542

Director
Office of Naval Research
Eastern/Central Regional Office
Building 114, Section D
666 Summer Street
Boston, MA 02210

Dr. J. P. Breslin
Stevens Institute of Technology
Davidson Laboratory
Castle Point Station
Hoboken, NJ 07030

Library
Naval Weapons Center
China Lake, CA 93555

Prof. Louis Landweber
The Institute of Hydraulic Research
Iowa City, IA 52242

R.E. Gibson Library
The Johns Hopkins University
Applied Physics Laboratory
Johns Hopkins Road
Laurel, MD 20810

The Society of Naval Architects &
Marine Engineers
One World Trade Center, Suite 1369
New York, NY 10048

Lorenz G. Straub Library
St. Anthony Falls Hydraulic Lab.
The University of Minnesota
Minneapolis, MN 55414

Technical Library
Naval Coastal System Laboratory
Panama City, FL 32401

Library
Naval Postgraduate School
Monterey, CA 93940

Prof. Theodore Y. Wu
Engineering Sciences Department
California Institute of Technology
Pasadena, CA 91125

Technical Library
Naval Underwater Systems Center
Newport, RI 02840

Director
Office of Naval Research
Western Regional Office
1030 E. Green Street
Pasadena, CA 91101

Engineering Societies Library
345 East 47th Street
New York, NY 10017

Technical Library
Naval Ship Engineering Center
Philadelphia Division
Philadelphia, PA 19112

Army Research Office
P.O. Box 12211
Research Triangle Park, NC 27709

Librarian Station 5-2
Coast Guard Headquarters
NASSIF Building
400 Seventh Street, SW
Washington, DC 20591

Editor
Applied Mechanics Review
Southwest Research Institute
8500 Culebra Road
San Antonio, TX 78206

Defense Research & Development Attache
Australian Embassy
1601 Massachusetts Avenue, NW
Washington, DC 20036

Technical Library
Naval Ocean Systems Center
San Diego, CA 92152

Library of Congress
Science and Technology Division
Washington, DC 20540

ONR Scientific Liaison Group
American Embassy - Room A-407
APO San Francisco 96503

Dr. A.L. Slafkosky
Scientific Advisor
Commandant of the Marine Corps
Code 2042 AA
Washington, DC 20380

Librarian
Naval Surface Weapons Center
White Oak Laboratory
Silver Spring, MD 20910

Maritime Administration
Office of Maritime Technology
14th & E Streets, NW
Washington, DC 20230

Maritime Administration
Division of Naval Architecture
14th & E Streets, NW
Washington, D.C. 20230

Mr. Stanley W. Doroff
Mechanical Technology, Inc.
2731 Prosperity Avenue
Fairfax, VA 22031

Dr. G. Kulin
National Bureau of Standards
Mechanics Section
Washington, DC 20234

Dr. Charles Watkins
Head, Mechanical Engineering Dept.
Howard University
Washington, DC 20059

Naval Research Laboratory
Code 2627
Washington, D.C. 20375

Library
Naval Sea Systems Command
Code 09GS
Washington, DC 20362

Mr. Thomas E. Peirce
Naval Sea Systems Command
Code 03512
Washington, DC 20362

Prof. A.J. Acosta
Div. of Engineering & Applied Science
Mail Code 104-44
California Institute of Technology
Pasadena, CA 91125

Mr. Ralph D. Cooper
Flow Research
Washington, D.C. Office, Suite 401
1320 Fenwick Lane
Silver Spring, MD 20910

Dennis Bushnell
Mail Stop 163
NASA Langley
Hampton, VA 23665

Dr. Mohamed Gad-el-Hak
Senior Research Scientist & Proj. Mgr.
Flow Research Company
21414 68th Avenue South
Kent, WA 98031

James W. Slack
Chase, Inc.
238 Main Street, Suite 507
Cambridge, MA 02142

Dr. Marvin E. Goldstein
NASA Lewis Research Center
Mail Stop 5-9
21000 Brookpark Road
Cleveland, OH 44135

Dr. Mario J. Casarella
Dept. of Mechanical Engineering
The Catholic University of America
Washington, D.C. 20064

Eugene C. Gritton
Engineering & Applied Sciences Dept.
The Rand Corporation
1700 Main Street
Santa Monica, CA 90406

Prof. Stanley Corrsin
Dept. of Mechanics & Materials Science
The Johns Hopkins University
Baltimore, MD 21218

Prof. Chester E. Grosch
1-14050
Old Dominion University
Norfolk, VA 23508

Mr. Robert J. Hansen
Fluid Dynamics Branch
Naval Research Laboratory
Code 387 - Bldg. 34
Washington, D.C. 20375

Prof. Richard E. Kronauer
Division of Engineering & Applied Phys.
324 Pierce Hall
Harvard University
Cambridge, MA 02138

Dr. Richard E. Hayden
Bolt, Beranek & Newman, Inc.
50 Moulton Street
Cambridge, MA 02138

Dr. George Lea
Fluid Mechanics-Engineering Division
National Science Foundation
Washington, D.C. 20550

Jerry Hefner
Mail Stop 163
NASA Langley
Hampton, VA 23665

Mr. Lucio Maestrello
Mail Stop 163
NASA Langley
Hampton, VA 23665

Dr. Gary R. Hough
Vought Corporation
Advanced Technology Center
P.O. Box 226144
Dallas, TX 75266

Dr. Leslie M. Mack
Jet Propulsion Laboratory
California Institute of Technology
4800 Oak Grove Drive
Pasadena, CA 91103

Dr. T.T. Huang
Code 1552
David W. Taylor
Naval Ship Research & Development Ctr.
Bethesda, MD 20084

J.W. Murdock
The Aerospace Corporation
P.O. Box 92957
Los Angeles, CA 90009

Prof. Mark V. Morkovin
Dept. of Mechanics & Mechanical
& Aerospace Engineering
Illinois Institute of Technology
Chicago, ILLINOIS 60616

Prof. Donald Rockwell
Dept. of Mechanical Engineering
& Mechanics
Building 19
Lehigh University
Bethlehem, PA 18015

Prof. Gabriel Miller
Faculty of Arts & Science
Department of Applied Science
New York University
26-36 Stuyvesant Street
New York, NY 10003

Prof. Eli Reshotko
Glennan Building
Case Western Reserve University
University Circle
Cleveland, OHIO 44106

Prof. Thomas J. Mueller
Aerospace & Mechanical Engineering
University of Notre Dame
Notre Dame, INDIANA 46556

Dr. Michael M. Reischman
Mechanics Division
Code 432
Office of Naval Research
800 North Quincy Street
Arlington, VA 22217

Dr. R.W. Paterson
Aeroacoustics Group
United Aircraft Research Laboratories
East Hartford, CT 06108

Dr. William C. Reynolds
Department of Mechanical Engineering
Stanford University
Stanford, CA 94305

Prof. Allan D. Pierce
School of Mechanical Engineering
Georgia Institute of Technology
Atlanta, GA 30332

Prof. William Saric
Dept. of Engineering Science & Mechanics
Virginia Polytechnic Institute &
State University
Norris Hall
Blacksburg, VA 24061

Dr. Paul Shapiro
Phillips Laboratories
345 Scarborough Road
Briar Cliff Manor
NEW YORK 10510

Prof. Frank M. White
Dept. of Mechanical and Ocean Engineering
University of Rhode Island
Kingston, R.I.

Dr. Robert L. Sternberg
Office of Naval Research
495 Summer Street
Boston, MA 02210

Prof. James Wallace
Dept. of Mechanical Engineering
Surge Facility--Room 2109
University of Maryland
College Park, MD 20742

Dr. Charles Thompson
Dept. of Engineering Science & Mechanics
Virginia Polytechnic Institute & State University
Norris Hall, Room 227
Blacksburg, VA 24061

Marshall P. Tulin
Hydronautics, Inc.
Laurel, MD 20810

Prof. W.W. Willmarth
Aerospace Engineering
Gas Dynamics Laboratories
The University of Michigan
North Campus
Ann Arbor, MICHIGAN 48105

Office of Naval Research
Code 481
800 N. Quincy Street
Arlington, VA 22217

Dr. Robert H. Kraichnan
Dublin
NEW HAMPSHIRE 03444

Prof. Richard W. Miksad
Department of Civil Engineering
The University of Texas at Austin
Austin, TX 78712

Prof. Robert E. Falco
Department of Mechanical Engineering
Michigan State University
East Lansing, MI 48824

Prof. Paul Lieber
Department of Mechanical Engineering
The University of California
Berkeley, CA 94720

Prof. E. Rune Lindgren
Department of Engineering Sciences
231 Aerospace Engineering Building
University of Florida
Gainesbille, FL 32611

Prof. S.I. Pai
Institute of Fluid Dynamics &
Applied Mathematics
The University of Maryland
College Park, MD 20742

Dr. A.K.M. Fazle Hussain
Department of Mechanical Engineering
The University of Houston
Houston, TX 77004

Computation and Analyses Laboratory
Naval Surface Weapons Center
Dahlgren Laboratory
Dahlgren, VA 22418

Prof. John L. Lumley
Sibley School of Mechanical &
Aerospace Engineering
Cornell University
Ithaca, NY [illegible]

Prof. K.E. Shuler
Department of Chemistry
University of California - San Diego
La Jolla, CA 92093

Prof. R. Blackwelder
Department of Aerospace Engineering
University of Southern California
University Park
Los Angeles, CA 90007

Dr. E.W. Montroll
Physical Dynamics, Inc.
P.O. Box 556
La Jolla, CA 92038

Prof. T.R. Thomas
Department of Mechanical Engineering
Teesside Polytechnic
Middlesbrough TS1 3BA
ENGLAND

Prof. Tuncer Cebeci
Mechanical Engineering Department
California State University
Long Beach, CA 90840

Dr. Arthur B. Metzner
Department of Chemical Engineering
University of Delaware
Newark, DE 19711

Dr. C.W. Hirt
Los Alamos Scientific Laboratory
University of California
P.O. Box 1663
Los Alamos, NM 87544

Prof. Harry E. Rauch
The Graduate School & University Center
of the City University of New York
Graduate Center
33 West 42 Street
New York, NY 10036

Prof. Frederick K. Browand
Department of Aerospace Engineering
University of Southern California
University Park
Los Angeles, CA 90007

Dr. Norman M. Nilsen
Dyntech Company
5301 Laurel Canyon Boulevard, Suite 2[illegible]
North Hollywood, CA 91607

Prof. L. Gary Leal
Div. of Chemistry & Chemical Engineering
California Institute of Technology
Pasadena, CA 91125

Prof. Francis R. Hama
Department of Mechanical &
Aerospace Engineering
Princeton University
Princeton, NJ 08540

Prof. H.W. Liepmann
Graduate Aeronautical Laboratories
California Institute of Technology
Pasadena, CA 91125

Dr. Joseph H. Clarke
Division of Engineering
Brown University
Providence, RI 02912

Prof. A. Roshko
Graduate Aeronautical Laboratories
California Institute of Technology
Pasadena, CA 91125

Prof. J.T.C. Liu
Division of Engineering
Brown University
Providence, RI 02912

Prof. K.M. Agrawal
Department of Mathematics
Virginia State College
Petersburg, VA 23803

Chief, Document Section
Redstone Scientific Information Center
Army Missile Command
Redstone Arsenal, AL 35809

Technical Library
Naval Missile Center
Point Mugu, CA 93041

Dr. Jack W. Hoyt
Naval Ocean Systems Center
Code 2501
San Diego, CA 92152

Prof. Richard L. Pfeffer
Geophysical Fluid Dynamics Institute
Florida State University
Tallahassee, FL 32306

Dr. Phillip S. Klebanoff
Mechanics Section
National Bureau of Standards
Washington, DC 20234

Dr. Denny R.S. Ko
Dynamics Technology, Inc.
22939 Hawthorne Boulevard, Suite 200
Torrance, CA 90505

Dr. J.O. Elliot
Naval Research Laboratory
Code 8310
Washington, DC 20375

Prof. Thomas J. Hanratty
Department of Chemical Engineering
University of Illinois at Urbana-Champaign
205 Roger Adams Laboratory
Urbana, IL 61801

Mr. R.J. Hansen
Naval Research Laboratory
Code 387 - Building 34
Washington, DC 20375

Air Force Office of Scientific Research/NA
Building 410
Bolling AFB
Washington, DC 2033 2

Dr. Gary Chapman
Mail Stop 227-4
Ames Research Center
Moffett Field, CA 94035

Prof. Hsien-Ping Pao
Department of Civil Engineering
The Catholic University of America
Washington, DC [illegible]

Prof. Sheila Widnall
37-475
MIT

Prof. J. Haritonides
37-461
MIT

Prof. Steven Orszag
2-347
MIT

Prof. T. Francis Ogilvie
5-230
MIT

Prof. Erik Mollo-Christensen
54-1726
MIT

Prof. P.S. Virk
66-558
MIT

Prof. C. Forbes Dewey
3-250
MIT

Prof. Marten Landahl
37-467
MIT

END

FILMED

10-83

DTIC